

The Development of a Stratospheric Real-Time Turbulence Modeling System

Michael L. Kaplan
Yuh-Lang Lin
Michael T. Kiefer
Paul S. Suffern
Chad J. Ringley

North Carolina State University
Department of Marine, Earth, and Atmospheric Sciences
Raleigh, North Carolina 27695

7 July 2005

Scientific Report No. 1

APPROVED FOR PUBLIC RELEASE; DISTRIBUTION UNLIMITED.



AIR FORCE RESEARCH LABORATORY
Space Vehicles Directorate
29 Randolph Rd
AIR FORCE MATERIEL COMMAND
Hanscom AFB, MA 01731-3010

This technical report has been reviewed and is approved for publication.

AFRL-VS-HA-TR-2005-1121

/signed/

DOUGLAS HAHN
Contract Manager

/signed/

ROBERT BELAND, Chief
Battlespace Surveillance Innovation Center

This report has been reviewed by the ESC Public Affairs Office (PA) and is releasable to the National Technical Information Service (NTIS).

Qualified requestors may obtain additional copies from the Defense Technical Information Center (DTIC). All others should apply to the National Technical Information Service.

If your address has changed, if you wish to be removed from the mailing list, or if the addressee is no longer employed by your organization, please notify AFRL/VSIM, 29 Randolph Rd., Hanscom AFB, MA 01731-3010. This will assist us in maintaining a current mailing list.

Do not return copies of this report unless contractual obligations or notices on a specific document require that it be returned.

Using Government drawings, specifications, or other data included in this document for any purpose other than Government procurement does not in any way obligate the U.S. Government. The fact that the Government formulated or supplied the drawings, specifications, or other data does not license the holder or any other person or corporation; or convey any rights or permission to manufacture, use, or sell any patented invention that may relate to them.

This report is published in the interest of scientific and technical information exchange and its publication does not constitute the Government's approval or disapproval of its ideas or findings.

REPORT DOCUMENTATION PAGE

*Form Approved
OMB No. 0704-0188*

Public reporting burden for this collection of information is estimated to average 1 hour per response, including the time for reviewing instructions, searching existing data sources, gathering and maintaining the data needed, and completing and reviewing this collection of information. Send comments regarding this burden estimate or any other aspect of this collection of information, including suggestions for reducing this burden to Department of Defense, Washington Headquarters Services, Directorate for Information Operations and Reports (0704-0188), 1215 Jefferson Davis Highway, Suite 1204, Arlington, VA 22202-4302. Respondents should be aware that notwithstanding any other provision of law, no person shall be subject to any penalty for failing to comply with a collection of information if it does not display a currently valid OMB control number. PLEASE DO NOT RETURN YOUR FORM TO THE ABOVE ADDRESS.

1. REPORT DATE (DD-MM-YYYY) 07-07-2005			2. REPORT TYPE Scientific Report No. 1			3. DATES COVERED (From - To) 06-07-2004 - 06-06-2005		
4. TITLE AND SUBTITLE The Development of a Stratospheric Real-Time Turbulence Modeling System			5a. CONTRACT NUMBER FA8718-04-C-0011					
			5b. GRANT NUMBER N/A					
			5c. PROGRAM ELEMENT NUMBER 62601F					
6. AUTHOR(S) Michael L. Kaplan, Yuh-Lang Lin, Michael T. Kiefer, Paul S. Suffern and Ringley			5d. PROJECT NUMBER 1010					
			5e. TASK NUMBER 0T					
			5f. WORK UNIT NUMBER A1					
7. PERFORMING ORGANIZATION NAME(S) AND ADDRESS(ES) North Carolina State University Department of Marine, Earth, and Atmospheric Sciences Campus Box 8208 Raleigh, North Carolina 27695			8. PERFORMING ORGANIZATION REPORT NUMBER					
9. SPONSORING / MONITORING AGENCY NAME(S) AND ADDRESS(ES) Air Force Research Laboratory 29 Randolph Road Hanscom AFB, MA 01731-3010			10. SPONSOR/MONITOR'S ACRONYM(S) AFRL/VSBYA					
			11. SPONSOR/MONITOR'S REPORT NUMBER(S) AFRL-VS-HA-TR-2005-1121					
12. DISTRIBUTION / AVAILABILITY STATEMENT Approved for public release; distribution unlimited.								
13. SUPPLEMENTARY NOTES								
14. ABSTRACT. This research project focused on the development of an automated numerical prediction system for stratospheric turbulence. This involved modifying and testing a stratospheric mesoscale numerical model with observed initial data from several case studies. A sequence of events was simulated that likely organized environments favorable for stratospheric turbulence. This sequence involved the development of large amplitude hydrostatic gravity waves that in turn modified the lower stratospheric environment making it favorable for wave breaking and significant eddy dissipation. An automatic grid nesting location system was tested that exploited three different dynamical indices, which would be indicators of the potential for stratospheric turbulence, i.e., the NCSU1 index, vertical variation of the Scorer parameter as well as the eddy dissipation rate derived from the complete turbulence kinetic energy equation. The automatic grid nesting scheme was utilized for several case studies wherein large amplitude gravity waves and substantial latent heating were simulated.								
15. SUBJECT TERMS Turbulence prediction system, Gravity-wave breaking, Dynamic indices								
16. SECURITY CLASSIFICATION OF:			17. LIMITATION OF ABSTRACT	18. NUMBER OF PAGES	19a. NAME OF RESPONSIBLE PERSON Douglas Hahn			
a. REPORT Unclassified	b. ABSTRACT Unclassified	c. THIS PAGE Unclassified	SAR	96	19b. TELEPHONE NUMBER (include area code) (781) 377-2878			

Table of Contents

1. Summary.....	1
2. Introduction.....	1
3. Methods, Assumptions and Procedures.....	2
4. Results and Discussion.....	5
5. Conclusions.....	19
6. Recommendations.....	19
References.....	20
Appendix A. Inertia-Gravity Wave Breaking and Lower-Stratospheric Turbulence During the 2003 Presidents' Day Event.....21	
1. Introduction.....	21
2. Model Description.....	22
3. Analysis of Flow Imbalance and IGW Generation.....	22
4. Transition of IGWs to Turbulence.....	32
5. Summary and Conclusions.....	39
6. Future Work.....	40
References.....	41
Appendix B. A TKE Budget Analysis in the Upper Troposphere/Lower Stratosphere for a Vertically Propagating Gravity Wave.....43	
1. Introduction.....	43
2. Methodology.....	44
3. TKE Budget Analysis: 12 December 2002 STRATONHMASS Simulation in Pressure Coordinates.....	49
4. Future Work.....	68
5. Conclusions.....	69
6. Summer 2005 Research Update.....	69
References.....	87

Figures

1. NWS radar summary valid at 2315 UTC, 12 December 2002.....	6
2. GPS mean sea level pressure (mb) at Palestine, Texas, valid from 12/0100 UTC – 15/0000 UTC, December 2002.....	6
3. (a) Winds (m/s) from vertically profiling radars at Palestine, Texas, every hour 1600 UTC – 0300 UTC, 12-13 December 2002, from right to left and (b) Winds (m/s) from vertically profiling radars at Palestine, Texas every 6 minutes from 2254 UTC - 0000 UTC, 12 -13 December 2002, from right to left.....	7
4. Grid mesh locations for the 6-km, 2-km, 667-m, 222-m, and 71-m STRATONHMASS model runs.....	9
5. Comparison of 18-km STRATONHMASS simulated 300-mb isoheights (m) and isotachs (knots) [top] with analyzed observed isotachs (knots) [bottom] valid at 0000 UTC, 13 December 2002.....	10
6. Comparison of 18-km STRATONHMASS simulated 150-mb isoheights (m) and isotachs (knots) [top] with analyzed observed isotachs (knots) [bottom] valid at 0000 UTC, 13 December 2002.....	11
7. 6-km STRATONHMASS 300-mb isoheights (m) and isotachs (knots) valid at 2300 UTC, 12 December 2002.....	12
8. 2-km STRATONHMASS simulated mean sea level pressure (mb) and surface winds (knots) valid at 2300 UTC, 12 December 2002.....	13
9. 222-m STRATONHMASS simulated 1-minute precipitation (mm) and surface winds (knots) valid at 2230 UTC, 12 December 2002.....	14
10. 222-m STRATONHMASS simulated 100-mb NCSU1 index ($s^2 \times 10^{-9}$) valid at 2230 UTC, 12 December 2002.....	14
11. 222-m STRATONHMASS vertical cross section from 30.42 N, -93.92 W and 30.42 N, -93.67 W. Isentropes (K) and isotachs (knots) valid at 2224 UTC, 12 December 2002.....	15
12. Same as Figure 11, but at 2227 UTC, 12 December 2002.....	16
13. Same as Figure 12, but at 2230 UTC, 12 December 2002.....	16

14. 222-m STRATONHMASS Scorer parameter (solid; m^{-2}) and eddy dissipation rate (dashed; $m^2 s^{-3}$) valid at the middle point of cross section in Figure 13 at 2233 UTC, 12 December 2002.....	17
15. Same as Figure 11, but at 71-m resolution orthogonal to cross-section in Figure 13, at 2238 UTC [top] and 2239 UTC [bottom], 12 December 2002.....	18
16. Same as Figure 14, but from the 71-m simulation valid at 2239 UTC, 12 December 2002.....	19

1. SUMMARY

A mesoscale numerical modeling system is adapted for use into the lower stratosphere. The model is tested and an automated grid-nesting scheme is developed and tested with observed initial data. The purpose of the model and the new nesting scheme is to improve the prediction of regions in which possible severe aviation turbulence occurs within the lower stratosphere. Simulation results show a possible link in the process of stratospheric turbulence to convectively generated large amplitude gravity waves that eventually propagate into the lower stratosphere and break. The grid-nesting scheme is tested to determine its potential utility.

2. INTRODUCTION

The operational forecasting of tropospheric turbulence has been ongoing for several years. Many indices are generated daily from operational numerical weather prediction models. The National Weather Service (NWS) has employed the Ellrod Index (Ellrod and Knapp 1992), the National Oceanic and Atmospheric Administration Forecasting Systems Laboratory (NOAA-FSL) has employed indices developed by Marroquin (1998) based on turbulence kinetic energy and eddy dissipation rate, and the Research Applications Program of the National Center for Atmospheric Research (NCAR-RAP) employs the Graphical Turbulence Guidance index as part of the suite of products from the NWS Rapid Update Cycle (RUC) II model (Sharman, Wiener, and Brown 2000). These systems are designed for use in the troposphere and are not strongly coupled to the model, i.e., indices are simply calculated from model-generated dependent variables and any grid nesting algorithms are independent of the case study and ongoing simulated fields, which the models produce.

The processes that create turbulence in the stratosphere are likely coupled to the troposphere as energy regularly is exchanged by vertically propagating internal gravity waves between the two atmospheric regions. This vertical coupling is greatly facilitated during moist convection or the development of large amplitude mountain waves as these local circulations are capable of modifying their immediate environment thus resulting in three-dimensional fluxes of energy. The magnitude of the vertical flux of energy is, therefore, a function of the kinematic and thermodynamical fields that evolve in response to convective motions, i.e., the perturbed static stability and vertical wind shear environments surrounding moist or dry convection. Simulating stratospheric turbulence is an extraordinarily demanding problem because of this vertical coupling as well as the fine scale and transient nature of turbulence itself. Therefore, to develop an automated system for the operational prediction of lower stratospheric turbulence potential will require at least three fundamental advances in mesoscale numerical weather prediction: 1) a model with significant vertical resolution spanning the mid-upper troposphere and lower stratosphere in order to resolve the vertical coupling, 2) a model with a "smart" grid nesting scheme that can focus on the regions of high turbulence potential based on scale dependent dynamical indices that can adapt to the favorable turbulence forcing processes that vary in space and time from one case study to another, and 3) a model which exploits as much of the observed data as possible in its initial conditions and lateral boundary

conditions to improve the accuracy of its simulation. We are modifying a modeling system to improve the automated prediction of lower stratospheric regions of turbulence potential in which we incorporate all three of these improvements. During year one, the focus was on testing the quality of the model with its vertical lid extended to 10 mb and its response to readily available conventional gridded data sets in its initial state. Additionally, work commenced on formulating, coding and testing an automated grid nesting scheme or *autonest* based on an original algorithm.

3. METHODS, ASSUMPTIONS AND PROCEDURES

The first research task (Task 1) involved extending the model lid and modifying the vertical structure of the Non-Hydrostatic Mesoscale Atmospheric Simulation System (NHMASS) model version 6.3 (note Table 1) (e.g., Kaplan et al. 2000). This modeling system was turned into a stratospheric modeling system, i.e., STRATONHMASS by extending the model lid to 10 mb, increasing the number of vertical levels to 90 and modifying its preprocessor to ingest observational data in the lower stratosphere, i.e., up to ~10 mb or ~30 km. This resulted in an average vertical thickness of model layers of ~300 m with a nonuniform vertical focus of resolution within the lower stratosphere.

Table 1. STRATONHMASS (Version 6.3)

Initialization
<ul style="list-style-type: none"> • 3-D multivariate OI procedure used to blend a first guess fields (e.g., previous MASS simulation, NCEP model output, archived Reanalysis data) with observations from a variety of sensing systems (e.g., surface, rawinsonde) • Global databases of terrain height, land cover/land use, vegetation index, sea surface temperature, soil texture, snow cover, soil moisture, subsurface temperature, and sea ice
Numerical Techniques
<ul style="list-style-type: none"> • Option of hydrostatic or non-hydrostatic primitive equations in terrain-following (σ_p) vertical coordinate with 4th-order accurate finite differencing • MPDATA positive definite advection scheme • Option of one-way or two-way interactive nesting, with arbitrary coarse/fine grid spacing ratio and unrestricted number of nested domains for one-way nesting
Boundary Layer/ Surface Physics
<ul style="list-style-type: none"> • 1.5 order Turbulence Kinetic Energy (TKE) parameterization with surface layer based on similarity theory formulation • Surface energy budget with option of isothermal or non-isothermal soil-vegetation canopy formulations and heterogeneous subgrid scale areas • Surface hydrology includes budget equations for three moisture reservoirs (cover layer, shallow and deep soil layers) and snow cover which incorporates the effects of accumulation, settling, melting and sublimation
Moisture Physics
<ul style="list-style-type: none"> • Option of diagnostic or three prognostic schemes with varying levels of sophistication. Prognostic equations for cloud water, cloud ice, rain water, snow and hail using a bulk microphysics parameterization • Option of Kuo-type cumulus parameterization with moist downdraft physics, Fritsch-Chappell scheme, Kain-Fritsch scheme or Grell scheme
Radiation
<ul style="list-style-type: none"> • Longwave and shortwave radiation parameterized in surface energy budget and in the free atmosphere. Interaction with atmospheric water vapor, liquid/frozen water, and parameterized sub-grid clouds

The second research task (Task 2) involved testing the new model on case studies wherein deep moist convection, large amplitude gravity waves as well as possible terrain-induced wave phenomena existed. A diverse group of case studies was simulated in an effort to test the reliability of the model with its vertically extended grid as well as the utility of conventional gridded and rawinsonde observations in the lower stratosphere. This involved producing nested-grid numerical simulations with STRATONHMASS for four different case studies: 1) a convectively-generated large amplitude gravity wave propagating on a well-developed duct, 2) a winter snowstorm with imbedded gravity and mountain waves, 3) a tropical system with possible large amplitude gravity waves and deep convection, and 4) a winter snowstorm with well-developed maritime convection and possible large amplitude gravity waves. These case studies were nested employing the newly developed autonesting code and the simulations were validated against all available conventional and many forms of synoptic data including wind profilers, Doppler radar and satellite datasets containing Advanced Microwave Sounding Unit (AMSU) data. Validation indicated reasonable model simulation of large-scale stratospheric winds and temperatures as well as clouds and precipitation.

Consistent with the generation of the four sets of nested-grid simulations, the development of a primitive autonest code was undertaken. The autonest code development was accompanied by the analyses of model-generated dynamical processes that resulted in the focusing of high frequency wave energy in the lower stratosphere both of which served as research Tasks 3 and 4. The coarse mesh 18-km numerical simulations were nested to 6-km, 2-km, 667-m, 222-m and 71-m horizontal resolution. The first generation of the autonest code employed the NCSU1 index (e.g., Kaplan et al. 2004). This was coded to nest in a region and time based on 100-mb NCSU1 threshold values. The second generation of autonest was being coded to nest based on the NCSU1 index at all grid resolution simulations ≥ 2 km and then to employ the Scorer Parameter variation in the vertical at horizontal resolutions below 2 km. The third generation of autonest was being coded to nest based on threshold values of eddy dissipation rate (EDR) from the complete turbulence kinetic energy equation at all grid resolutions below 222-m horizontal resolution. These equations are listed below.

$$\text{NCSU1 Index} = \left[\vec{U} \bullet \nabla \vec{U} \right] \frac{|\nabla \zeta|}{|Ri|} \quad (1)$$

$$\text{Scorer Parameter} = \frac{N^2}{U^2} - \frac{U_{zz}}{U} \quad (2)$$

$$\begin{aligned} \text{EDR} = & -u \frac{\partial \bar{e}}{\partial x} - v \frac{\partial \bar{e}}{\partial y} - w \frac{\partial \bar{e}}{\partial z} + \frac{g}{\theta_v} \overline{(w' \theta_v')} \\ & - \overline{(u' w')} \frac{\partial \bar{u}}{\partial z} - \frac{\partial}{\partial z} (\overline{w' e}) - \frac{1}{\rho} \frac{\partial}{\partial z} (\overline{w' p'}) - \frac{\partial \bar{e}}{\partial t} \end{aligned} \quad (3)$$

Task 5 involved initial testing of code that will be used to improve the initial asynoptic remotely-sensed data to be employed in the model's initial conditions. This will focus on relative humidity data derived from infrared cloud top temperatures.

Task 6 involved modifying a version of the turbulence kinetic energy equation for use in the autonesting scheme so that the most comprehensive representation of the eddy dissipation rate can be calculated. This involved adding the advective terms to make the equation complete, as is described in Appendix B.

Finally, Task 7 involved several required Air Force Research Laboratory reports, two conference preprints and two journal articles, which were prepared or were in the process of being prepared at the end of year one in an effort to document the research.

4. RESULTS AND DISCUSSION

As noted in Appendices A and B, the paradigm developed to modify and implement successive generations of the autonest code is based on simulated dynamical adjustment processes in the lower stratosphere. Two case studies, in particular, have been used to test the paradigm, i.e., the 12-13 December 2002 convective gravity wave event and the 16-17 February 2003 Mid-Atlantic extreme snowfall event. Additionally, the landfall of tropical storm Gaston during 30-31 August 2004 and the 24-25 January 2000 Mid-Atlantic coastal storm were also being simulated. In both extensively simulated case studies, i.e., 12-13 December 2002 and 16-17 February 2003, large amplitude internal gravity waves occur, due in part to the development of an unbalanced jet streak exit region (e.g., Uccellini and Koch 1987; Kaplan et al. 1997).

The 16-17 February 2003 snowstorm, and its potential implications for stratospheric turbulence, is discussed in detail in Appendix A. In this section of the report we will describe the large amplitude gravity wave case study of 12-13 December 2002 wherein mesoscale convective systems developed above a stable layer. The turbulence kinetic energy diagnostics calculated for this case study are depicted in Appendix B. In this section we will focus on the scale contraction process that results in stratospheric wave amplification and breaking, necessitating the turbulence kinetic energy analysis in Appendix B.

Figure 1 depicts the radar imagery valid at 2315 UTC, 12 December 2002. The large convective complex system located across eastern Texas and Louisiana originated over the southern Texas Gulf coast at about 1630 UTC, 12 December. Collocated with this convective complex and its propagation across eastern Texas north of a stable layer, is the large amplitude gravity wave diagnosed in the NOAA Global Positioning System (GPS) microbarogram in Figure 2 at Palestine (PAL), in southeastern Texas. The microbarogram indicates a wave of depression associated with a nearly 6-mb pressure fall in about two hours just before 2230 UTC. This fall is a likely signal of a large amplitude gravity wave based on this single station trace as well as other GPS traces in eastern Texas and Louisiana, which show similar temporally coherent signals. Thus, even in the absence of a detailed surface covariance analysis, inferential observational proof of the wave exists which will be bolstered by the mesoscale simulations.

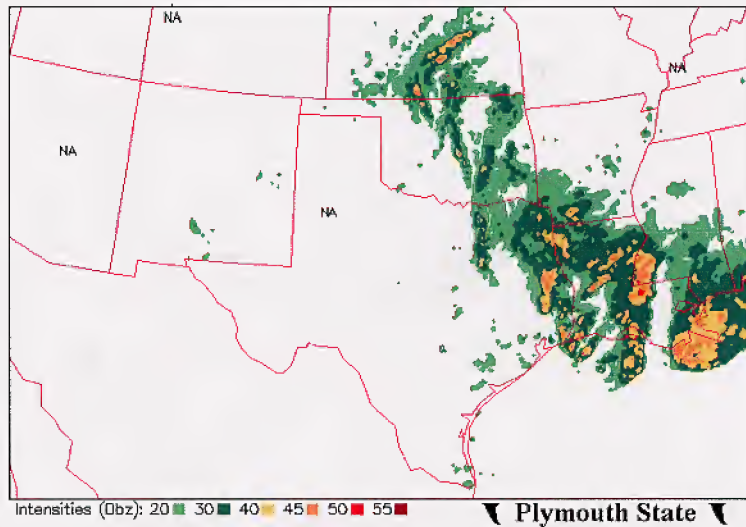


Figure 1. NWS radar summary valid at 2315 UTC, 12 December 2002.

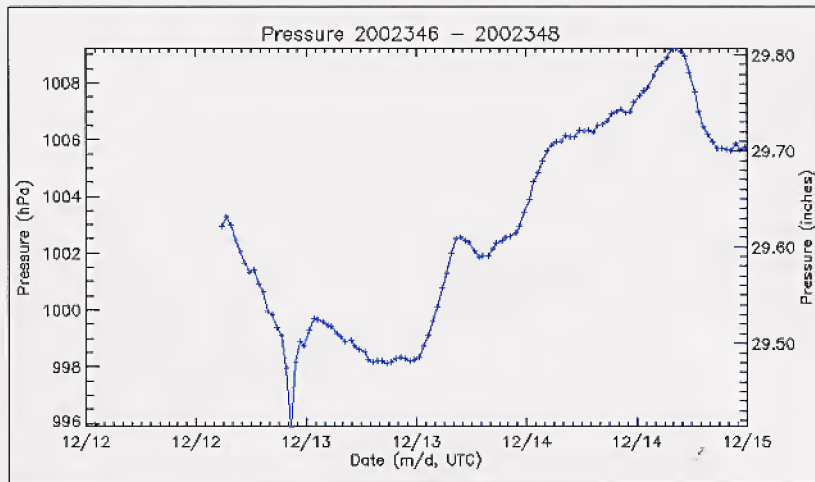


Figure 2. GPS mean sea level pressure (mb) at Palestine, Texas, valid from 12/0100 UTC – 15/0000 UTC, December 2002.

Winds from profiling radars at Palestine are depicted in Figures 3 (a) and (b) at hourly and 6-minute time intervals. The time of wave passage in the pressure data was shortly before 2230 UTC. It is during this period that the 6- to 10-km winds in the hourly data show acceleration and turning from southwest to south. Above this level, there is a brief acceleration to the west, particularly at about 150 mb or ~14 km, which is in the lower stratosphere immediately above the tropopause. The 6-minute data confirms an increase from the west and then decrease of westerly flow at that level after about 2330 UTC when the wave of depression was located well east of Palestine in microbarograms in southwestern Louisiana.

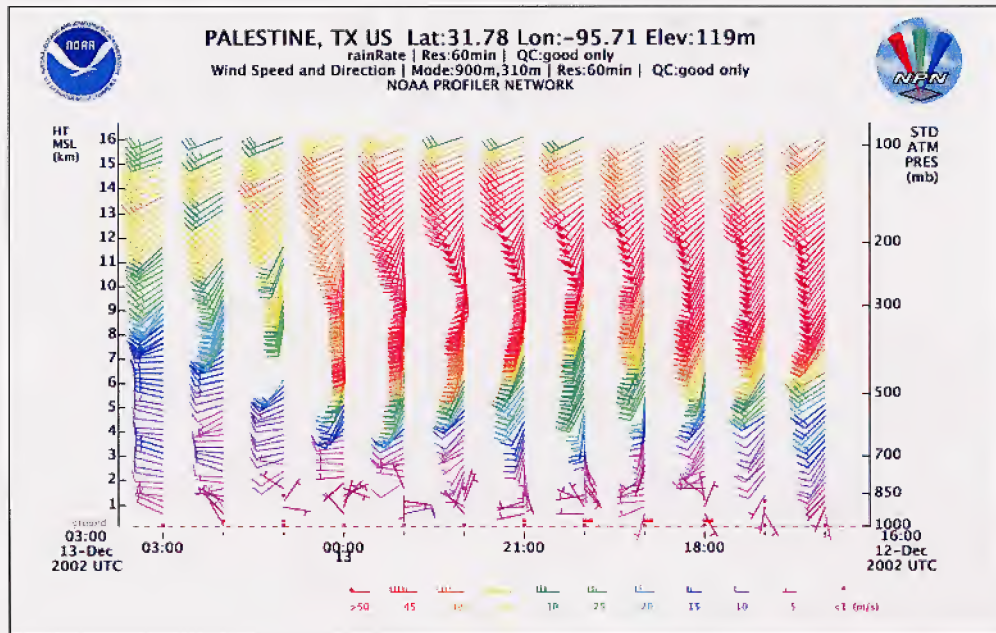


Figure 3(a). Winds (m/s) from vertically profiling radars at Palestine, Texas, every hour 1600 UTC – 0300 UTC, 12-13 December 2002, from right to left.

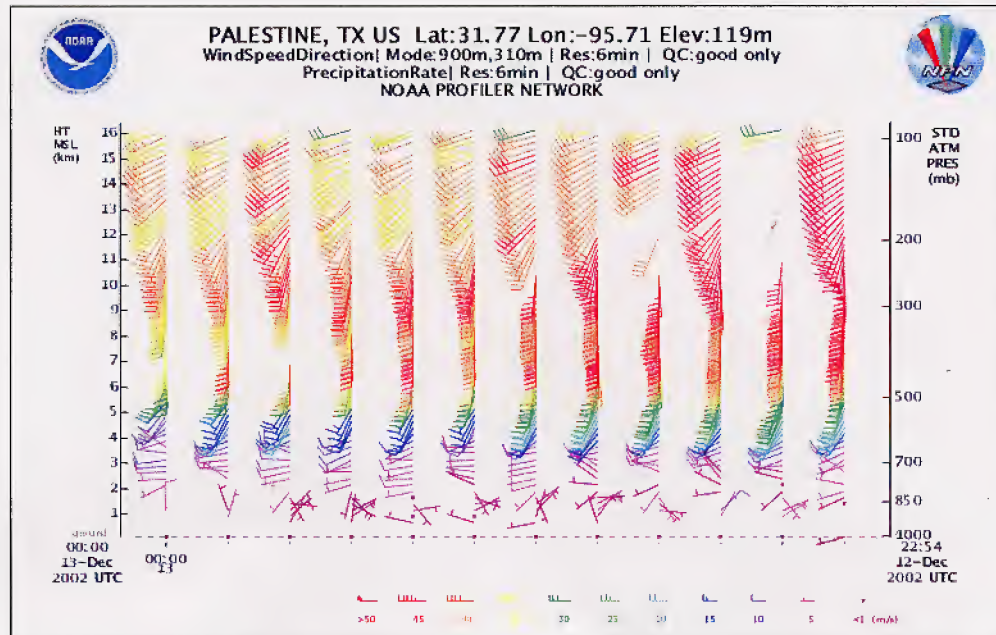


Figure 3(b). Winds (m/s) from vertically profiling radars at Palestine, Texas, every 6 minutes from 2254 UTC - 0000 UTC, 12 -13 December 2002, from right to left.

The inferences to be drawn from all these data are: 1) that convection was fairly closely related to the wave of depression and 2) that the wave/convective system likely played some role in modifying the winds aloft above and below the tropopause. This can be seen in the accelerating of the flow below the tropopause, followed by a deceleration in velocities below the tropopause, as well as accelerations above the tropopause nearly coincident with the lower layer deceleration. This is analogous to the wave and its attendant convective heating acting to vertically expand the height of the previous background jet stream flow or to force a vertical mass convergence between 6 and 14 km. This process, therefore, should likely result in the evacuation/decrease of horizontal momentum at 300 mb and increase of momentum at 150 mb on or about 0000 UTC, 13 December 2002. The consequence is that southerly momentum is being forced upwards from the lower troposphere and westerly momentum is being forced upwards from the upper troposphere being forced into the lower stratosphere while the down and upstream flows are being modified as well. This restructuring of the flow can be further confirmed by viewing rawinsonde-based gridded wind analyses depicted in Figures 5 and 6. Thus, the wave and its attendant/nearly collocated diabatic forcing are acting to vertically expand the level of momentum shears both upward and outward in 3-dimensional space from their pre-convective levels in the vertical and, therefore, acting to modify the wind shears in the lower stratosphere. This is all accompanying the convectively induced energy fluxes that were hypothesized earlier to be critical to generating stratospheric wave breaking.

In an effort to test the new stratospheric model and the first generation autonest code, a sequence of numerical simulations were performed with the model employing a three-dimensional grid matrix of 162x162x90 points. Figure 4 depicts the 6-km, 2-km, 667-m, 222-m, and 71-m regions of model integration for this 12-13 December 2002 case study, all of which were embedded within the 18-km grid, which covered much of the continental U.S. The model coarse mesh grid was initialized at 0000 UTC, 12 December 2002, from NCEP Reanalysis gridded data and reanalyzed rawinsonde and surface observations. Each finer mesh simulation was integrated for a progressively shorter period of time centered on and consistent with wave passage near the Texas/Louisiana border region. The initial conditions and lateral boundary conditions were derived from each successively coarser mesh model simulation for a one-way nested-grid configuration.

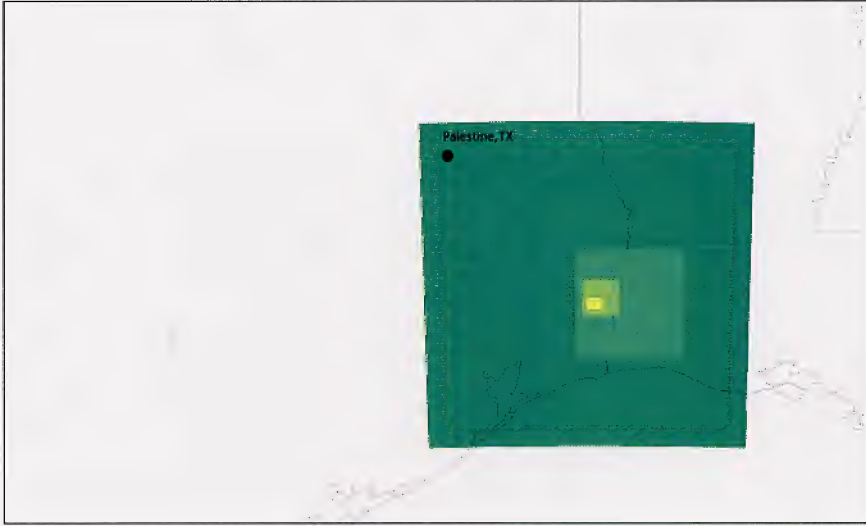


Figure 4. Grid mesh locations for the 6-km, 2-km, 667-m, 222-m and 71-m STRATONHMASS model runs.

Figures 5 and 6 depict the 18-km wind validation against the rawinsonde observations at 300 and 150 mb. Most notable in the simulations is the previously-referenced decelerating flow at 300 mb and accelerating flow at 150 mb near the Texas/Louisiana border at 0000 UTC, 13 December. This is deduced from the apparent 300-mb wind minimum near the convection in east Texas and maximum in the jet entrance region aloft at 150 mb in the same region. The timing is consistent with gravity wave and mesoscale convective system passage through this region just southeast of Palestine, Texas. The model replicates the general pattern of stronger winds at 150 mb relative to that at 300 mb consistent with observed data in this region. As such, the vertical wind shear above the tropopause, i.e., within the 25- to 50-mb deep layer centered on 150 mb, is likely very large due to the expansion/vertical and horizontal convergence of the momentum field above the convective heating. This increased wind shear above the wave is consistent with the 6-km simulated 300-mb winds in Figure 7 wherein the momentum has been depleted at 300 mb and forced upward and outward into a new highly ageostrophic jet entrance region to the north and west of, as well as above, the simulated and observed convection. Hence, the diabatic heating is forcing kinetic energy fluxes both into the stratosphere and upstream to the north and west of the surface wave signal in the simulated fields. This can be seen by comparing Figures 7 and 8 with the 2-km nested-grid mean sea level pressure trough and ridge accompanying the wave near the Texas/Louisiana border region and its highly ageostrophic surface flow, which lies just southeast of the depleted flow at 300 mb. Hence, tilting backward from the simulated surface wave is a kinetic energy minimum at 300 mb and maximum above the tropopause reflecting the phase shift of kinetic energy adjustments to the convectively-induced heating.

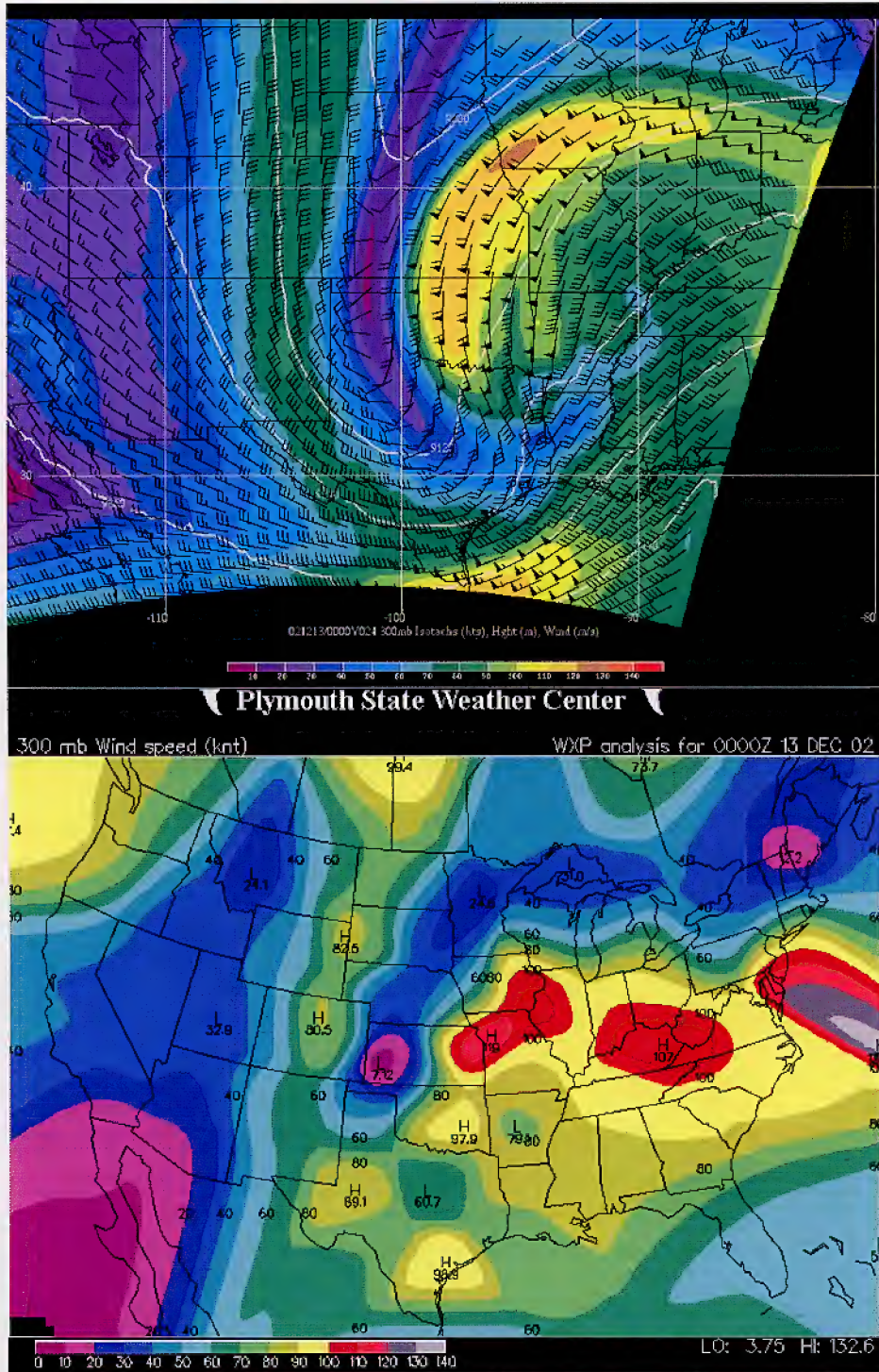


Figure 5. Comparison of 18-km STRATONHMASS simulated 300-mb isoheights (m) and isotachs (knots) [top] with analyzed observed isotachs (knots) [bottom] valid at 0000 UTC, 13 December 2002.

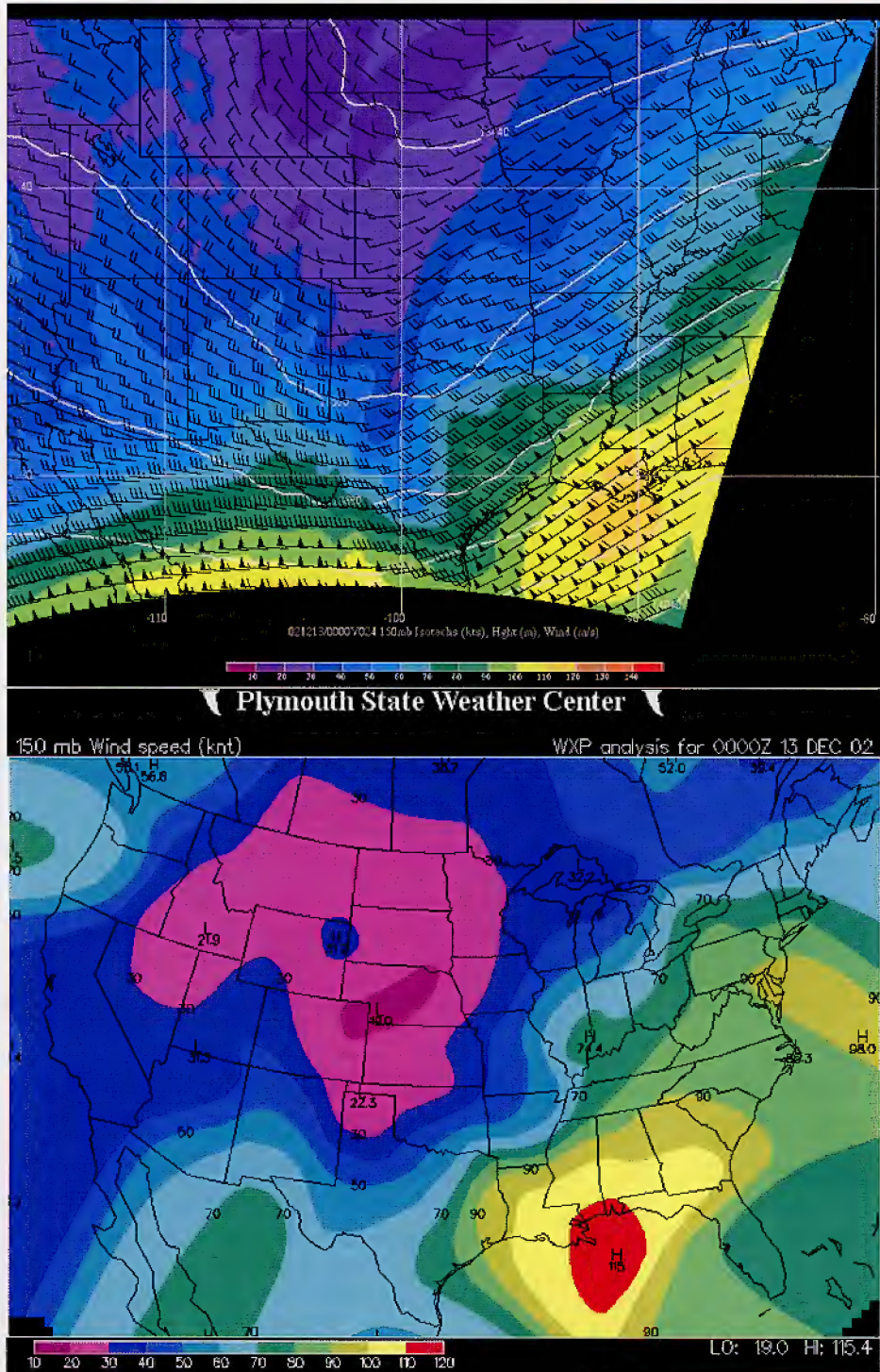


Figure 6. Comparison of 18-km STRATONHMASS simulated 150-mb isoheights (m) and isotachs (knots) [top] with analyzed observed isotachs (knots) [bottom] valid at 0000 UTC, 13 December 2002.

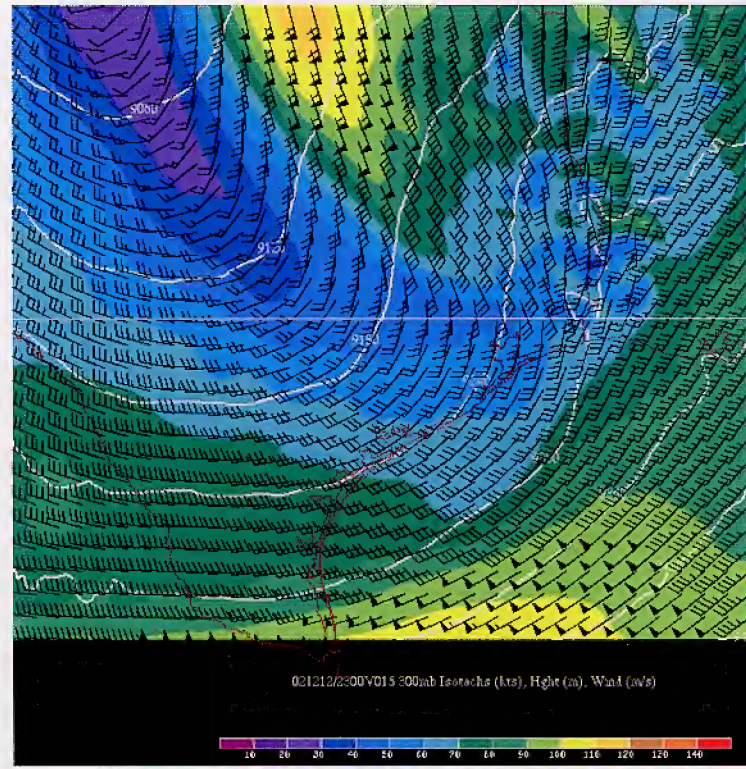


Figure 7. 6-km STRATONMASS 300-mb isoheights (m) and isotachs (knots) valid at 2300 UTC, 12 December 2002.

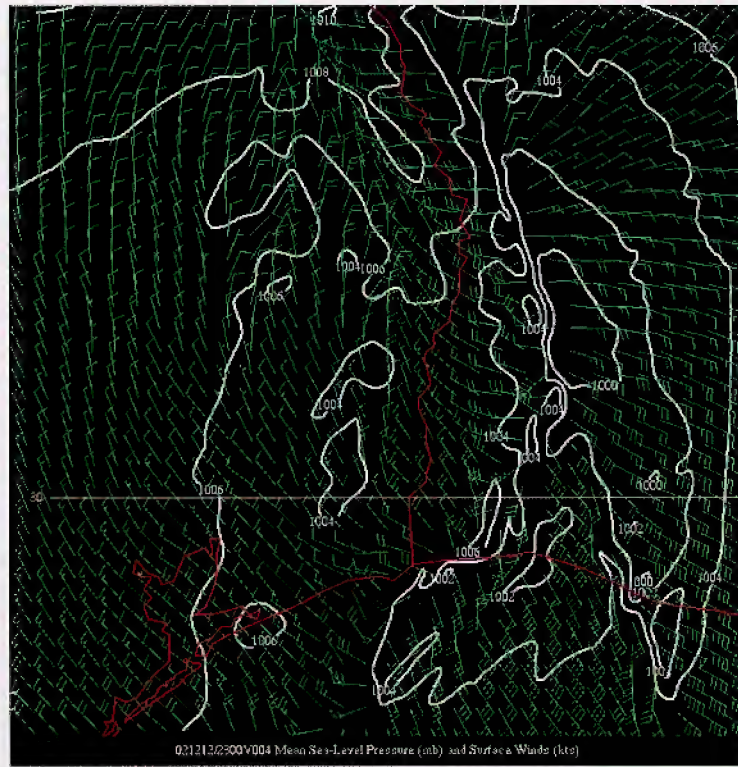


Figure 8. 2-km STRATONHMASS simulated mean sea level pressure (mb) and surface winds (knots) valid at 2300 UTC, 12 December 2002.

Further simulated proof of this sloping shear zone and its implication for stratospheric turbulence can be gleaned from Figures 9 and 10, which depict very high resolution, i.e., 222 m, simulated precipitation and surface winds as well as the 100 mb NCSU1 index. Note how the turbulence index at 100 mb is displaced well upstream/northwest from the precipitation. This signal of large index values is consistent with the discontinuous advection of streamwise momentum, vorticity gradients, vertical wind shear and decreased static stability maximizing many kilometers to the northwest of the border and to the northwest of the ongoing simulated precipitation. Thus, the region of potential horizontal flow bifurcation and vertically propagating wave structures may maximize well displaced in space and time from the actual convective heating. The horizontal flow bifurcation and subsequent vertically propagating gravity wave energy resulting from the shear and instability are likely caused by the temporally integrated effects of convection on the environmental dependent variables rather than at the location of the convection itself.

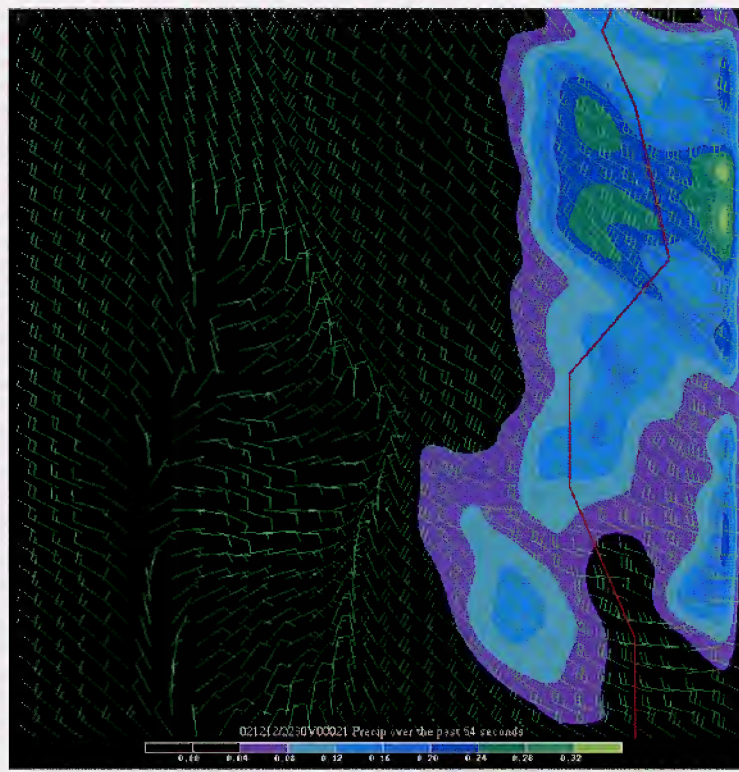


Figure 9. 222-m STRATONHMASS simulated 1-minute precipitation (mm) and surface winds (knots) valid at 2230 UTC, 12 December 2002.

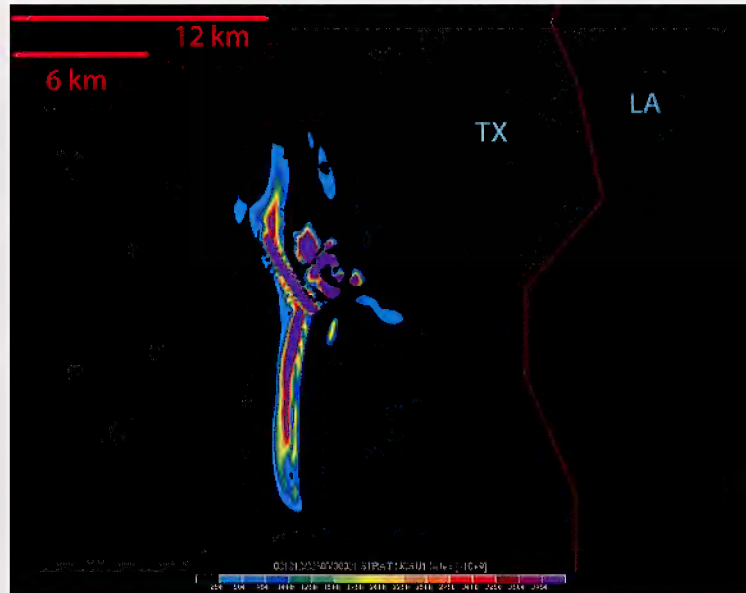


Figure 10. 222-m STRATONHMASS simulated 100-mb NCSU1 index ($s^{-2} \times 10^{-9}$) valid at 2230 UTC, 12 December 2002.

To visualize the consequence of these processes better at the finest scales of motion, a vertical cross section corresponding to cross section M depicted in Appendix B, is oriented west to east as can be seen with simulated isentropes and isotachs depicted in Figures 11-13 for three time periods separated by three minutes each from 0015 -0021 UTC. The location of the cross section bisects the high values of NCSU1 depicted in Figure 10 along a west – east axis. The isentropic perturbation above the wind shear zone near 90 mb is consistent with a vertically varying value of the Brunt-Vaisalla frequency and the second derivative of wind with respect to height just above the tropopause. These shear and stability terms control vertical fluctuations in the stability and wind shear consistent with a transition region between wave trapping and critical layer formation, i.e., where the value of the Scorer parameter changes signs from positive to negative in the vertical. Critical layer theory dictates that wave breaking would be ongoing where the Scorer parameter decreases to less than zero in such a region. The wave amplification and overturning seen in Figures 11-13 are consistent with shearing instability occurring where a convective outflow jet has modified the lower stratosphere. The model is predicting wave breaking here, hence it is a region where the autonesting code should sense the increase in Scorer parameter variation and its possible organization of local shear and buoyancy maxima ideal for the generation of turbulence kinetic energy. The correspondence between this vertically varying zone of Scorer parameter and increasing eddy dissipation rate can be seen depicted at the grid point in Figure 14. At approximately 90 mb, i.e., the level of wave breaking, the local increase in turbulence kinetic energy will force the model autonest code to flag this location as ideal at this time for nesting to 71 m.

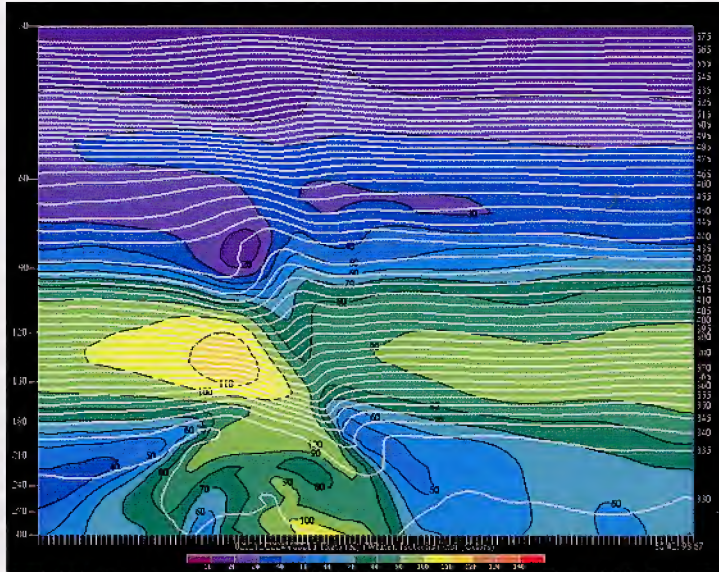


Figure 11. 222-m STRATONHMASS vertical cross section from 30.42 N, -93.92 W and 30.42 N, -93.67 W. Isentropes (K) and isotachs (knots) valid at 2224 UTC, 12 December 2002.

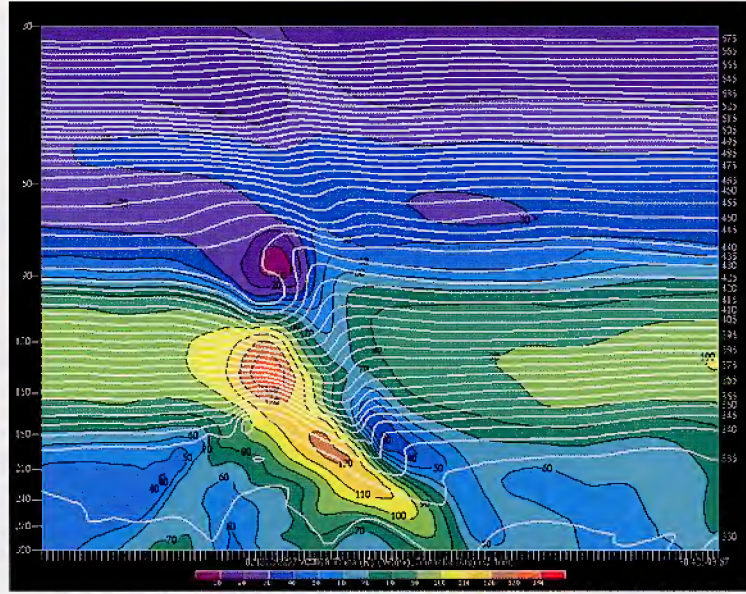


Figure 12. Same as Figure 11, but at 2227 UTC, 12 December 2002.

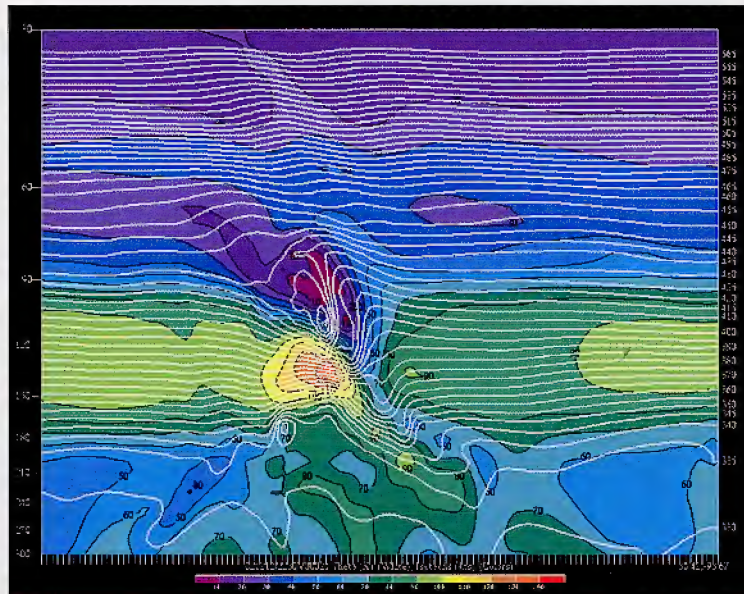


Figure 13. Same as Figure 12, but at 2230 UTC, 12 December 2002.

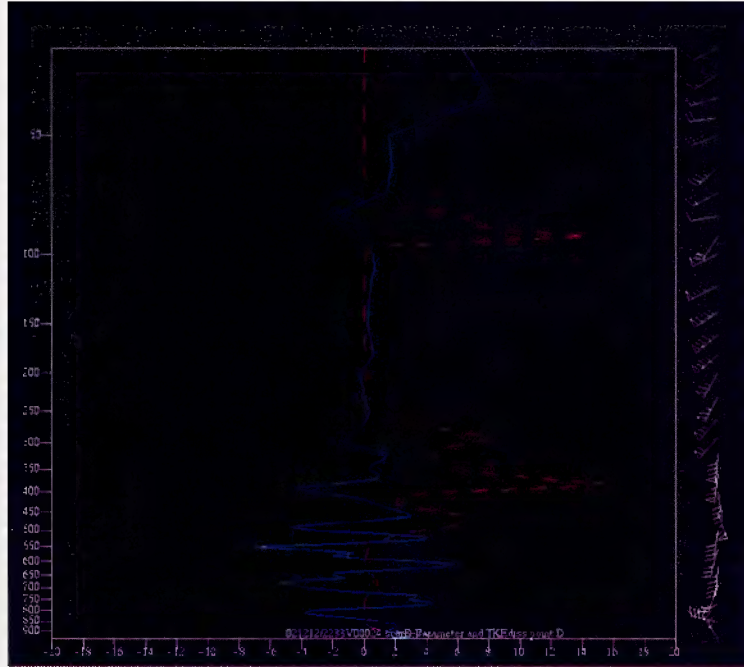


Figure 14. 222-m STRATONHMASS Scorer parameter (solid; m^{-2}) and eddy dissipation rate (dashed; $\text{m}^2 \text{s}^{-3}$) valid at the middle point of cross section in Figure 13 at 2233 UTC, 12 December 2002.

The nested grid 71-m cross section (M2) of simulated isentropes and isotachs oriented nearly orthogonal to cross section M in Figures 11-13 is depicted in Figure 15 at 0024 and 0025 UTC, 12 December 2002. The maximum vertical variation of Scorer parameter in the stratosphere near 90 mb can be seen in Figure 16 with the superimposed vertical variation of eddy dissipation rate at the same time and level from the 71-m simulation. This orthogonal cross section depicts shallower cross-wave instabilities along the periphery of the feature in Figures 11-13. Such possible regions of wave breaking and turbulence may be validated against AMSU data in the near future if such data is available from NOAA.

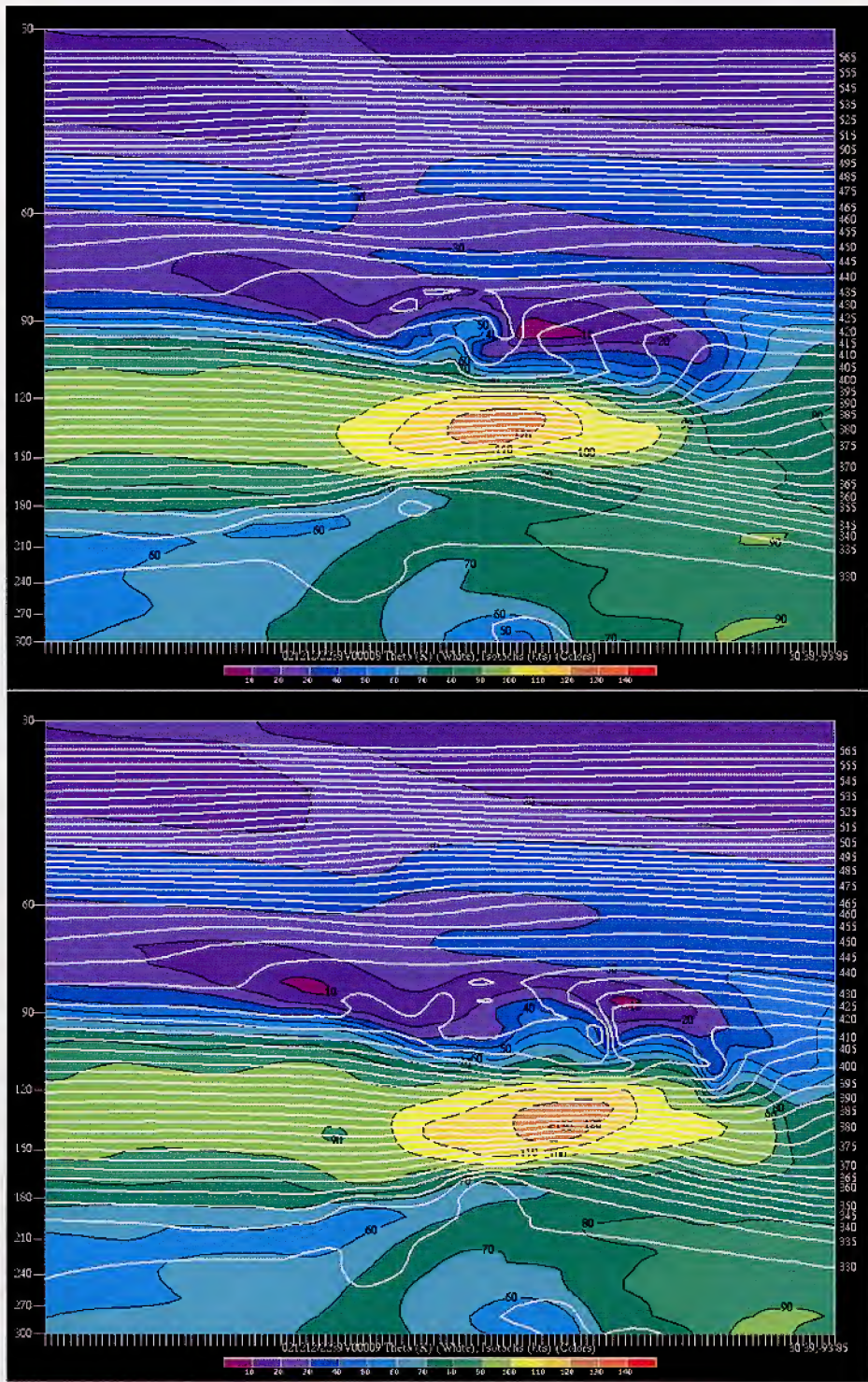


Figure 15. Same as Figure 11, but at 71-m resolution orthogonal to cross section in Figure 13, at 2238 UTC [top] and 2239 UTC [bottom], 12 December 2002.

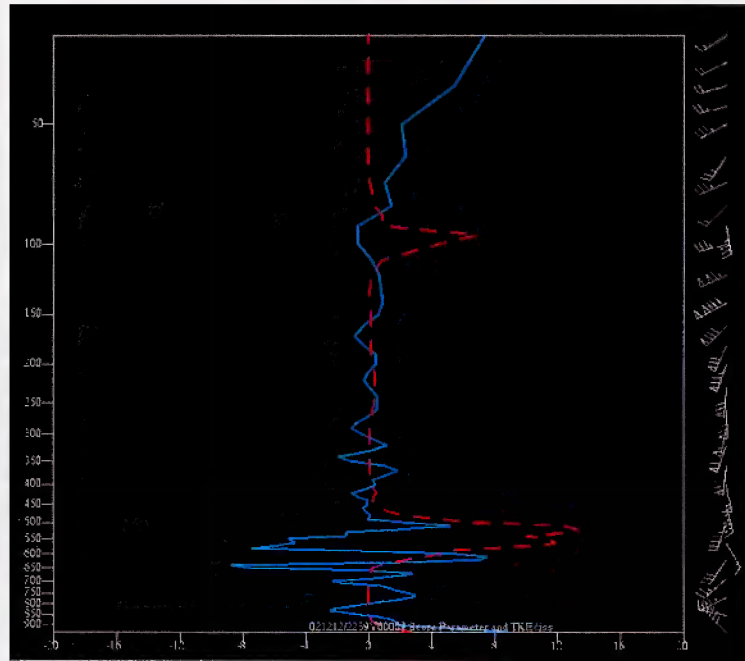


Figure 16. Same as Figure 14, but from the 71-m simulation valid at 2239 UTC, 12 December 2002.

5. CONCLUSIONS

The first year of research showed major progress towards the development of a stratospheric real-time turbulence modeling system. During this period, the NHMASS model was tested with the lid raised well into the stratosphere on four research case studies. Results of the simulated fields were satisfactory when validated against conventional and asymptotic observations. An autonest algorithm was formulated and tested on these four case studies. The ability of the model to simulate fine scale convective features and wave phenomena, as well as the autonest to direct the model grid nests to finer scales in regions of convectively modified circulations, indicates the potential for use in turbulence generating regions. However, validation of the modeling system lags its development and testing due to the lack of stratospheric turbulence observations.

6. RECOMMENDATIONS

There is a need for information concerning observed turbulence reports in the lower stratosphere in the existing simulated and future simulated case studies to validate the modified and evolving modeling system.

REFERENCES

- Ellrod, G. P., and Knapp, D. I., 1992: An objective clear air turbulence forecasting technique: Verification and operational use. *Wea. Forecasting*, **7**, 150-165.
- Kaplan, M. L., S. E. Koch, Y.-L. Lin, R. P. Weglarz, and R. A. Rozumalski, 1997: Numerical simulations of a gravity wave event over CCOPE. Part I: The role of geostrophic adjustment in mesoscale jetlet formation. *Mon. Wea. Rev.*, **125**, 1185-1211.
- Kaplan, M. L., Y.-L. Lin, J. J. Charney, K. D. Pfeiffer, D. B. Ensley, D. S. DeCroix, and R. P. Weglarz, 2000: A Terminal Area PBL Prediction System at Dallas-Fort Worth and its application in simulating diurnal PBL jets. *Bull. Amer. Meteor. Soc.*, **81**, 2179-2204.
- Kaplan, M. L., K. M. Lux, J. D. Cetola, A. W. Huffman, A. J. Riordan, S. W. Slusser, Y.-L. Lin, J. J. Charney, and K. T. Waight, 2004: Characterizing the severe turbulence environments associated with commercial aviation accidents. A Real-Time Turbulence Model (RTTM) designed for the operational prediction of hazardous aviation turbulence environments. NASA/CR-2004-213025.
- Marroquin, A., 1998: An advanced algorithm to diagnose atmospheric turbulence using numerical model output. *Preprints, 16th AMS Conference on Weather Analysis and Forecasting*, 11-16 January, 79-81.
- Sharman, R., G. Wiener and B. Brown, 2000: Description and integration of the NCAR integrated turbulence forecasting algorithm (ITFA). *AIAA 00-0493*.
- Uccellini, L. W., and S. E. Koch, 1987: The synoptic setting and possible source mechanisms for mesoscale gravity wave events. *Mon. Wea. Rev.*, **115**, 721-729.

Appendix A

Inertia-Gravity Wave Breaking and Lower-Stratospheric Turbulence During the 2003 Presidents' Day Event

1. INTRODUCTION

Atmospheric turbulence is both a significant threat to aviation throughout the United States and an extremely difficult phenomenon to observe and forecast, making turbulence one of the more critical research topics in atmospheric science. Between 1986 and 1993, close to 1000 people were injured as a result of turbulence impacting aircraft (Cowen 1998), and for commercial airliners alone, tens of passengers are injured each year (Lane et al. 2003). The small spatial and temporal scale of turbulence limits both the observation and accurate forecasting of atmospheric turbulence. Cetola (2003) points out that the identification of large-scale precursors of turbulence is a necessary step in order to predict turbulence using the relatively course observational data commonly available. Turbulence has been shown to have a wide variety of sources, including mountain wave breaking, wind shear-induced Kelvin-Helmholtz instabilities, overshooting convective updrafts, and inertia-gravity wave breaking. The purpose of this study is to relate the development of inertia-gravity waves to the simulated development of stratospheric turbulence over portions of West Virginia and western Maryland during the 2003 Presidents' Day winter storm of 16-17 February 2003. Since limited observational data is available to validate the existence of apparent inertia-gravity wave activity over the study region, the majority of this study makes use of a mesoscale numerical model, the Non-Hydrostatic Mesoscale Atmospheric Simulation System (NHMASS) version 6.3 (Kaplan et al. 2000) to evaluate the complex non-linear dynamics resulting in the transition of mesoscale wave activity to turbulence.

Inertia-gravity wave sources have been shown to include shearing instability, convection, and geostrophic adjustment (Uccellini and Koch 1987). The latter mechanism will be evaluated in this paper due to the elimination of the first two mechanisms in analyses of NHMASS fields (not shown), and the presence of a strongly unbalanced subtropical jet (STJ) exit region immediately upstream of the region of propagating wave activity. Methods of distinguishing inertia-gravity wave activity from other mesoscale banded phenomena, including quadrature between mid-tropospheric potential temperature (θ) and vertical velocity (w) fields, and evaluating the in-phase relationship between the surface fields of perturbation pressure (p') and wave-normal horizontal wind speed (u^*) (Koch and Golus 1988) will be evaluated to partially validate the classification of the phenomena observed as inertia-gravity wave activity.

High-resolution simulations will be used to analyze the transition to turbulence in the lower stratosphere, evaluating the process of wave overturning, generation of fine-scale instabilities, and the rapid development of turbulence. Lastly, a number of turbulence measurements, including turbulence kinetic energy (TKE) dissipation and the NCSU1 index, an index sensitive to horizontal gradients of momentum and low Richardson number values, will be utilized in assessing turbulence in the simulations.

2. MODEL DESCRIPTION

Due to the lack of observational data available at a scale necessary to resolve the mechanisms discussed in this paper, a mesoscale model is employed for dynamical analysis. The Non-Hydrostatic Mesoscale Atmospheric Simulation System (NHMASS) model version 6.3 (Kaplan et al. 2000), adapted for modeling of stratospheric dynamics, is used for this study. TKE PBL physics (Therry and Lacarrerre 1983), mixed-phase moisture physics (Lin et al. 1983; Rutledge and Hobbs 1983), and the Kain-Fritsch cumulus parameterization scheme (Kain and Fritsch 1993) were used in all simulations performed. A nested-grid approach was used, with the initial grid featuring 18-km grid spacing and each subsequent nest finer in scale by a factor of three. The finest-scale horizontal grid spacing used was 222 m, which will be utilized in evaluating stratospheric wave breaking and generation of turbulence. A summary of simulations performed is found in Table A1. See Figure A1 for a schematic of grid meshes discussed in this paper.

3. ANALYSIS OF FLOW IMBALANCE AND IGW GENERATION

To understand the unbalanced flow inertia-gravity wave energy source, one needs to first consider the flow characteristics of a balanced jet streak, depicted in a schematic given in Figure 2. One notes an ageostrophic component directed toward lower streamfunction (akin to geopotential height on an isobaric surface) in the entrance region of the jet streak, and a component directed toward higher streamfunction in the exit region. The direction of these ageostrophic components is consistent with acceleration (deceleration) of the total wind in the entrance (exit) region of the geostrophic wind maximum, and represents an attempt by the atmosphere to maintain mass-momentum (i.e., thermal wind) balance. Any deviation from this simple conceptual model, which could disrupt thermal wind balance, will be considered *unbalanced flow*, a classification of great importance since such flow is known to generate unbalanced mesoscale circulations, such as inertia-gravity waves.

Table A1. Summary of MASS Simulations Performed

Initialized (UTC)	Resolution (km)	Grid Dimensions (x,y,z)	Duration (Hours)	Modifications	Hydrostatic / Non- Hydrostatic	Simulation Name
02/14/03 1200	36	95,114, 90	72	None	H	FULL36
02/14/03 1200	36	95,114, 90	72	Dry *	H	DRY36
02/15/03 1200	18	162,162,90	60	None	NH	FULL18
02/15/03 1200	18	162,162,90	60	Smooth Terrain	NH	SMOOTH18
02/16/03 1800	6	153,100,90	18	None	NH	FULL6
02/16/03 1800	6	153,100,90	18	Smooth Terrain	NH	SMOOTH6
02/16/03 1800	6	153,100,90	18	Dry	NH	DRY6
02/16/03 1830	2	200,125,90	9	None	NH	FULL2
02/16/03 1830	2	200,125,90	9	Smooth Terrain	NH	SMOOTH2
02/17/03 0100	0.670	127,127,90	2	None	NH	FULL670
02/17/03 0100	0.670	127,127,90	2	Smooth Terrain	NH	SMOOTH670
02/17/03 0100	0.222	162,162,90	0.75	None	NH	FULL222

* DRY runs differ from FULL simulations in that diabatic heat release due to evaporation and condensation has been omitted. Sensible heating remains intact in all simulations.

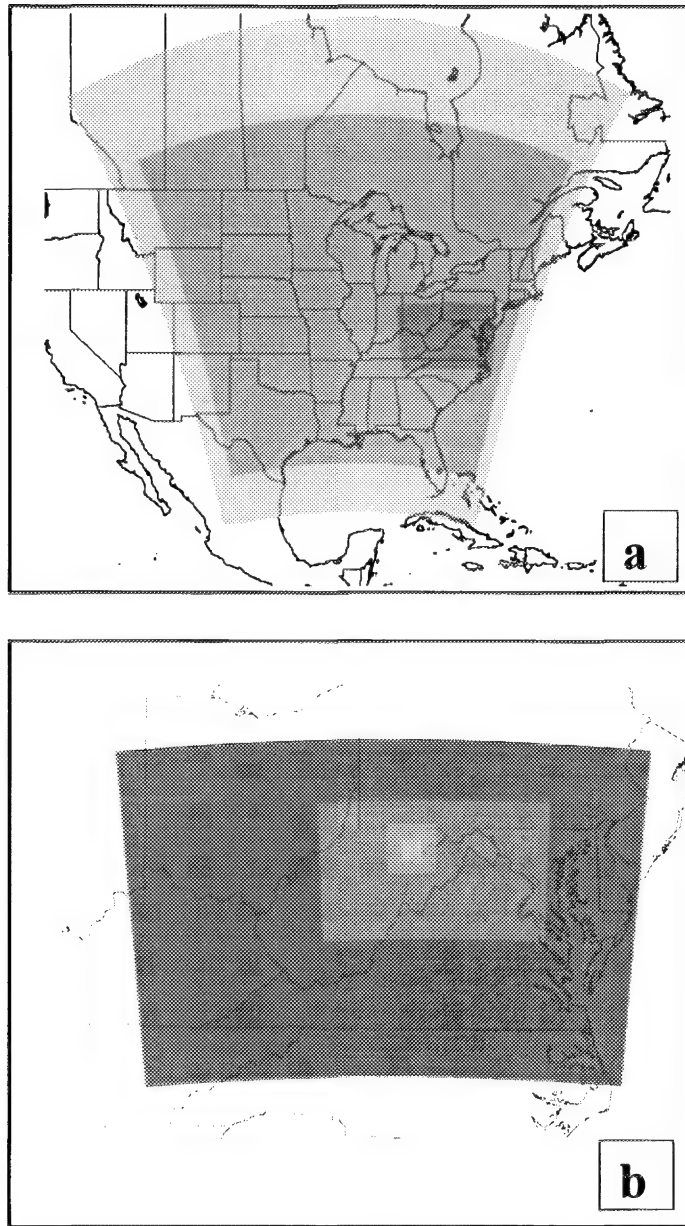


Figure A1. (a) 36-km Domain (light shading), 18-km and 6-km grid meshes (medium and dark shading, respectively), and (b) 6-km Domain (darkest shading), 2-km, 670-m, and 222-m grid meshes (lightest shading).

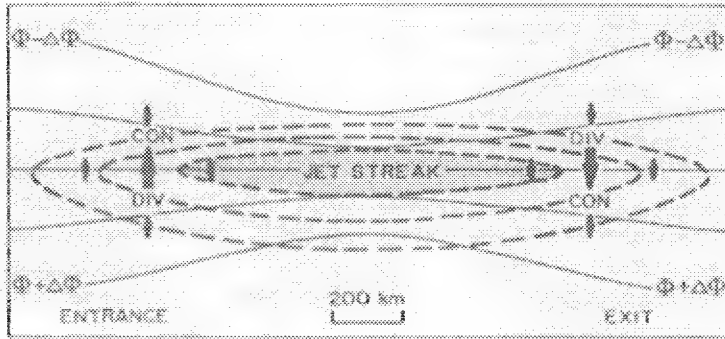


Figure A2. Schematic representation of the ageostrophic motions (heavy arrows) and associated patterns of convergence (CON) and divergence (DIV) in the vicinity of a straight jet streak in the absence of along-contour thermal advection. Assumed to be near level of maximum wind, where the horizontal wind distribution is most distinct and the flow is approximately horizontal. Solid lines indicate geopotential height of a constant pressure surface; dashed lines are isotachs with maximum wind speed shaded. [From Keyser and Shapiro (1981) and Keyser and Shapiro (1986)].

Figure A3 is a 300-hPa analysis of U.S. rawinsonde data valid 1200 UTC, 16 Feb 2003, and indicates a component of the total wind directed toward lower streamfunction in the exit region of the (*geostrophic*) STJ streak (indicated by the oval in Figure A3). This is clearly inconsistent with the balanced jet schematic in Figure A1. Evidence of unbalanced flow within the NHMASS simulations performed is given in Figure A4, an analysis of the Lagrangian Rossby number (Ro_L) within the 36-km full physics NHMASS simulation (FULL36) at (a) 16/1200, (b) 16/1800, and (c) 17/0000, where

$$Ro_L = |DV/dt| / |fV|. \quad (A1)$$

Caution, though, must be exercised in the use of Ro_L in assessing imbalance in highly curved flow such as that seen in Figure A3, as Ro_L includes the effects of curved flow, which itself can be described through gradient wind balance. For this reason, precise magnitudes of Ro_L should not be gleaned from Figure A4; only an evaluation of regions of likely flow imbalance should be made. Large values of $Ro_L (> 0.5)$ have been shown to exist for flows that cannot be described by either geostrophic or gradient wind balances, i.e., unbalanced flow (Uccellini and Koch 1987; Koch and Dorian 1988; Rozumalski 1998 among others), and will be utilized here to confirm the unbalanced flow signal in the simulation. One notes that the region of high Ro ($\sim 0.7\text{--}0.8$) at 16/1200 [Figure A4(a)] over much of Kentucky and southern Indiana is part of the same region inferred as unbalanced in the 300-hPa upper-air analysis (Figure A3). By 17/0000 [Figure A4(c)], the region of large Ro has expanded and moved to the northeast, with the largest Ro (> 0.8) over northern West Virginia. The movement of this region of apparently unbalanced flow is consistent with the motion of the STJ exit region in both the upper-air analysis and simulated 300-hPa fields (not shown).

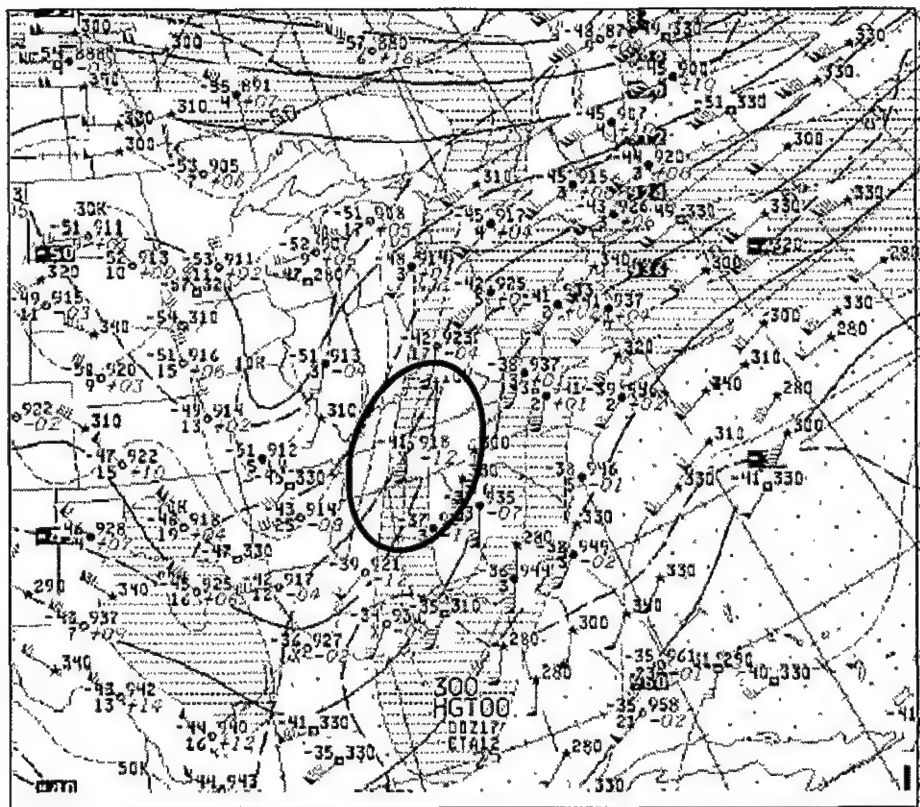


Figure A3. 300-hPa NMC analysis valid 0000 UTC, 2/17/03. Oval denotes region described in text.

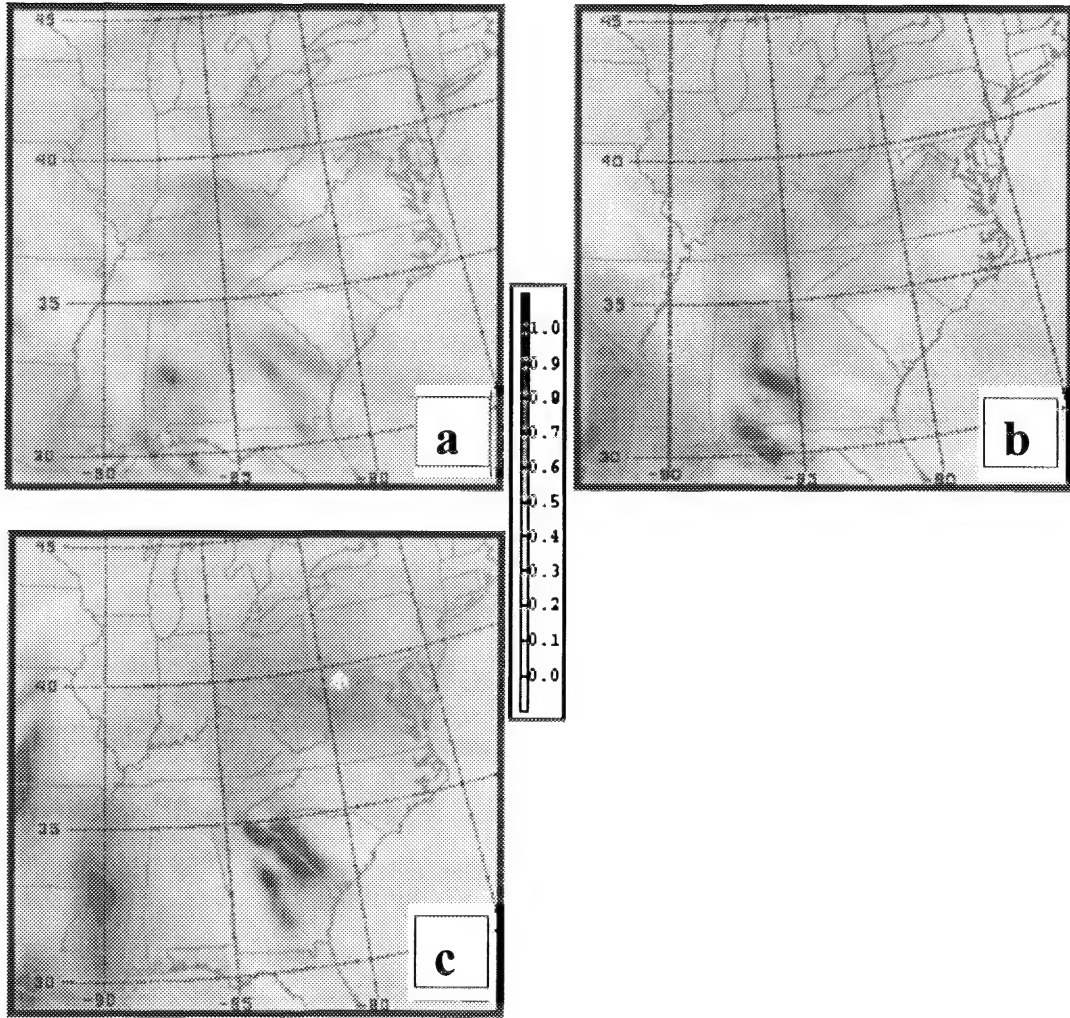


Figure A4. FULL36 332 K Lagrangian Rossby valid (a) 16/1200, (b) 16/1800, and (c) 17/0000. The star in (c) marks location of western Maryland.

With the presence of unbalanced flow in the STJ exit region now established in both the observational and NHMASS datasets, an assessment of IGW activity will be made. In Figure A5, which depicts an NOAA Global Positioning System (GPS) surface pressure trace from the Louisville, Kentucky (LOU) GPS site, one notices a roughly one-hPa wave of elevation near 16/2100 followed one hour later by a wave of depression of opposite amplitude. This pair of high-frequency waves is embedded within a much longer period (~48hr) oscillation associated with the passage of surface low pressure. Reasonably consistent with this feature in the GPS pressure trace is a wave of depression noted within the FULL18 surface pressure tendency fields at 16/2000 from central Kentucky to upstate South Carolina [Figure A6(a)]. It should be noted that estimations of horizontal wavelength and vertical wavelengths of 94 km (Figure A7) and 4 km (not

shown), respectively, from higher resolution NHMASS output of potential temperature and vertical velocity are consistent with previous studies of inertia-gravity wave activity (Uccellini and Koch 1987). The wave of depression at 16/2000 in Figure A6(a) is noted to have moved to the Kentucky/West Virginia border by 16/2200 [Figure A6(b)], along with a band of precipitation out of phase with the wave (not shown). This out-of-phase relationship is noted to be one piece of evidence supporting the assessment of the wave activity as IGW activity (Koch and Dorian 1988).

A second test for IGW activity, quadrature between mid-tropospheric vertical velocity (w) and potential temperature (θ) fields, is evident in Figure A8, a timeseries of 400-hPa w and θ fields at a point in northern West Virginia from the FULL222 simulation.

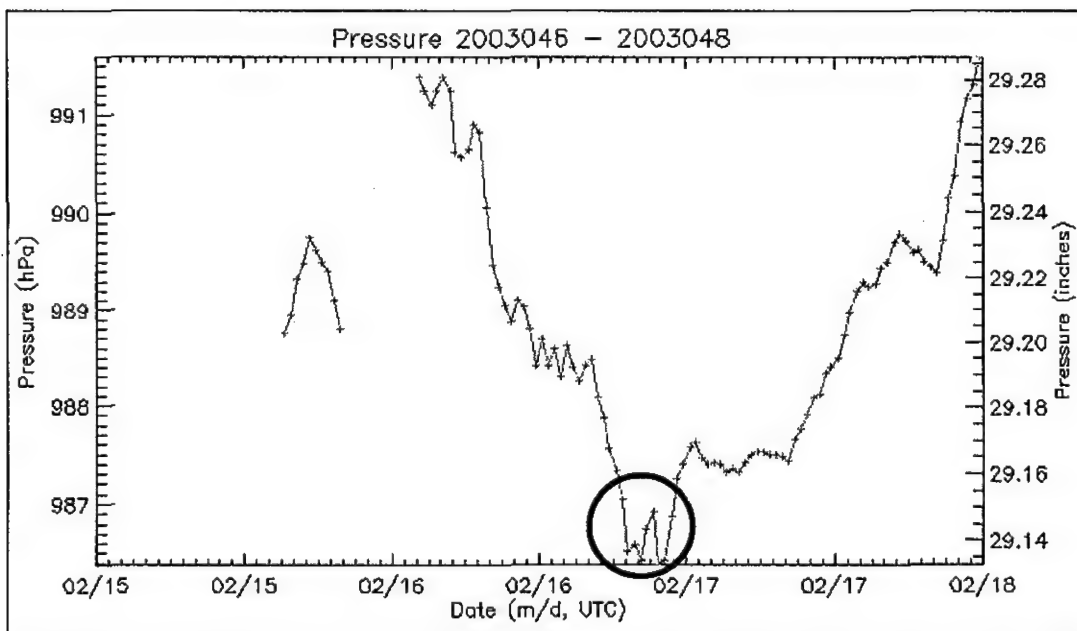


Figure A5. NOAA Global Positioning System (GPS) surface pressure trace from Louisville KY (LOU) GPS site. Valid 0000 UTC, 2/15/03 to 0000 UTC, 2/18/03. Period of IGW activity between 2000 UTC, 2/16/03 and 2300 UTC, 2/16/03 noted with black circle.

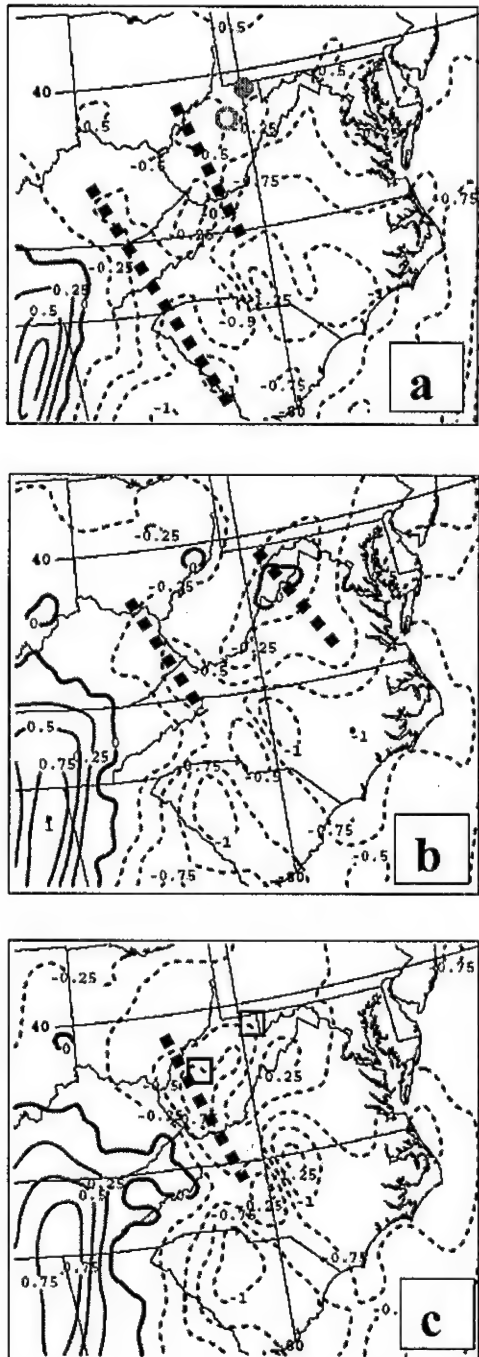


Figure A6. NHMASS FULL18 (a)-(b)-(c) one-hour sea-level pressure tendency (hPa/hr) for 2000 UTC, 2/16/03, 2100 UTC, 2/16/03, and 2200 UTC, 2/16/03, respectively. Boxes in (c) denote areas over which covariances of perturbation pressure and front normal surface wind were calculated (see text for details). Hollow circle in (a) is point A for timeseries in Figure A8; filled circle for profiles in Figure A9.

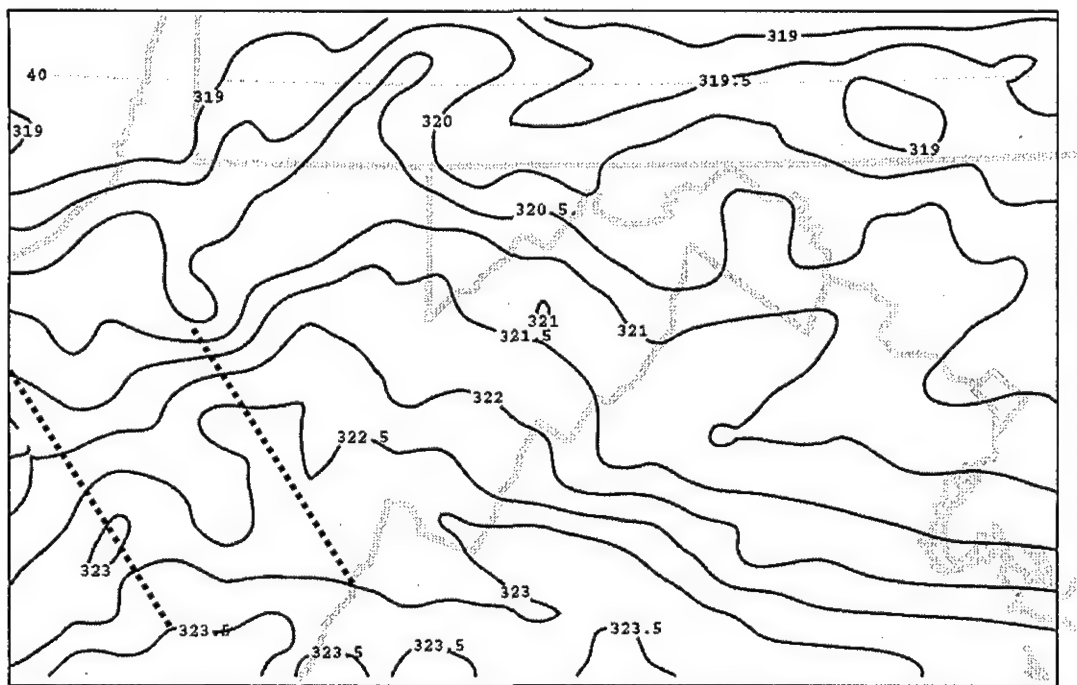


Figure A7. 2-km NHMASS 400-hPa potential temperature, valid 0200 UTC, 2/17/03.
Select waves noted by dashed black lines.

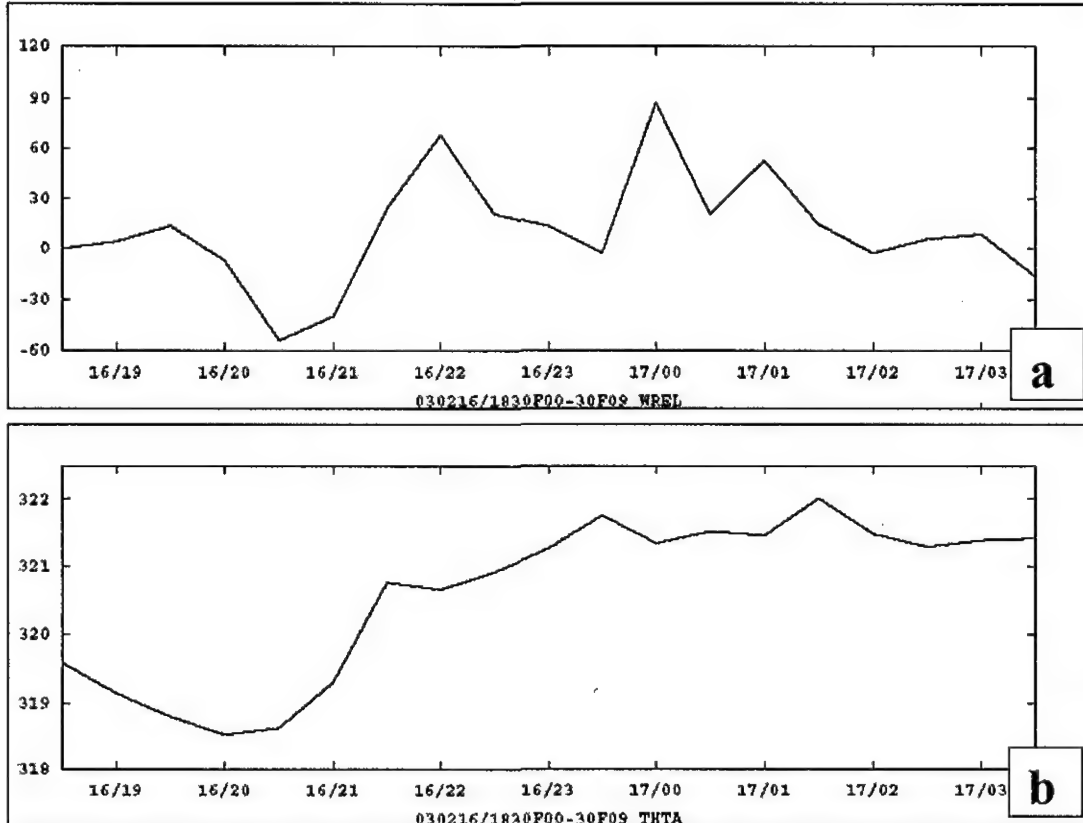


Figure A8. NHMASS FULL2 time series of (a) 400-hPa vertical velocity [cm/s] and (b) 400-hPa potential temperature [K] from 1830 UTC, 2/16/03 to 0330 UTC, 2/17/03 for point A displayed in Figure A6(a).

While no filtering has been performed on the analysis, resulting in the use of θ rather than θ' and w rather than w' , quadrature between 400-hPa w and θ is clearly evident, lending credibility to the assertion of the wave activity as IGW activity. An analysis of the phase relationship between surface pressure and wave-normal horizontal wind speed was performed (correlations approaching 0.8) and, in combination with the previous tests discussed, supports the claim of inertia-gravity waves as the source of the mesoscale banding noted in the available datasets. Due to the limited nature of asynoptic data in the region of wave propagation and lack of filtering performed in the above analyses, no definitive claims can be made. As a result, the wave activity will be referred to as *apparent* IGW activity within this paper.

4. TRANSITION OF IGWs TO TURBULENCE

In this section, the process through which vertically propagating apparent IGW waves underwent steepening, and consequently led to development of instability and generation of turbulence will be considered. It is well known that wave breaking is often noted in regions of the atmosphere characterized by a critical layer (where wave phase speed is equal in magnitude to the mean flow in the direction of wave propagation), low Richardson number, and a wind reversal layer (Jiang and Doyle 2004). Near the critical level, the vertical wavelength of the waves approach zero and the group velocity is directed entirely in the horizontal, i.e., vertical propagation of wave energy becomes zero at the critical level (Lin TBD). The orientation of gravity waves entirely in the horizontal produces fine-scale instabilities that promote wave breaking and breakdown of the mesoscale waves into turbulence.

Considering the common atmospheric structure in the vicinity of wave-breaking regions, vertical profiles of wave-front normal wind speed and Richardson number from FULL222 simulations will be considered. Figure A9(a), a profile of wave-front normal wind speed as determined from wave-front positions noted in Figure A6, indicates a deep layer of negative wind shear above approximately 180 hPa with multiple layers of enhanced wind shear. Figure A9(b) indicates that a low Richardson number (less than 5) is simulated between about 120 hPa and 80 hPa, within the layer of negative wind shear. Although Richardson numbers less than unity have been observed in analyzing critical layers (Jiang and Doyle 2004; Koch and Dorian 1988), the layer of interest in this case is in the very stable lower stratosphere (large $d\theta/dz$), where the Ri calculation is likely skewed larger by the strong static stability, despite the presence of large values of vertical wind shear.

A potential range of critical levels has been included in Figure A9(a), determined from both calculations of phase speed from linear theory and a subjective analysis of timeseries of 70-hPa velocity divergence fields from the FULL222 simulation (not shown). Evident in a comparison of Figures A9(a) and A9(b) is the fact that the range of possible critical levels is not collocated with the layer of the low Richardson number. A critical limitation of this analysis is that a total wind speed ($U+u'$) profile has been utilized, rather than a profile of background wind speed (U). It has been noted by Fritts (1984) that a critical level may be induced, due to non-linear effects where $U+/-u'=c$. While this raises significant questions as to the actual location of a critical level (or levels), the likelihood of turbulence indicated by NHMASS simulations (to be discussed) and the presence of vertically propagating wave activity supports the presence of a critical level (or levels) within the lower stratosphere.

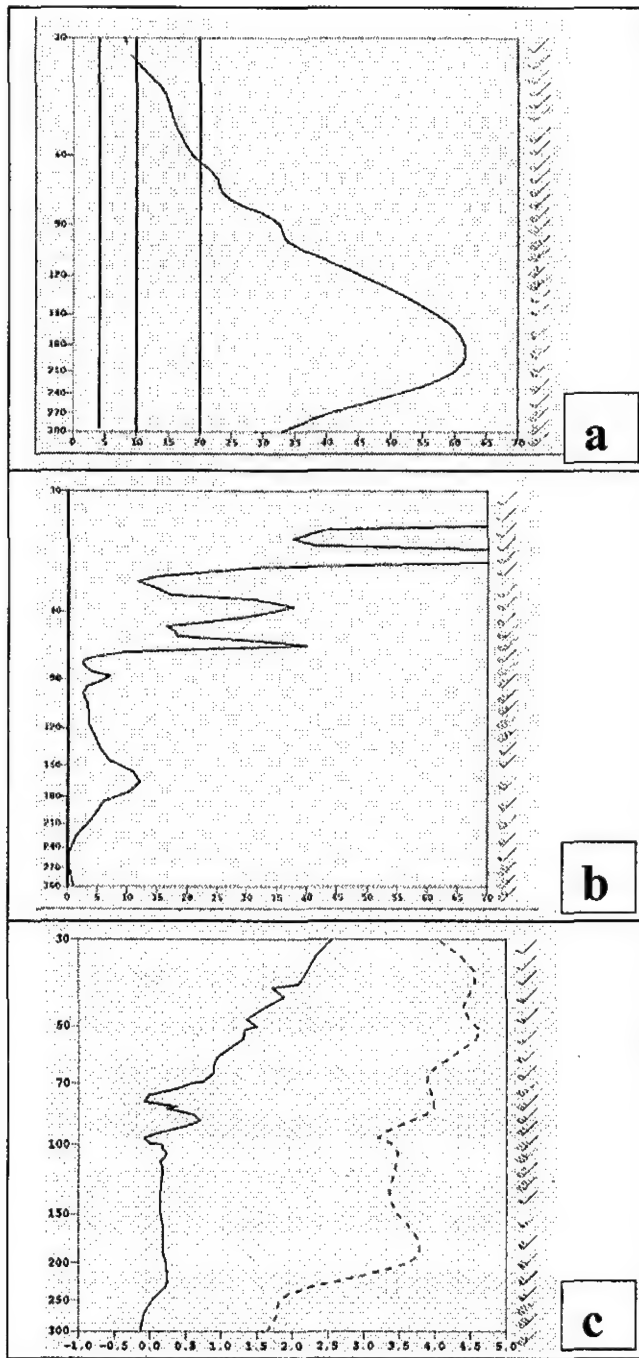


Figure A9. 0154 UTC, 2/17/03 222-m NHMASS profiles of (a) wave-front normal wind speed and vectors (m/s). Range of critical level wind speeds (5-20 m/s) noted (see text), (b) Richardson number, vertical profile of wave front normal wind (m/s) included, and (c) Scorer parameter (solid profile, scaled by 10^6) and turbulence kinetic energy dissipation (dashed profile, scaled by 10^7), defined in text. See Figure A6 for location of profile.

The vertical variation of Scorer parameter (l^2), where

$$l^2 = \frac{N^2}{U^2} - \frac{U_{zz}}{U}, \quad (\text{A2})$$

may be used as a measure of the potential for critical level wave reflecting, as both the Richardson number (Ri) and wind reversal requirements discussed above are accounted for here (Chun 1991). This is true since Ri is proportional to static stability, which can be represented by N^2 , the Brunt Vaisala frequency, and the wind reversal layer is indicated by the curvature of u , or U_{zz} . It can be shown from linear wave theory that for $l^2 < 0$, an evanescent flow regime exists wherein vertical propagation of wave energy is zero and for $l^2 > 0$, a regime exists where waves are free to propagate vertically (Lin TBD).

Therefore, one can view layers where $[\partial(l^2)/\partial z < 0]$ as layers where wave modes transition from vertically propagating to modes where the vertical wavelength equals zero. Such a transition occurs as waves approach a critical level, and as such one should expect wave steepening and potential breaking/turbulence generation in regions where $[\partial(l^2)/\partial z < 0]$. Thus, from the Scorer parameter profile in Figure A9(c), the layers near 100 hPa, 85 hPa, 50 hPa, and 40 hPa will be considered for wave breaking and potential turbulence generation.

Steepening wave activity can be seen in a cross-sectional analysis of vertical velocity from the FULL222 simulation at 17/0154 (Figure A10). It is clear that the vertical wavelength of the waves are decreasing with increasing height in the lower stratosphere, consistent with the presence of a critical level (or levels). One can see that the strongest wave is located near 150 hPa in the center of the cross-sectional axis with an amplitude of greater than -0.9 m/s, a vertical velocity respectable for such a height in the atmosphere. As the waves steepen and largely become oriented in the horizontal, one expects the vertical variation of potential temperature (θ) and horizontal wind speed (U) to increase as the alternating phases of θ and U in the horizontal are tilted into the vertical. These changes are consistent with the generation of mesoscale instabilities, two of which, convective instability and Kelvin-Helmholtz (or shearing) instability, will be discussed next.

Convective instability, present where $\partial\theta/\partial z < 0$ (or $\partial\theta/\partial z < 0$ for very dry flow in the lower stratosphere), is clearly not resolved at the 222-m scale, as indicated by the lack of overturning of the isentropes in Figure A11. One notes $\partial\theta/\partial z > 0$ everywhere within the lower stratosphere. Presumably, with finer horizontal and vertical grid resolution, as well as stronger critical levels (i.e., more wave amplification), overturning of the isentropes in the lower stratosphere would be explicitly resolved. A second instability, Kelvin-Helmholtz instability, produces growing disturbances through extraction of kinetic energy present in strongly sheared flow ($|\partial U/\partial z| \gg 0$) for use in raising or suppressing stable fluid ($N^2 > 0$). This instability is most effective for strong shear and weak static stability (i.e., $Ri < 1/4$) (Lin TBD).

While multiple layers of enhanced vertical wind shear are apparent in a lower-stratospheric cross-section of total wind speed (Figure A11), the lack of layers with both strong enough shear and sufficiently weak static stability precludes Kelvin-Helmholtz instabilities from developing in the FULL222 simulation. It must be emphasized here that the convective and orographic forcing supporting the wave breaking layers was weak during this case, increasing the difficulty of simulating full wave breaking. NHMASS simulations by another NHMASS modeler (Paul Suffern) of a separate case study of inertia-gravity wave breaking in a region of stronger convective forcing with 222-m grid spacing have explicitly resolved the above instabilities and through use of a 71-m resolution simulation, turbulent mixing, indicating the mesoscale model's ability to resolve such features. Lane et al. (2003), in a numerical modeling study of turbulence above deep convection, was able to resolve regions of turbulence with a 3-dimensional cloud model with grid spacing approximately $\frac{1}{4}$ that used in the finest of the simulations in this study. The smallest resolvable feature in this simulation, on the order of 888 m ($4\Delta x$ wave), is much larger than the scale of most turbulent eddies (~100- to 300-m).

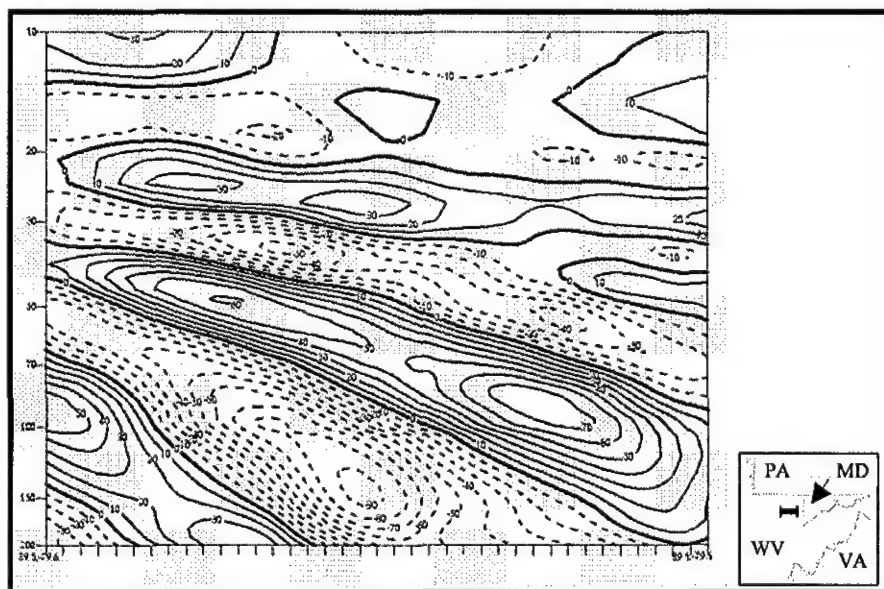


Figure A10. 222-m NHMASS vertical cross-section of vertical velocity (cm/s), solid (positive), dashed (negative), valid 0154 UTC, 2/17/03. See inset for cross-section axis.

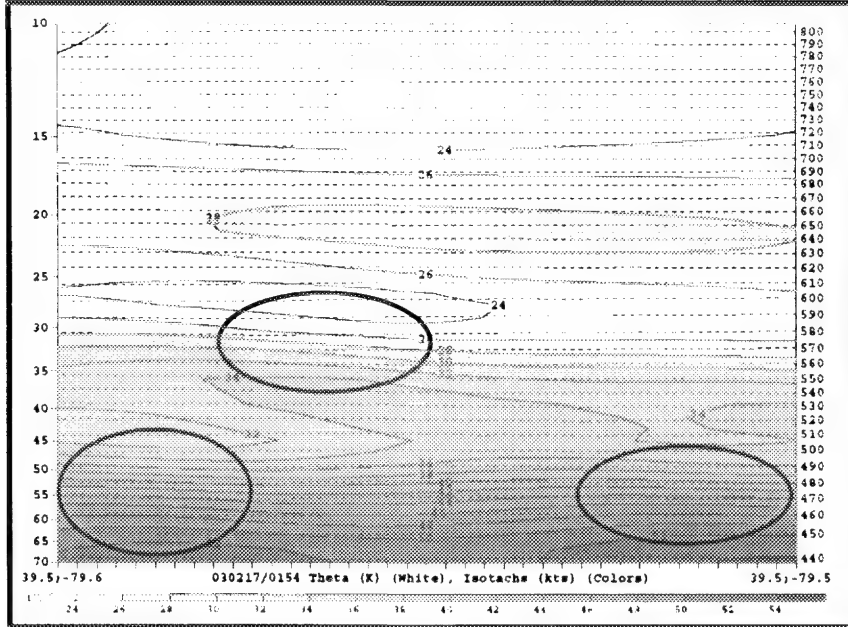


Figure A11. 222-m NHMASS vertical cross-section of total wind speed (m/s) (shaded, solid contour) and potential temperature (K) (dashed), valid 17/0154. Regions of potential Kelvin-Helmholtz instability indicated by ovals. For cross-section axis see inset in Figure A10.

Caution must be exercised in interpreting mesoscale model output at such fine horizontal resolutions (such as 71 m), as the unequal vertical and horizontal resolutions negates the proper simulation of large turbulent eddies. Additionally, due to the need for increased vertical resolution both in the boundary layer and in the lower stratosphere, a discontinuity in vertical resolution exists in the lower stratosphere near 110 hPa. This discontinuity, on the order of a change of vertical resolution of ~ 500 m/10 hPa, raises doubt as to the degree of simulated wave-breaking, as some wave reflection in the NHMASS simulations near 110 hPa may be numerical in origin. The use of finer scale simulations in this study was prevented by extreme near-surface instabilities generated due to errors in the boundary layer scheme in the vicinity of fine-scale terrain.

Despite the insufficient resolution with which to explicitly resolve the above instabilities (and therefore turbulent mixing), the resolved fields within the FULL222 simulation do indicate the likelihood of sub-grid scale turbulence. The first large-scale measure of turbulence to be considered, the NCSU1 index, defined as

$$NCSU1 = \left[\bar{U} \bullet \nabla \bar{U} \right] \frac{|\nabla \zeta|}{|Ri|}, \quad (A3)$$

has been shown to be sensitive to regions of strong anticyclonic shear in the presence of low Ri (conditions conducive for clear-air turbulence [CAT]) (Kaplan et al. 2004). Inertia-gravity wave activity perturbs the large-scale flow, producing the regions of strong lateral shear and weak dynamic stability that the NCSU1 parameter is designed to be sensitive to. Figure A12 indicates a region of enhanced NCSU1 values moving northeast toward the location of the aforementioned vertical profiles and cross-sections that were suggestive of wave breaking. Of interest is the fact that the region of high NCSU1 index values, apparently maximized at 17/0154 [Figure A12(d)] is positioned immediately west of a roughly 150-m steep terrain ridge across northeastern West Virginia (Figure A13). One possibility is that mountain-wave drag due to low-level easterly flow normal to the ridge induces a critical level (or levels) in the lower stratosphere (Lin TBD). The apparent inertia-gravity waves, propagating toward northeastern West Virginia, encounter these mountain-wave induced critical levels, steepen, and break-down into turbulence.

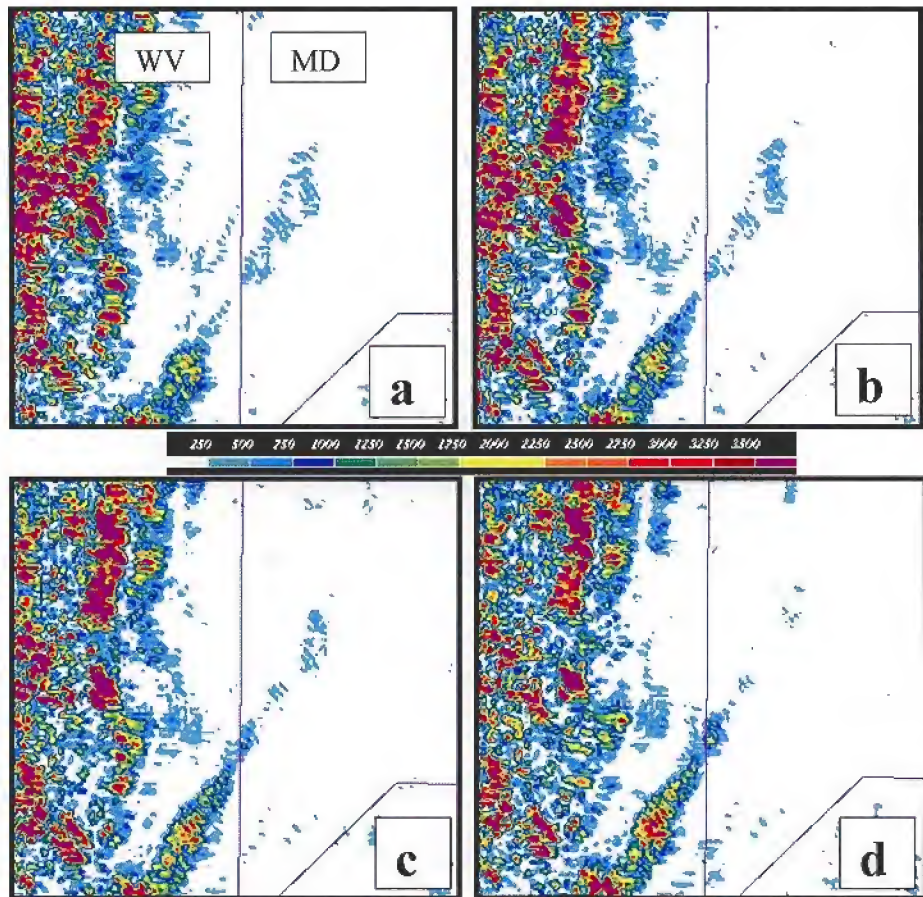


Figure A12. 222-m NHMASS NCSU1 index [scaled by 10^{13}] valid (a) 0145 UTC, 2/17/03, (b) 0148 UTC, 2/17/03, (c) 0151 UTC, 2/17/03, and (d) 0154 UTC, 2/17/03. See text for definition of NCSU1 index.

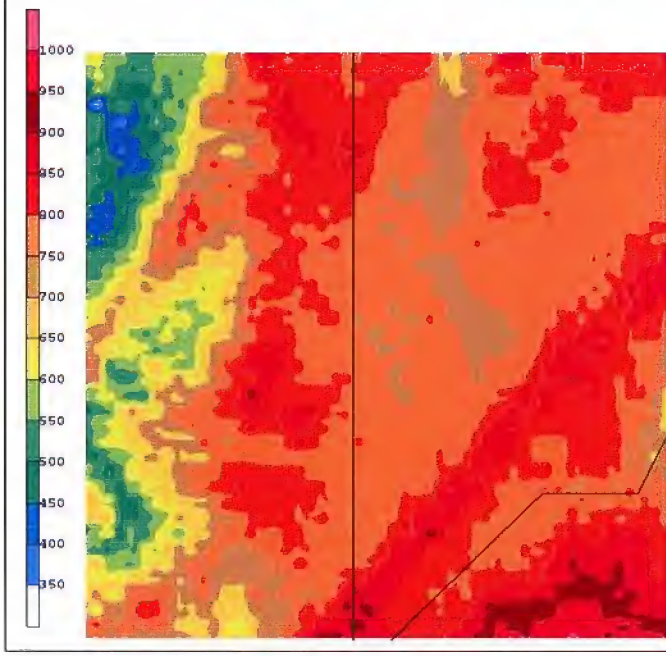


Figure A13. 222-m NHMASS model terrain [m].

The mean turbulence kinetic energy (TKE), defined as

$$\frac{TKE}{m} \equiv \frac{1}{2} \left(\overline{u'^2} + \overline{v'^2} + \overline{w'^2} \right) \equiv \bar{e} \quad (A4)$$

(Stull 1988), is the most direct measure of turbulence available. A turbulence budget equation can be written for mean turbulence kinetic energy,

$$\frac{\partial \bar{e}}{\partial t} = -\bar{u'}\bar{w'} \frac{\partial \bar{u}}{\partial z} - \bar{v'}\bar{w'} \frac{\partial \bar{v}}{\partial z} + \frac{g}{T_o} (\bar{w'}\theta') - \frac{\partial}{\partial z} \left(\bar{e'}\bar{w'} + \frac{l}{\rho_o} \bar{p'}\bar{w'} \right) - \varepsilon \quad , \quad (A5)$$

I	II	III	IV	V	VI
---	----	-----	----	---	----

assuming horizontal homogeneity (Stull 1988). In Equation (A5), term I is the TKE tendency, term II and III are shear production/loss terms, term IV is the buoyant production/dissipation term, term V represents vertical diffusion, and term VI represents the viscous dissipation of TKE. The boundary layer parameterization used for all NHMASS simulations in this study is based on the 1.5 order TKE closure scheme developed by Therry and Lacarrerre (1983), wherein a form of the TKE budget Equation (A5) is used in closing the model equations. Post-processing of NHMASS output makes use of the TKE scheme in generating TKE profiles, yet due to the apparently weak nature of the turbulence in the lower stratosphere, the output of raw TKE proved to be of little value as small quantities of TKE are output as zero. Rather, TKE dissipation (term VI in

Equation (A5)) calculations were relied upon in this study and are generated using the empirical relationship,

$$\varepsilon \approx \frac{0.125(TKE)^{3/2}}{LE}, \quad (\text{A6})$$

where LE is the dissipation length (Kaplan et al. 2000). While a more rigorous analysis would involve calculating terms I-V in Equation (A5) and estimating ε as a remainder, this empirical method does appear to have some value.

Considering a profile of ε [dashed profile in Figure A9(c)], one notes a good correlation between the layers of possible critical level-induced wave breaking (I^2 decreasing with height) and the layers of enhanced ε . One also notices that the greatest values of ε are not associated with the more pronounced layers of $\partial/\partial z(I^2) < 0$ in the 80-100-hPa layer but, rather, are maximized near the 50-hPa level where gradients of I^2 are smaller. One possibility for this vertical ε structure is that with each successive critical level encountered by vertically propagating waves, each level is not strong enough to limit further vertical movement of wave energy, and so multiple wave-breaking episodes occur with the ~50-hPa level receiving the benefits of the subsequent turbulence generation. Nevertheless, the two vertical profiles [Figure A9(c)] and the NCSU1 analysis (Figure A12) appear to support the idea that (1) vertical variation in Scorer parameter can indicate possible wave-breaking layers and (2) the variations in the mesoscale horizontal fields represented by the enhanced values of the NCSU1 index at 50 hPa were a reasonable indicator of 50-hPa turbulence potential across northeastern West Virginia.

5. SUMMARY AND CONCLUSIONS

The threat of atmospheric turbulence to the aviation community motivated this study of inertia-gravity wave breaking and generation of lower-stratospheric turbulence during the 2003 Presidents' Day winter storm. The ability of a mesoscale model, the Non-hydrostatic Mesoscale Atmospheric Simulation System (NHMASS) version 6.3, to simulate the development of apparent inertia-gravity wave activity in the mid-troposphere and subsequent transition to turbulence in the lower stratosphere has been evaluated. Simulation of both the pre-existing unbalanced mid-tropospheric flow and the resultant apparent inertia-gravity wave activity have been shown to be consistent with the synoptic and limited asynoptic data available. The vertically propagating wave activity was noted to propagate toward northeastern West Virginia, losing coherency north and east of the region (not shown). The Scorer parameter, a measure of both vertical decrease of static stability and the presence of negative vertical wind shear (both consistent with critical layer theory), was evaluated over northeastern West Virginia. This analysis of the vertical structure of the upper troposphere and lower stratosphere revealed a number of potential levels where vertical propagation of wave energy was limited and the likelihood of wave breaking increased.

Cross-sections of vertical velocity indicated vertically propagating wave activity in the upper troposphere, with vertical wavelengths decreasing with height in the lower stratosphere, consistent with the presence of a critical level (or levels) in that layer. Two

mesoscale instabilities noted to develop in regions of breaking inertia-gravity wave activity, convective instability and Kelvin-Helmholtz (or shearing) instability (Lane et al 2003), were not resolved with 222-m horizontal resolution, yet the existence of sub-grid scale turbulence was inferred from two turbulence indicators, the NCSU1 index and turbulence kinetic energy (TKE) dissipation. The NCSU1 index, sensitive to horizontal gradients of momentum and small values of the Richardson number, was evaluated at 50 hPa (one of the layers indicated by Scorer parameter profiles as a possible wave-breaking layer), revealed the likelihood of turbulence in northeastern West Virginia. Bands of high NCSU1 index were noted to have been positioned along, and in the lee of, 100- to 300-m tall terrain ridges in the region, where mountain wave activity potentially induced the critical levels deduced in the aforementioned vertical profiles. A comparison of vertical profiles of TKE dissipation and Scorer parameter indicated a high correlation between the potential wave-breaking layers indicated by the vertical variation of Scorer parameter and the regions of enhanced TKE dissipation.

This study indicates the suitability of two parameters in detecting the potential for wave breaking and lower-stratospheric turbulence utilizing simulations with insufficient resolution with which to explicitly resolve either full wave breaking or turbulent mixing. One parameter is sensitive to lateral changes associated with the increased anticyclonic shear produced by amplifying inertia-gravity waves (NCSU1), and the second is sensitive to vertical variation of the perturbed flow suggestive of wave-breaking potential (Scorer parameter). Improving the predictability of turbulence is an effort sure to have many positive effects on the aviation community and the public-at-large.

6. FUTURE WORK

Additional case studies are currently being analyzed, applying the same methodology described here, in order to further test the predictability of turbulence in the lower stratosphere using the NCSU1 index and vertical variation of Scorer parameter. Lastly, the possibility of utilizing high temporal and spatial resolution NOAA-16 Advanced Microwave Sounding Unit (AMSU) brightness temperature data to better validate the existence of inertia-gravity wave activity in NHMASS simulations is being pursued.

REFERENCES

- Cetola, J. D., 2003: The role of terrain and convection on microfront formation leading to severe low-level turbulence. Ph.D. dissertation, North Carolina State University, 323 pp.
- Chun, H.-Y., 1991: Role of a critical level in a shear flow with diabatic forcing. MS thesis, North Carolina State University, 159 pp.
- Cowen, R., 1998: Clearing the air about turbulence. *Weatherwise*, **51**, 24-28.
- Fritts, D. C., 1978: The nonlinear gravity wave-critical level interaction. *J. Atmos. Sci.*, **35**, 397-413.
- Jiang, Q., and J. D. Doyle, 2004: Gravity wave breaking over the central Alps: Role of complex terrain. *J. Atmos. Sci.*, **61**, 2249-2266.
- Kain, J. S., and J. M. Fritsch, 1993: Convective parameterization for mesoscale models: The Kain-Fritsch Scheme. *The Representation of Cumulus Convection in Numerical Models, Meteor. Monogr.*, No. 46, Amer. Meteor. Soc., 165-170.
- Kaplan, M. L., Y.-L. Lin, J. J. Charney, K. D. Pfeiffer, D. B. Ensley, R. P. Weglarz, and D. S. DeCroix, 2000: A Terminal Area PBL Prediction System at Dallas-Fort Worth and its application in simulating diurnal PBL jets. *Bull. Amer. Meteor. Soc.*, **81**, 2179-2204.
- Kaplan, M. L., K. M. Lux, J. D. Cetola, A. W. Huffman, A. J. Riordan, S. W. Slusser, and Y.-L. Lin, 2004: Characterizing the severe turbulence environments associated with commercial aviation accidents. A real-time turbulence model (RTTM) designed for the operational prediction of hazardous aviation turbulence environments. NASA/CR-2004-213025, 49 pp.
- Koch, S. E., and R. E. Golus, 1988: A mesoscale gravity wave event observed during CCOPE. Part I: Multiscale statistical analysis of wave characteristics. *Mon. Wea. Rev.*, **116**, 2527-2544.
- Koch, S. E., and P. B. Dorian, 1988: A mesoscale gravity wave event observed during CCOPE. Part III: Wave environment and probable source mechanisms. *Mon. Wea. Rev.*, **116**, 2570-2592.
- Lane, T. P., R. D. Sharman, T. L. Clark, and H.-M. Hsu, 2003: An investigation of turbulence generation mechanisms above deep convection. *J. Atmos. Sci.*, **60**, 1297-1321.

- Lin, Y.-L., R. D. Farley, and H. D. Orville, 1983: Bulk parametrization of the snow field in a cloud model. *J. Climate and Appl. Meteor.*, **22**, 1065-1092.
- Lin, Y.-L., TBD.: *Mesoscale Dynamics*. Cambridge University Press, (in progress).
- Rozumalski, R. A., 1997: The role of jet streak regeneration forced by a deepening continental planetary boundary layer in the explosive surface cyclogenesis of 28 March 1984. Ph.D. dissertation, North Carolina State University, 360 pp.
- Rutledge, S. A., and P. V. Hobbs, 1983: The mesoscale and microscale structure and organization of clouds and precipitation in midlatitude cyclones. VIII: A model for the “seederfeeder” process in warm-frontal rainbands. *J. Atmos. Sci.*, **40**, 1185-1206.
- Stull, R. B., 1988: *An Introduction to Boundary Layer Meteorology*. Kluwer Academic Pub., 670 pp.
- Therry, G., and P. Lacarrere, 1983: Improving the eddy kinetic energy model for the planetary boundary layer. *Bound.-Layer Meteor.*, **25**, 63-88.Uccellini, L. W., and S. E. Koch, 1987: The synoptic setting and possible source mechanisms for mesoscale gravity wave events. *Mon. Wea. Rev.*, **115**, 721-729.

Appendix B

A TKE Budget Analysis in the Upper Troposphere/Lower Stratosphere for a Vertically Propagating Gravity Wave

1. INTRODUCTION

The application of turbulent kinetic energy (TKE) and the TKE tendency equation are usually applied to quantify turbulence and turbulent tendency within the planetary boundary layer (PBL). The importance of TKE and TKE tendency is far greater within the PBL than the free atmosphere on average. However, turbulence is of great importance in the upper atmosphere, especially to aviation interests.

The United States Air Force has commissioned a project with the North Carolina State University's Mesoscale Modeling and Dynamics Lab to investigate the role of convection on generating turbulence in the lower stratosphere. Several different case studies, representing various different synoptic and mesoscale environments and different convective modes, are to be simulated using numerical models. The importance of vertically propagating gravity waves near the tropopause would have great influence on the turbulence generated in these layers. Aircraft who choose to fly over convection, especially Air Force spy planes that fly at high levels, may unexpectedly experience turbulence at vertical levels far above the convection.

A TKE budget analysis, involving the TKE tendency equation, is done explicitly for the 12 December 2002 large amplitude gravity wave over far eastern Texas and western Louisiana. Figure B1 shows the stratospheric wave for the model simulation described in this paper as a cross-section across the region. Though rudimentary, this first attempt at a TKE budget analysis is aimed at providing an initial insight and motivation for future research related to the author's thesis and the Air Force project's other case study simulations. The results presented within this paper in no way represent a truly accurate and rigorous TKE budget analysis, but provide a good qualitative starting point for future research related to TKE and eddy dissipation (EDR) budget calculations.

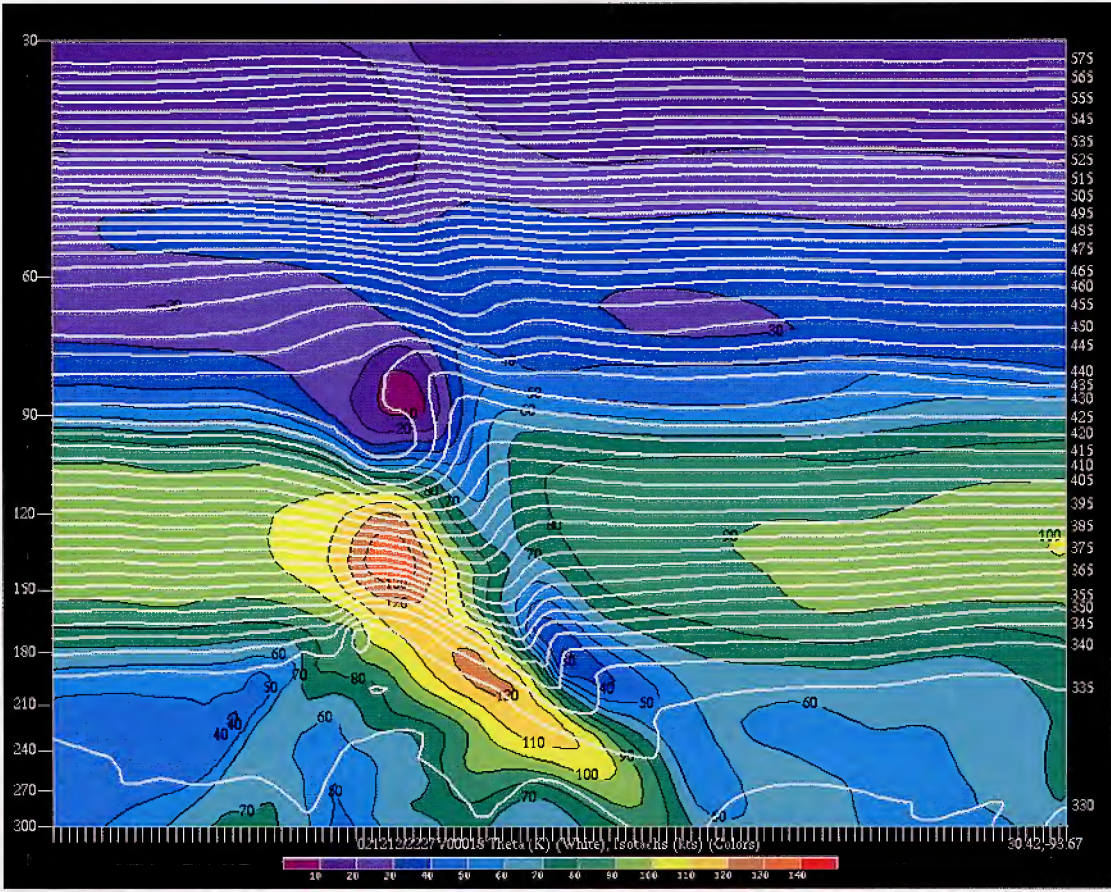


Figure B1. Cross-section showing the total wind field (color) and the isentropes (contoured) for the 222-m horizontal STRATONHMASS simulation of the 12 December 2002 large amplitude gravity wave valid at 2227 UTC, 12 December.

2. METHODOLOGY

2.1. Reynolds Decomposition

For the purposes of the TKE tendency equation, it is useful to employ Reynolds' decomposition. For any scalar quantity, its value at any time step or position can be expressed as a combination of an average/ basic state and a perturbation from that basic state, namely:

$$\Omega = \bar{\Omega} + \Omega' \quad (\text{B1})$$

For the output from a numerical model, the arbitrary value Ω would be the output at each interval specified by the user. The calculation of this arbitrary variable Ω is inherently an average itself, coming from the model's algorithm using the values at each time step. For

this study, the parameter Ω is considered to be representative of a true time step value, and not an average. The complications that arise from needing to modify the computational scheme to extract the value of Ω at each time step are beyond the current study.

If Ω is known and is treated as a set of model simulated values over a given time range, the value of the basic state/average $\bar{\Omega}$ can be calculated by simply taking a time average, such that:

$$\bar{\Omega} = \frac{(\Omega_1 + \Omega_2 + \Omega_3 + \dots + \Omega_i)}{i} \quad (B2)$$

where i is the number of output times the variable Ω is output. The user can choose different ranges to calculate the average field over. Because of time restraints, an average over the entire model run is done for the case study presented herein. If $\bar{\Omega}$ is known, then the perturbation can be calculated by solving for the perturbation value in Equation (B1):

$$\Omega' = \Omega - \bar{\Omega} \quad (B3)$$

Though this method is rudimentary, it is most convenient for the data types presented in the Air Force case studies and provide a good qualitative representation of the average and perturbation fields for any quantity from the model output. As aforementioned, the user selects the amount of time the variable Ω is averaged and, thus, selects the time scale at which the perturbations are evaluated. To capture small-scale features, it is advantageous to select a shorter time range to calculate the basic state and, henceforth, capture the smaller scale perturbations in the Ω field. If the length of the actual model run is short, and the horizontal and vertical grid spacing are small enough to capture the features of interest, this restriction can be relaxed.

2.2. TKE Tendency Equation

In order to quantify and understand the contributions to turbulence production, an analysis of each term in the TKE tendency equation is needed. Numerical models, such as the Non-Hydrostatic Stratospheric Mesoscale Atmospheric Simulation System (STRATONHMASS) output TKE at each specified output time. The TKE, defined as:

$$\bar{e} = \sqrt{u'^2 + v'^2 + w'^2} \quad (B4)$$

is calculated at each time step and averaged for each output time. The model user is unable to see variances change from each model time step. In addition, the TKE scheme does not explicitly show or calculate the various terms in the TKE tendency equation for mesoscale numerical models.

From Stull (1988), the TKE tendency equation can be written as:

$$\begin{aligned}\frac{\partial \bar{e}}{\partial t} = & -u \frac{\partial \bar{e}}{\partial x} - v \frac{\partial \bar{e}}{\partial y} - w \frac{\partial \bar{e}}{\partial z} + \frac{g}{\theta_v} \overline{(w' \theta'_v)} \\ & - \overline{(u'w')} \frac{\partial \bar{u}}{\partial z} - \frac{\partial}{\partial z} (\overline{w'e}) - \frac{1}{\rho} \frac{\partial}{\partial z} (\overline{w'p'}) - \varepsilon\end{aligned}\quad (B5)$$

Equation (B4) is valid if the model coordinate system is aligned with the mean wind, but does not necessitate the need for horizontal homogeneity as prescribed by Stull (1988, hereafter S88). The only term on the left-hand side of Equation (B5) is denoted the storage term by S88 and, for the duration of this paper, is referred to as the TKE tendency. The TKE tendency can be computed over a given time range if the variables on the right-hand side were known over the same time range.

The first term on the right-hand side of Equation (B5) is the creation/destruction of turbulence by the advection of the mean-u wind, which will be denoted *Term 1: U-Advection*. Similarly, the second and third terms are the creation/destruction of turbulence by the advection from the mean-v and mean-w wind, and are denoted *Term 2: V-Advection* and *Term 3: W-Advection*. Authors such as S88 neglect the horizontal advection by assuming the horizontal flow is homogenous, and are much smaller in comparison to Term 3: W-Advection for situations where turbulence is important. Due to the rapid fluctuations in u and v during the case study presented in Section 3, it was necessary to investigate the overall contributions from Term 1 and Term 2 to the overall TKE tendency profile. Term 3, which includes the mean vertical motion field, is hypothesized to be important in locations where large variations in TKE are overlapped with strong background vertical motion from convective motions.

The fourth term on the right-hand side of Equation (B5) is referred to as the buoyancy production/consumption term in S88, and is referred to hereafter as *Term 4: Buoyancy*. The physical interpretation of this term is that positively buoyant (negatively buoyant) parcels act to produce (consume) TKE. The product of the perturbations, which are the vertical velocity and the virtual potential temperature, mimic a vertical heat flux term. S88 states Term 4's biggest contribution within the PBL comes on days where free convection and subsequent strong surface heating takes place. For stratospheric applications, it is hypothesized that areas where perturbations in vertical motion and virtual potential temperature from convection at and below the tropopause would produce large and small variations in Term 4.

The fifth term on the right-hand side of Equation (B5) is known as the mechanical shear production term, from S88, and is referred to hereafter as *Term 5: Mechanical Shear*. According to S88, when the turbulent momentum flux is in the presence of a large mean wind shear, the two interact positively to generate more turbulence. The product of the perturbations of the u and w wind is a momentum flux, and this flux is multiplied by the basic state mean wind shear. Term 5 would, in theory, be maximized for stratospheric applications where a large mean wind shear is found over the averaging time period. As will be demonstrated for the 12 December 2002 case, relatively small vertical propagating

waves are capable of producing large mean wind shear values around their periphery. The large wind shear over a short distance would act to produce a non-negligible contribution to the TKE tendency.

The sixth term of Equation (B5) represents the contribution of TKE from the rate of change in the vertical of turbulent transport, hereafter referred to as *Term 6: Turbulent Transport*. The term that results is similar to a vertical TKE flux; and the contribution to TKE tendency comes from the vertical derivative. According to S88, on a local scale, Term 6 acts to either enhance (retard) TKE generation depending on where there is flux convergence (divergence). If there is more flux into a given layer than leaves in that layer, then the magnitude of the TKE increases (S88). Stull (1988) comments that Term 6 really does not create or destroy TKE, but rather re-distributes it within a given layer. For a stratospheric case, where vertical perturbations are large, the author hypothesizes that the greatest contribution to TKE creation (destruction) would be in a situation where large values of TKE are juxtaposed with strong upward (downward) perturbation velocities.

The seventh term of Equation (B5) represents the creation and destruction of TKE by pressure perturbations, which is called the “pressure correlation” term by S88.

Hereafter, the pressure correlation term is referred to as *Term 7: Pressure Perturbation*. S88 comments that very little is known about this term from observational data since it is difficult to measure a static pressure perturbation flux in the atmosphere. However, in a numerical model such as the STRATONHMASS, the pressure perturbation term can be output directly from the model. Term 7 can then be calculated directly, given that the TKE is output at the same time interval. The author hypothesizes that the contribution from Term 7 would be largest where pressure perturbations and TKE are juxtaposed, most likely above strong convective updrafts, where TKE is large due to momentum variances.

The final term in Equation (B5) is the TKE dissipation, which is always negative and acts to reduce TKE. The eighth term is referred hereafter as *Term 8: Dissipation*. Term 8 is also referred to as the eddy dissipation rate (EDR). The dissipation is from molecular destruction and, thus, an empirical scheme must be employed, as it cannot be calculated directly from the model output as the other terms in Equation (B5). The STRATONHMASS outputs the dissipation at each output along with the rest of the parameters listed in Equation (B4). The TKE dissipation (EDR) scheme is not described here, but is a high order scheme that does output the dissipation at every level outside the PBL.

2.3. TKE Tendency Equation in Pressure Coordinates

Though not described explicitly in S88, for a model data set, it is often convenient to express variables in pressure coordinates as opposed to height coordinates. For most data sets from field studies, parameters are measured as a function of height, which is known given the height of the instrument. However, in a numerical model, the vertical axis is most often expressed as a normalized coordinate system, such as σ , which can easily be output into corresponding pressure coordinates. Graphical interpretation packages such as GEMPAK most often work with data that is plotted in pressure coordinates.

In addition to the overall general use of pressure versus height coordinates, the height spacing between vertical σ levels is uneven for the STRATONHMASS model. The model's post-processing package automatically extrapolates the σ levels into corresponding pressure values, but does not for height coordinates. The uneven nature of the height spacing between σ levels introduces a major data analysis problem that may require quite a bit of programming to address. Therefore, for the purposes of this study, the use of pressure coordinates is most convenient.

For the purposes of this study using a STRATONHMASS simulation-produced data set, Equation (B5) must be expressed in pressure coordinates. To do so, we consider the vertical derivative of the arbitrary quantity Ω expressed as:

$$\frac{\partial \Omega}{\partial z} = \frac{\partial \Omega}{\partial p} \frac{\partial p}{\partial z} \quad (\text{B6})$$

from a generalized coordinate transformation, taken from Bluestein (1993). If we assume that the atmosphere is hydrostatically balanced within the layer of the derivative, then we can invoke the hydrostatic approximation, such that Equation (B6) becomes:

$$\frac{\partial \Omega}{\partial z} = -\rho g \frac{\partial \Omega}{\partial p} \quad (\text{B7})$$

The author acknowledges that the output used is from a non-hydrostatic model, and that the hydrostatic balance is not applicable to convective systems. However, the hydrostatic approximation is only made over the difference between the levels in which the derivative is calculated (see Section 2.4). The pressure differences between the levels are between 5 and 10 millibars, and even for the stratosphere, only correlate to a 0.2-km difference in levels. Thus, the hydrostatic approximation is likely valid within those layers for the duration of the model run. Sensitivity studies to a higher-order coordinate transformation would be needed to exactly quantify the error introduced by using the hydrostatic approximation with the levels between the derivatives.

Using Equation (B7), we can rewrite Equation (B5) as:

$$\begin{aligned} \frac{\partial \bar{e}}{\partial t} \approx & -u \frac{\partial \bar{e}}{\partial x} - v \frac{\partial \bar{e}}{\partial y} + \bar{w} \rho g \frac{\partial \bar{e}}{\partial p} + \frac{g}{\theta_v} (\bar{w}' \theta_v') \\ & + (\bar{u}' \bar{w}') \rho g \frac{\partial \bar{u}}{\partial p} + \rho g \frac{\partial}{\partial p} (\bar{w}' e) + g \frac{\partial}{\partial p} (\bar{w}' p') - \varepsilon \end{aligned} \quad (\text{B8})$$

Equation (B8) is the TKE tendency equation written in pressure coordinates, and founds the basis for the pressure-based TKE budget presented in Section 3. For the simplicity of the calculations, the author takes the average air density to be 1.25 kg/m^3 and gravity as 9.80665 m/s^2 .

2.4. Finite Difference Scheme

In order to represent Equation (B8) to calculate derivatives using actual data, finite difference schemes must be implemented to approximate the derivatives. Following Lin (2005), the most stable and useful finite difference scheme is a centered in time and centered in space approach. From Equation (B8), we see that only spatial derivatives are necessary to quantify the budget, since we are solving for a time tendency on the right hand side.

The horizontal derivatives, seen in Term 1 and Term 2 of Equation (B8), can be calculated directly using the GEMPAK numerical graphics package. Due to time constraints, the horizontal derivatives for the case study presented in Section 3 are calculated using GEMPAK's horizontal derivative scheme. The functions DDX and DDY are valid for any scalar field Ω , and follow a second-order centered spatial finite difference.

Because the choice of vertical axis is left to the user, the GEMPAK numerical graphics package does not calculate a vertical derivative of any sort. From Equation (B8), we see that Terms 3, 5, 6, and 7 all require a vertical derivative of some scalar quantity or product of quantities. In order to account for these terms, one must develop a finite difference scheme that is consistent with the horizontal derivatives calculated in Term 1 and Term 2. From Lin (2005), a first-order centered spatial finite difference for some arbitrary quantity Ω is done vertically, such as shown in Equation (B9):

$$\frac{\partial \Omega}{\partial p} \approx \frac{\Omega^{\tau}_{i,j,p+1} - \Omega^{\tau}_{i,j,p-1}}{2\Delta p} \quad (B9)$$

The scalar quantity Ω is taken at time step τ from two different pressure levels above and below the level at which the derivative is calculated. Since pressure has the opposite sense as height, it must be pointed out that the first observation corresponds to the value of Ω at a higher-pressure level, meaning lower height. Fortran programs were written to calculate the vertical derivatives for the various scalar quantities shown in Equation (B8), and are described in further detail in Section 3.

Though the horizontal derivatives are of higher order accuracy than Equation (B9), the two schemes are still comparable from a semi-quantitative viewpoint. Due to time constraints, a comparison of Equation (B9) to a second-order centered vertical scheme was unable to be completed, but is planned to be part of future work on the project.

3. TKE BUDGET ANALYSIS: 12 DECEMBER 2002 STRATONHMASS SIMULATION IN PRESSURE COORDINATES

3.1. Model Simulation Description

The STRATONHMASS model was run at a horizontal grid spacing of $\Delta x, \Delta y = 222$ m for the 12 December 2002 case using the pressure coordinated transformation discussed in Section 2.3. The model was initialized at 2209 UTC, 12 December, and ran

approximately 35 minutes, with the last model output time of 2244 UTC, 12 December. The model was initialized using NCAR NARR reanalysis data that includes data above 100 millibars, making computations in the stratosphere possible.

Figure B2 shows the terrain map for this 222-meter simulation. The grid area is very small and only covers a small portion of far eastern Texas and western Louisiana. The simulation was run using the Kain-Fritch convective parameterization scheme and Lin et al. (1983) microphysics package. The model was run with a TKE option for the PBL, but this is of no concern since we are dealing with the upper level regions for the TKE budget.

The model's time step is approximately 0.07 s, but the output from the model run was only available every 54 seconds. This totaled 40 model simulation times for each field over the 35-minute model run. Due to a time formatting error within the GEMPAK graphics package, five of these 40 model simulations times had to be neglected. Thus, the TKE budget is performed using 35 total model simulation times and the initial state.

The model was run with 90 vertical σ levels. For the purposes of the TKE budget analysis, however, only data between 300 mb and 10 mb was considered. While the entire vertical structure of the model can be ingested into the programs and scripts necessary to run the TKE budget, the computational time required is not feasible if one is only interested in stratospheric applications. Model data that lie between the 300 millibar and 100 millibar surfaces are available every 10 millibars, while data above 100 millibars to the model top at 10 millibars are available every 5 millibars.

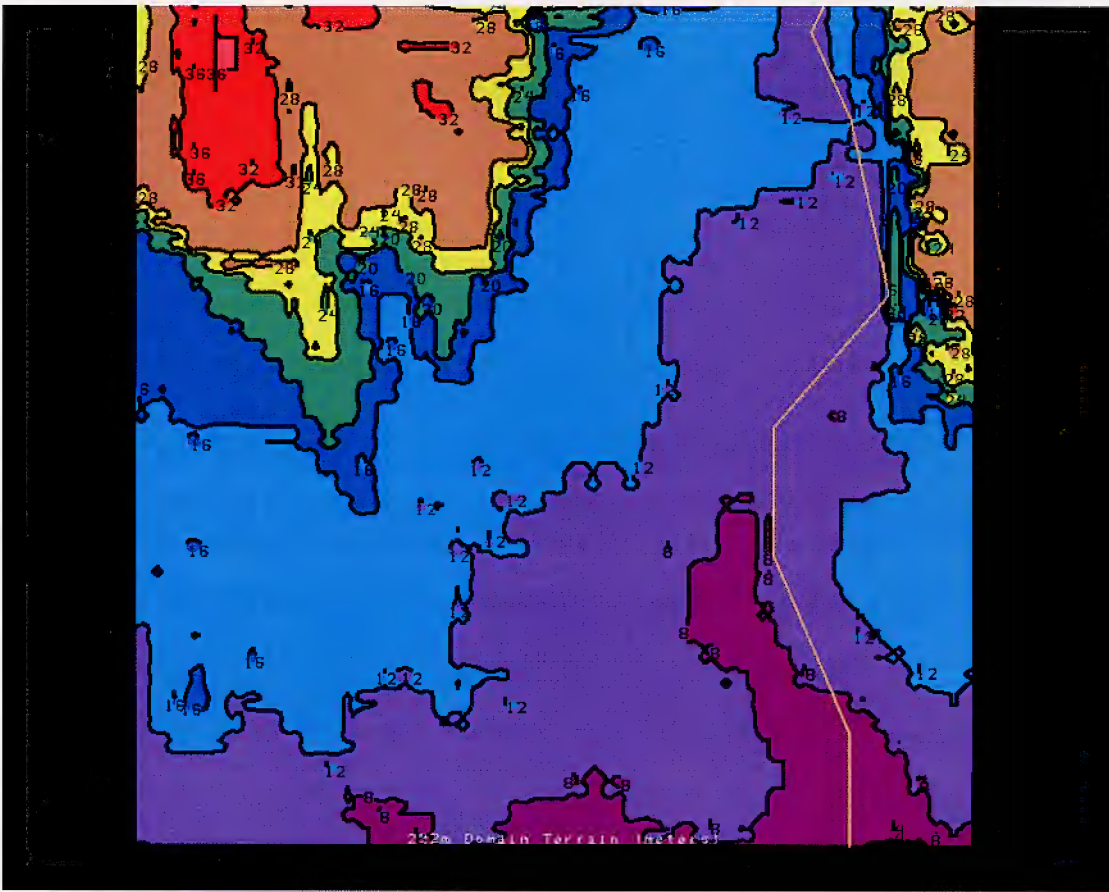


Figure B2. Domain terrain map for the 222-m STRATONHMASS simulation, shown in meters, for the 12 December 2002 case.

In the model, as was true with satellite and ground-based GPS observations, strong convection forced a large-amplitude gravity wave that propagated within a wave duct north of a strong warm front/stable layer. In Paul Suffern's 222-m output data available on the Mesolab server, a strong vertically propagating gravity wave, initiated by the convection below, traveled up the troposphere and into the lower stratosphere. The convection top/overshoot from the w-relative wind fields was around 170 mb, penetrating 50 mb into the stratosphere. According to model-derived soundings, the tropopause was located around 210 mb. From the plots of the total wind fields and isentropes (not shown), the levels at which the budget are most interesting are between 120 mb and 70 mb. Figure B3 shows the cross-sections that are taken for the graphics that follow in Sections 3.2-3.9. Of note, the only cross-section plotted from Figure B3 is the cross-section labeled M2.

3.2. Parameter Extraction and Reynolds Decomposition

As can be seen from Equation (B8), several different variables need to be extracted from the model output in order to perform a preliminary TKE budget analysis. The STRATONHMASS model was formatted to output the U-relative, V-relative, and W-relative wind field in accordance with S88's restriction that the coordinate system be aligned with the mean wind field. The u, v, and w model-relative winds are then averaged over the 35-minute simulation using Equation (B2). These terms, denoted as the mean u, v, and w wind fields, are used in Terms 1, 2, 3, and 5 from Equation (B8).

In order to calculate perturbations from this 35-minute average, Equation (B4) was used to produce a perturbation data set, denoted u' , v' , and w' , from the respective fields and averages calculated using Equation (B2). Figures B4 and B5 show the M2 cross-section for the u' and w' fields at forecast time $t = 19$. The perturbation fields, when looped for each model simulation time, show a vertically propagating wave coming from below 300 millibars and moving into the stratosphere. The full physical interpretation of these fields is deferred to future research.

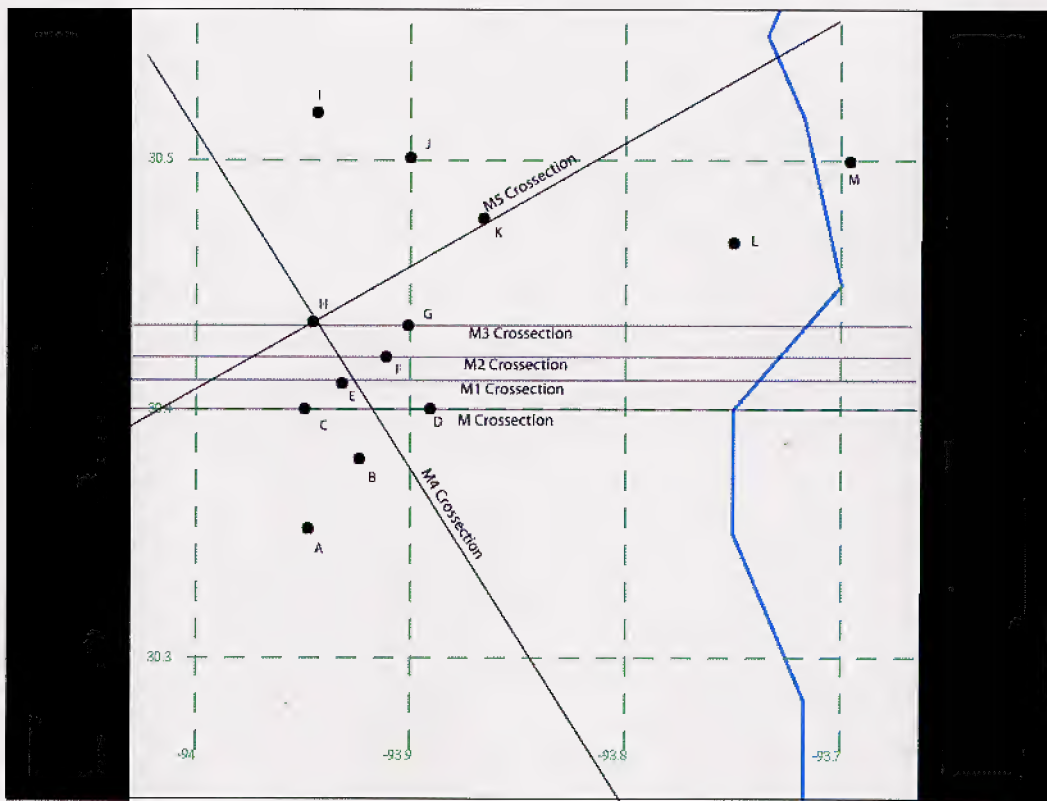


Figure B3. Domain map showing the location of various cross-sections for the 222-m STRATONHMASS simulation of the 12 December 2002 case. For the purposes of this paper, the only cross-section that is used is M2, in the center of the map.

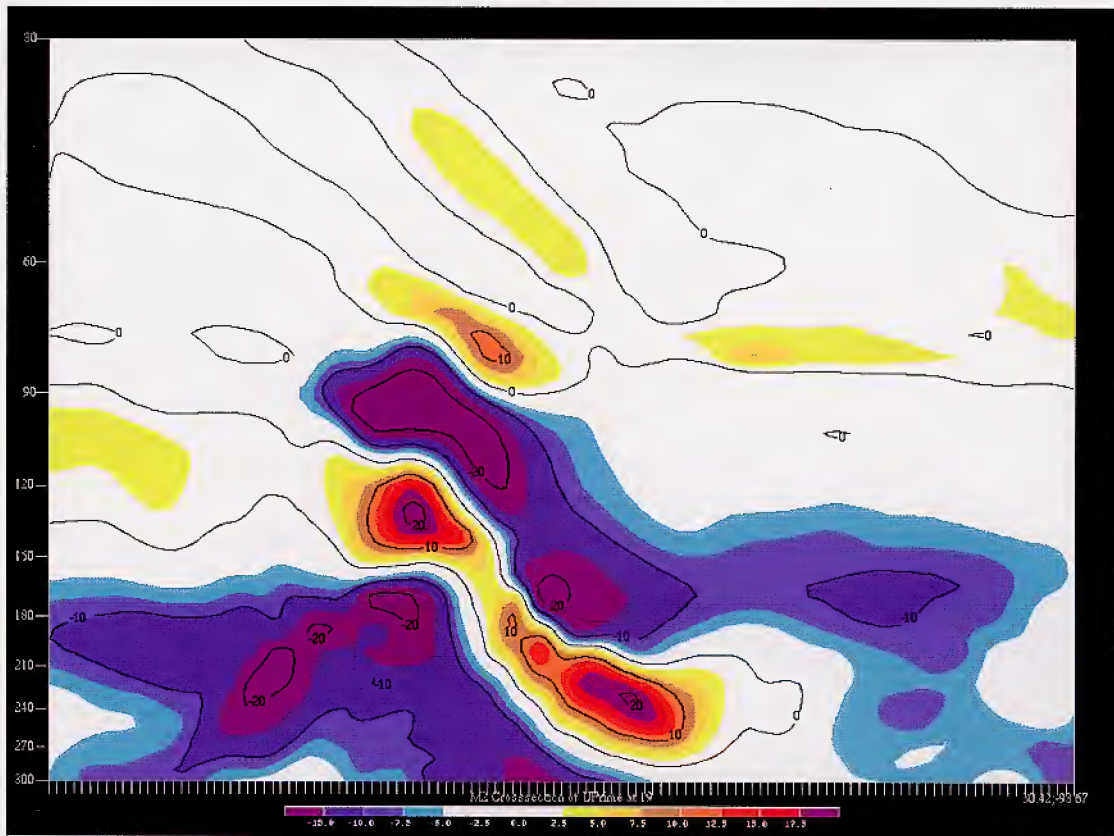


Figure B4. U' (color shaded) for the 12 December 2002 simulation, valid at 2238 UTC, 12 December. The main stratospheric wave is located roughly corresponding to the positive/negative couplet centered between 150-80 millibars.

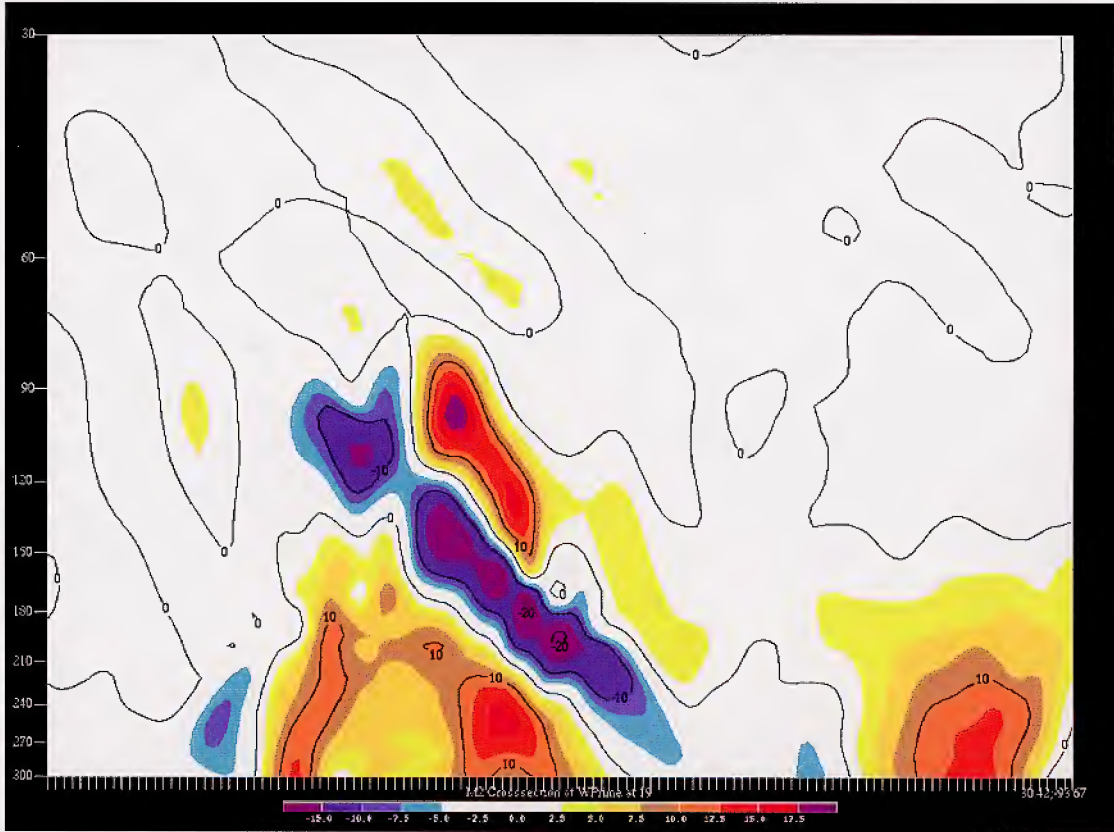


Figure B5. As with Figure B4, except for w' . The wave tilt is clearly seen here in the vertical velocity perturbations, with a very nice positive/negative/positive couplet phase tilted with the stratospheric wave.

The same Reynolds decomposition is applied to the virtual temperature field from the MASS model output. First, the virtual temperature field is converted to virtual potential temperature, and then decomposed using Equations (B2) and (B3). Figure B6 shows the virtual potential temperature perturbation (θ_v') for the 12 December case at time $t = 19$, the same time as shown in Figures B3 and B4. The large θ_v' corresponds to the same location where the stratospheric wave is increasing the heights, and the small θ_v' corresponds to the location where the wave is decreasing the heights. Further research must be done on this hypothesis, but quick visual inspection and conferencing with Dr. Michael Kaplan and Paul Suffern aided this argument.

3.3. TKE Tendency Due to Terms 1 and 2: U and V-Advection

Using Equation (B8), Term 1 and Term 2 were calculated using the time-averaged u and v mean wind field and GEMPAK's horizontal derivative scheme (DDX and DDY) for the TKE field. Following Equation (B3), the average TKE field was also calculated for the 35-minute simulation. Thus, the contributions from Term 1 and Term 2:

$$\frac{\partial \bar{e}}{\partial t} \approx -u \frac{\partial \bar{e}}{\partial x} \dots \quad TERM 1$$

$$\frac{\partial \bar{e}}{\partial t} \approx -v \frac{\partial \bar{e}}{\partial y} \dots \quad TERM 2$$

can be quantified over the 35-minute model simulation.

Figure B7 shows Term 1 plotted for the M2 cross section averaged over the 350-minute domain.

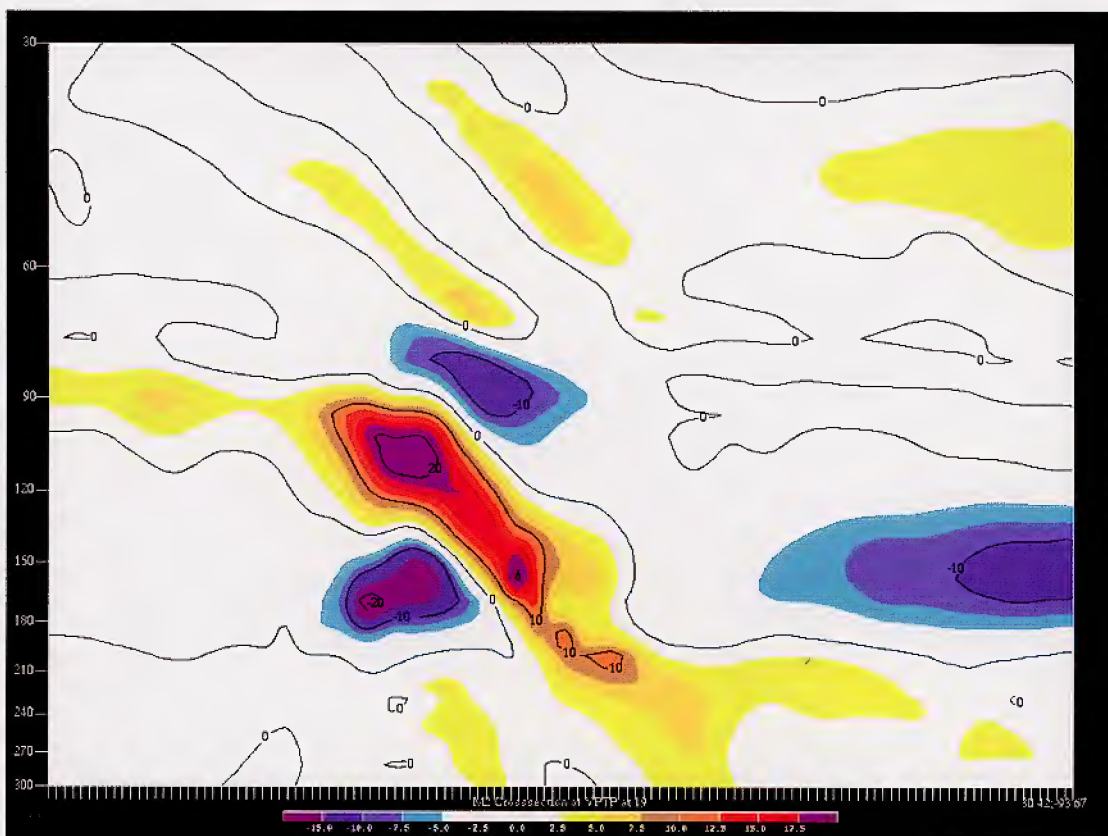


Figure B6. As with Figures B4 and B5, but for perturbation virtual potential temperature. The field is a bit higher up than the u' and w' maxima, but is of the same shape and orientation at this time.

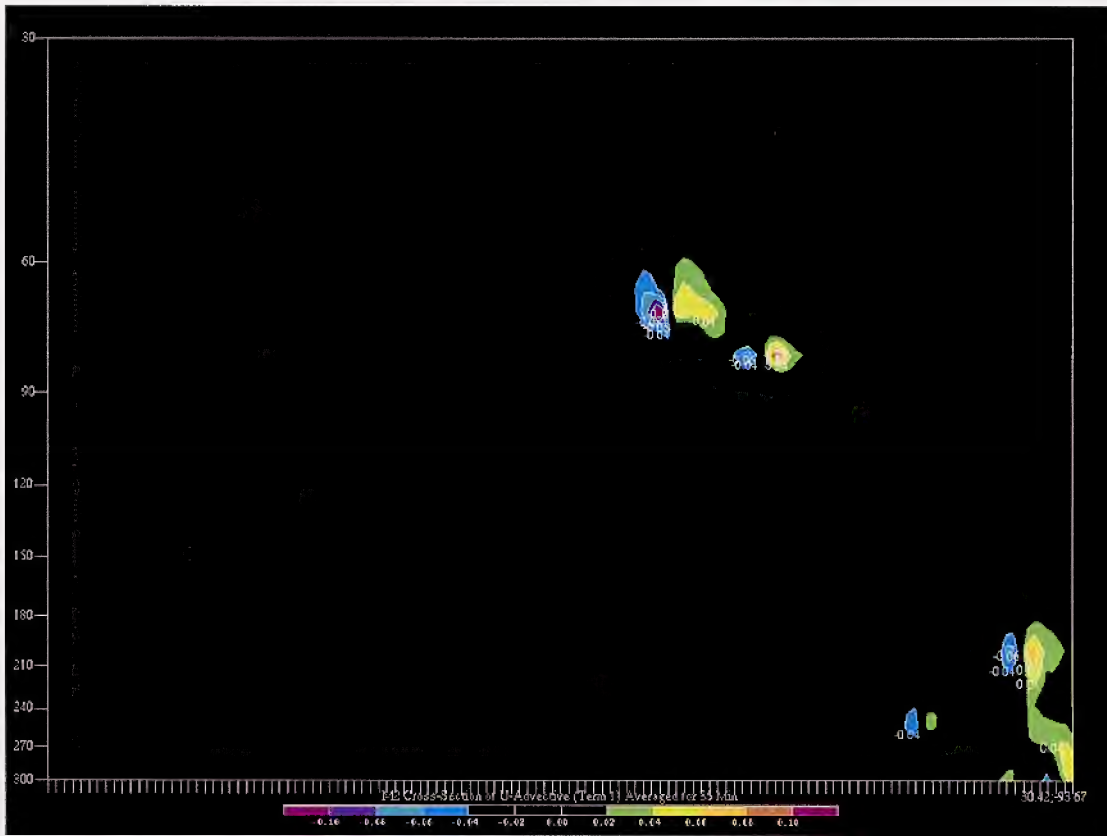


Figure B7. Term 1 (U-Advection) plotted for the 35-minute time averaged field. Notice the lone maxima and minima couplet centered around 70 mb, much higher than the actual stratospheric wave.

Term 1 is relatively small everywhere within the domain except near the apex of the breaking stratospheric wave, which is zoomed-in and shown close-up for Figure B8. These results are consistent with the findings of S88, and Term 1 is likely quantitatively small compared to the other terms.

Similar findings are found in Term 2, shown in Figure B9. Like Term 1, Term 2 is small except for small pockets in the upper troposphere where the stratospheric wave has broken. Term 2 is also likely relatively small compared to the other terms in the TKE budget. Further analysis, particularly a small time average from Equation (B3), is needed and is planned in future research.

3.4. TKE Tendency Due to Term 3: W-Advection

Using Equation (B8), Term 3 was calculated using a separate Fortran program, written by the author. The program calculates the vertical derivative of turbulent kinetic energy, which has been averaged over the 35-minute model run. From Equation (B9):

$$\frac{\partial \bar{e}}{\partial p} \approx \frac{\bar{e}_{i,j,p+1} - \bar{e}_{i,j,p-1}}{2\Delta p}$$

Using the w average wind field, Term 3 can be calculated using Equation (B8):

$$\frac{\partial \bar{e}}{\partial t} \approx \dots w \rho g \frac{\partial \bar{e}}{\partial p} \dots \quad TERM3$$

Figure B10 shows the 35-minute averaged cross-section for Term 3. Because w is being used here instead of omega, the plot is strictly qualitative. The first set of large Term 3 values are shown zoomed in Figure B11, in a layer between 300 and 250 millibars. The area of strongest vertical motion associated with the convection lies just below this layer and, thus, the convection itself drives higher values of Term 3 here. The second set of large Term 3 values are shown zoomed in Figure B12, in the lower stratosphere between 120 and 65 millibars. Here, the breaking stratospheric wave has created a large vertical gradient in turbulent kinetic energy.

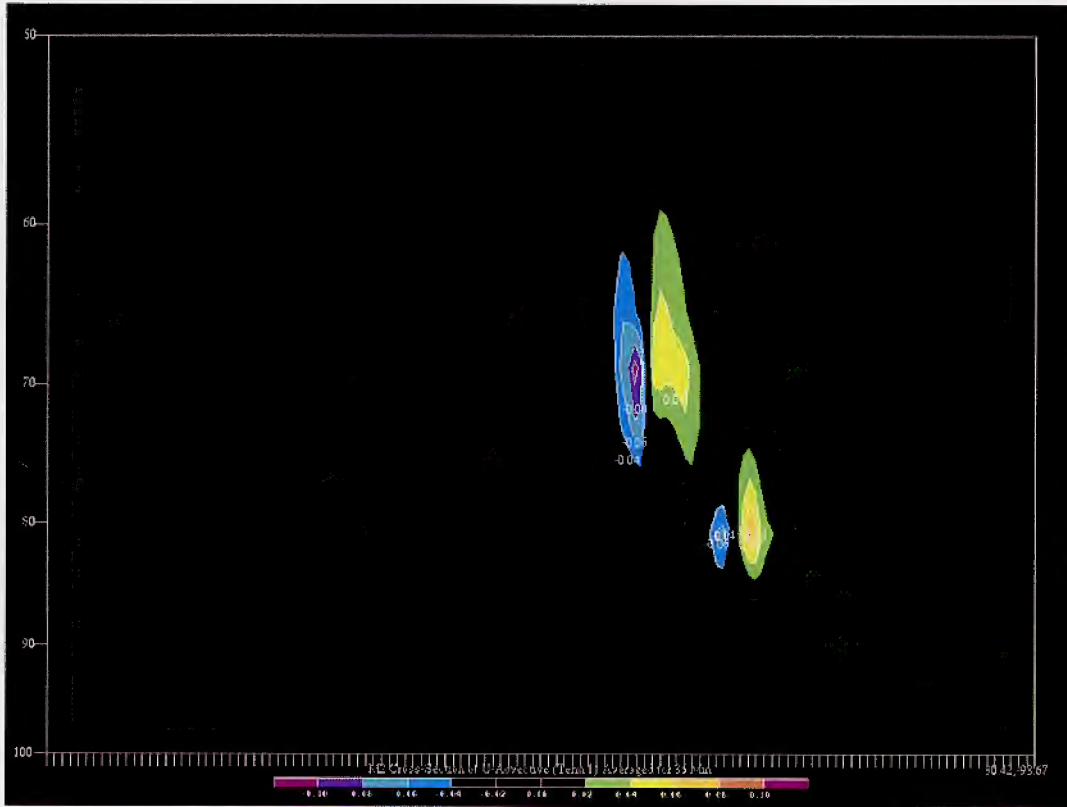


Figure B8. Term 1, U-Advection. As with Figure B7, but zoomed to a vertical axis of 50-100 mb.



Figure B9. Term 2: V-Advection.

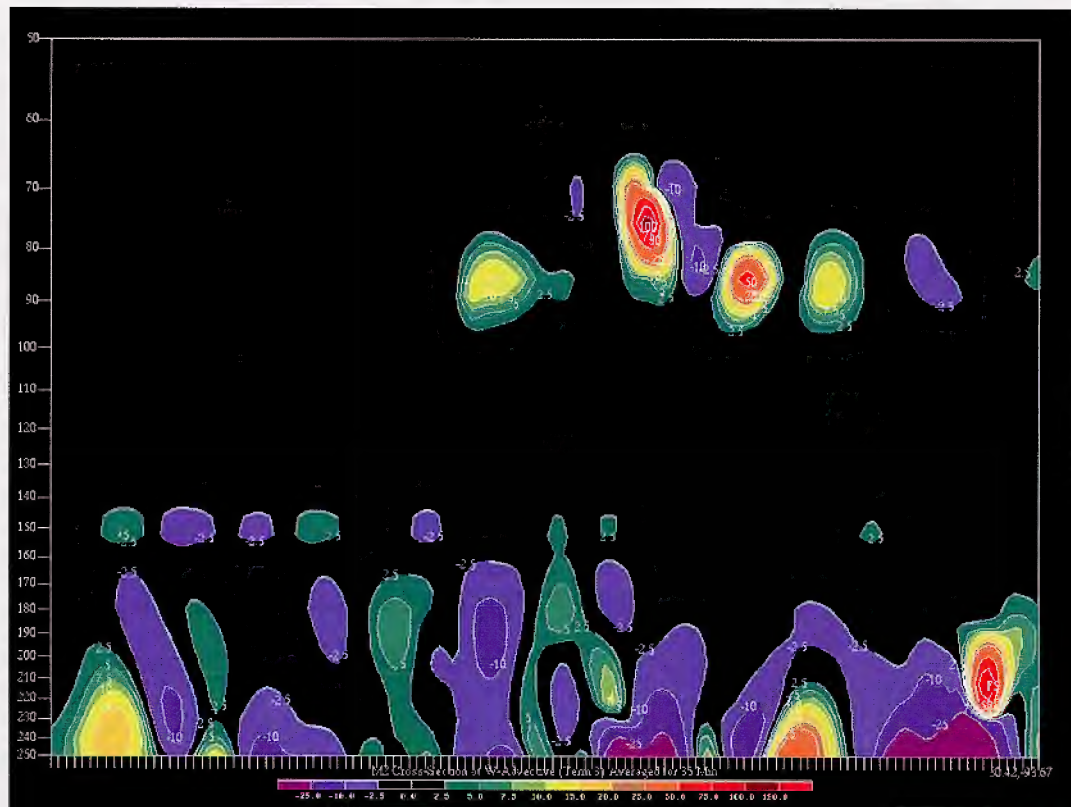


Figure B10. Term 3: W-Advection.

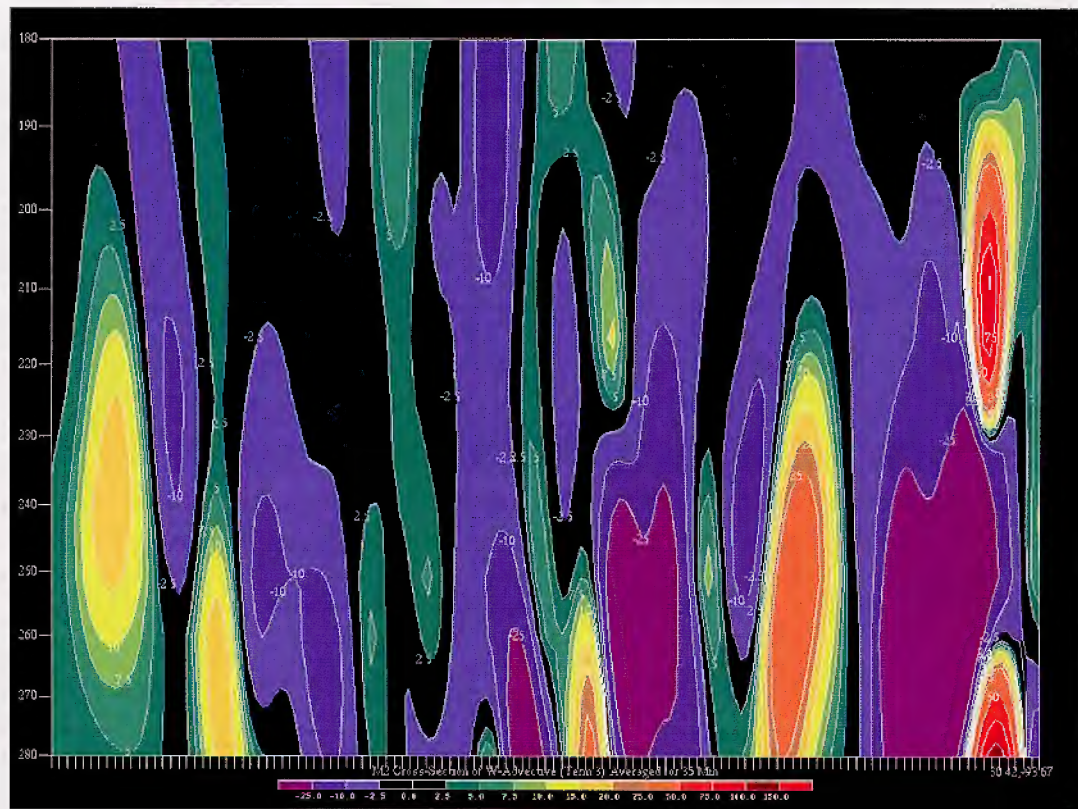


Figure B11. Term 3, W-Advection, with a vertical axis from 180-280 millibars.

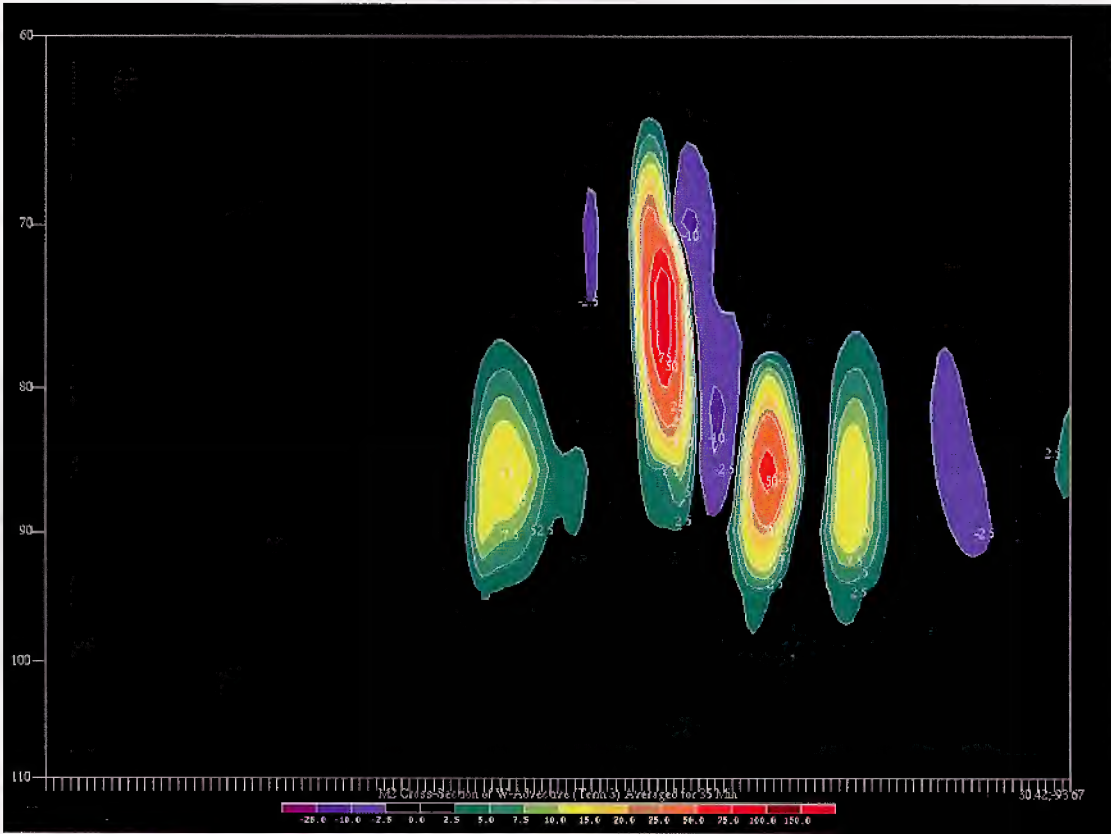


Figure B12. Term 3, W-Advection, but with a vertical axis from 60-110 millibars.

Figure B13 shows the same color-filled values for Term 3, with contoured values of $\frac{\partial \bar{e}}{\partial p}$. Clearly, the large Term 3 values are driven primarily because of a high gradient in $\frac{\partial \bar{e}}{\partial p}$ rather than a flux of w-momentum. The area of highest Term 3 lie above the stratospheric wave break, leading the author to hypothesize that the rapid change from large to small TKE values above the wave ($d\bar{e} < 0$ and $d\bar{p} < 0$) acts to generate higher TKE generation there. This result will be tested in future research, as aircraft who choose to fly over convection may actually be flying into areas of high TKE generation in the lower stratosphere holds in further applications.

3.5. TKE Tendency Due to Term 4: Buoyancy

Using Equation (B8) and the perturbation fields, Term 4 is calculated using the 35-minute average virtual potential temperature, and the product of w' and θ_v' . From Equation (B8):

$$\frac{\partial \bar{e}}{\partial t} \approx \dots \frac{g}{\theta_v} \overline{(w' \theta_v')} \dots TERM4$$

The quasi-heat flux $w' \theta_v'$ was subsequently averaged over the 35-minute model run to produce Figure B14, which is Term 4 plotted in the same M2 cross-section as the other figures. Figure B14 shows an interesting couplet pattern centered around 90 millibars; about 15-20 millibars lower than the highest values in Term 3. Further investigation of these phenomena will be required to gain a physical understanding to the couplet's meaning.

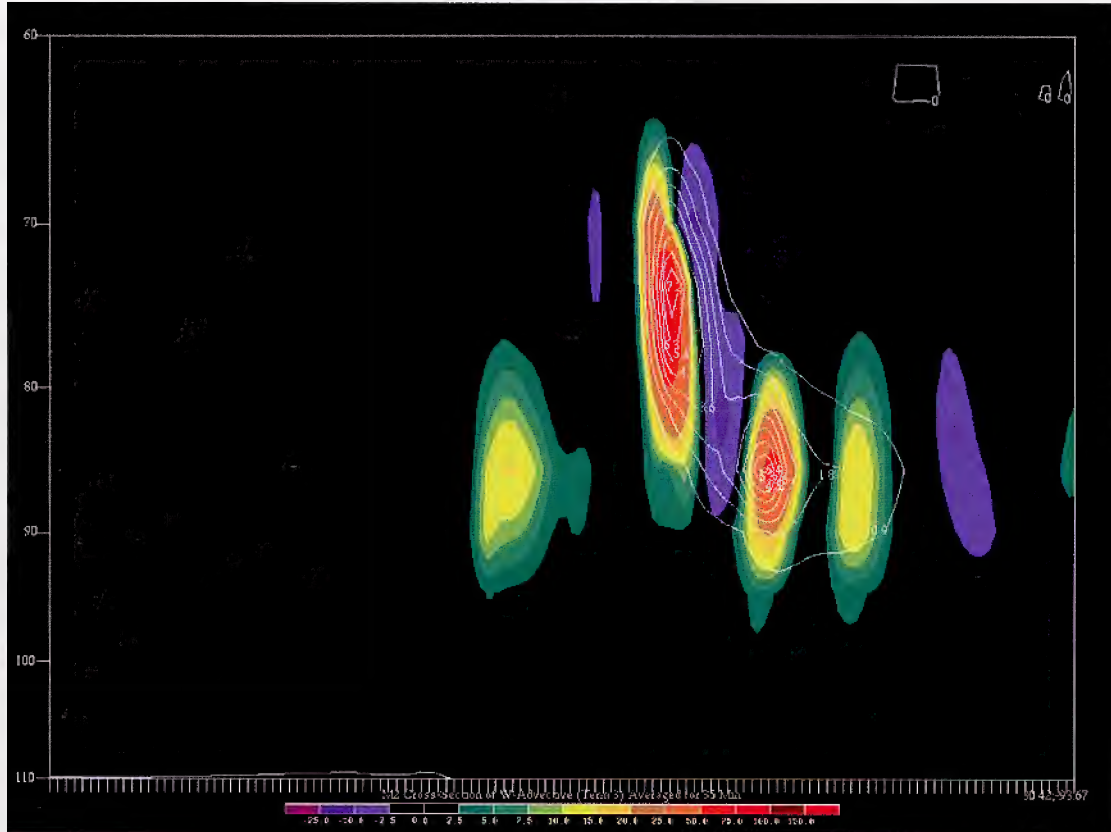


Figure B13. Term 3, W-Advection, with contoured values of de/dp .

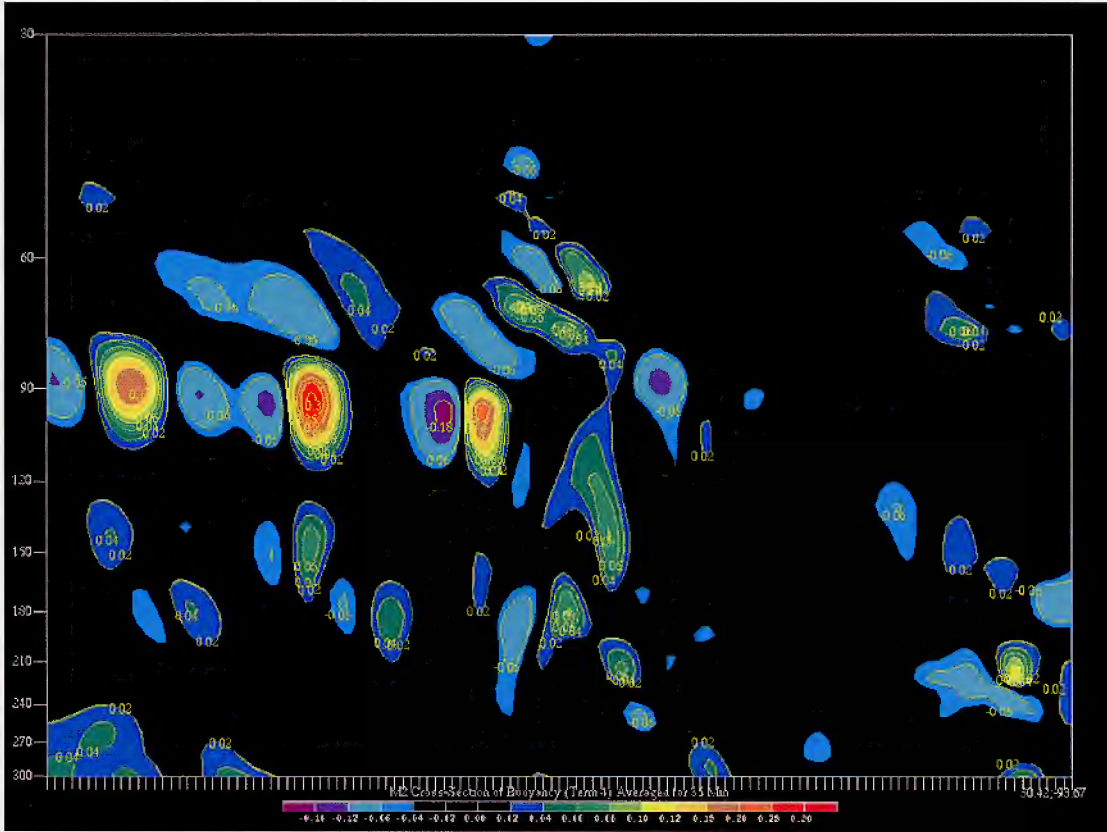


Figure B14. Term 4, Buoyancy production.

3.6. TKE Tendency Due to Term 5: Mechanical Shear

Using Equation (B8), and the perturbation fields, Term 5 is calculated using the u' and w' fields multiplied together and averaged over the 35-minute model run using Equation (B2). The average basic state shear of the u -mean wind is calculated using a separate Fortran program and has different resolution above and below 100 millibars as described earlier in this paper. From Equation (B8), Term 5 is expressed as:

$$\frac{\partial \bar{e}}{\partial t} \approx \dots + (\bar{u}' \bar{w}') \rho g \frac{\partial \bar{u}}{\partial p} \dots \quad TERM5$$

Figure B15 shows the 35-minute average for Term 5 using the same M2 cross-section as the other figures.

The most noteworthy information about Figure B15 is the anomalously high values of Term 5 throughout a large part of the domain. At the present time, the author speculates that the coordinate transformation may be the culprit, however, further investigation is necessary to be certain. However, though the magnitude is much too

large, the pattern of mechanical shear production is consistent with theory. Since the stratosphere is extremely stable, one suspects that the dominant production term for the TKE tendency equation would be mechanical shear, due to the large gradient in wind speed produced by the wave.

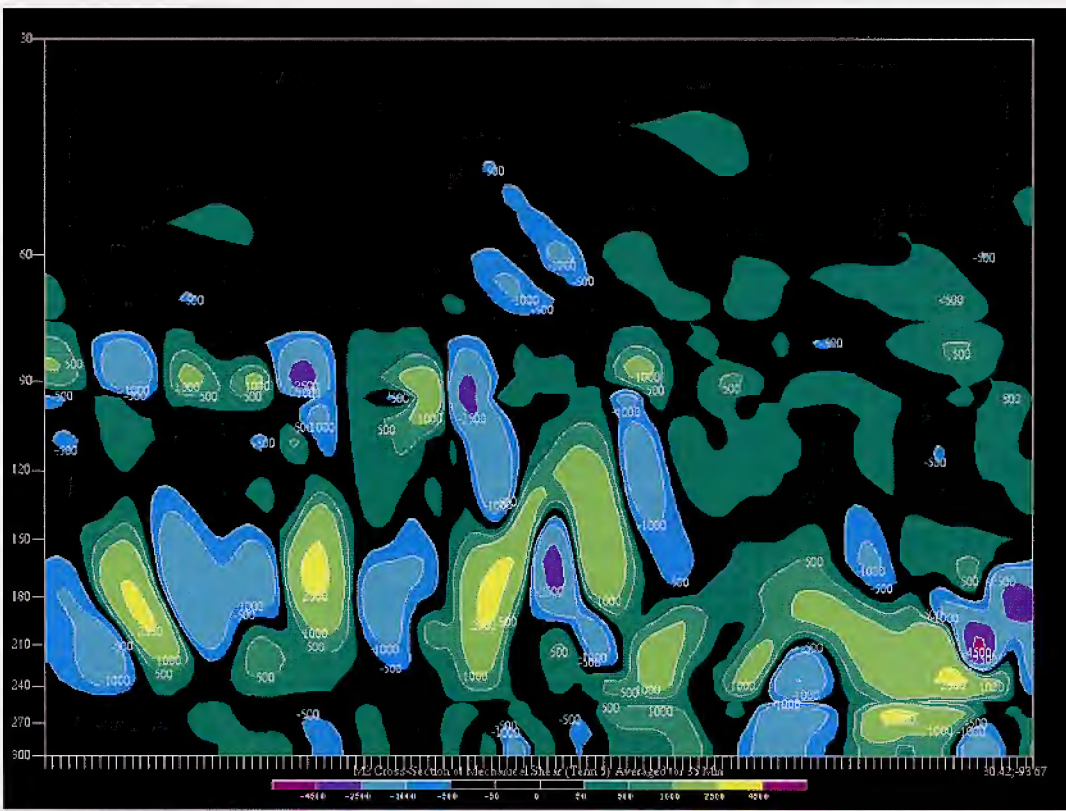
3.7. TKE Tendency Due to Term 6: Turbulent Transport

Using Equation (B8) and the perturbation fields, Term 6 is calculated using the w' and turbulent kinetic energy (e) fields multiplied together and averaged over the 35-minute model run using Equation (B2). The quantity $w'e$ represents the turbulent flux of TKE from the vertical velocity perturbation. From Equation (B8), Term 6 is expressed as:

$$\frac{\partial \bar{e}}{\partial t} \approx \dots + \frac{\partial \bar{w'e}}{\partial p} \dots \quad TERM6$$

Figure B16 shows the 35-minute average for Term 6 using the M2 cross-section.

There are two primary regions of interest in Figure B16. First, several large Term 6 maxima appear near 100 mb. As speculated in Section 2, Term 6 is likely largest where gradients in large values of w' and e are juxtaposed. Further investigation of the magnitude of w' and e in this layer are necessary to determine why there are positioning maxima there. In addition, a couplet in Term 6 appears on the eastern half of the domain in far western Louisiana. According to discussion with Mr. Suffern, convection is ongoing in this region not tied directly to the vertically propagating gravity wave.



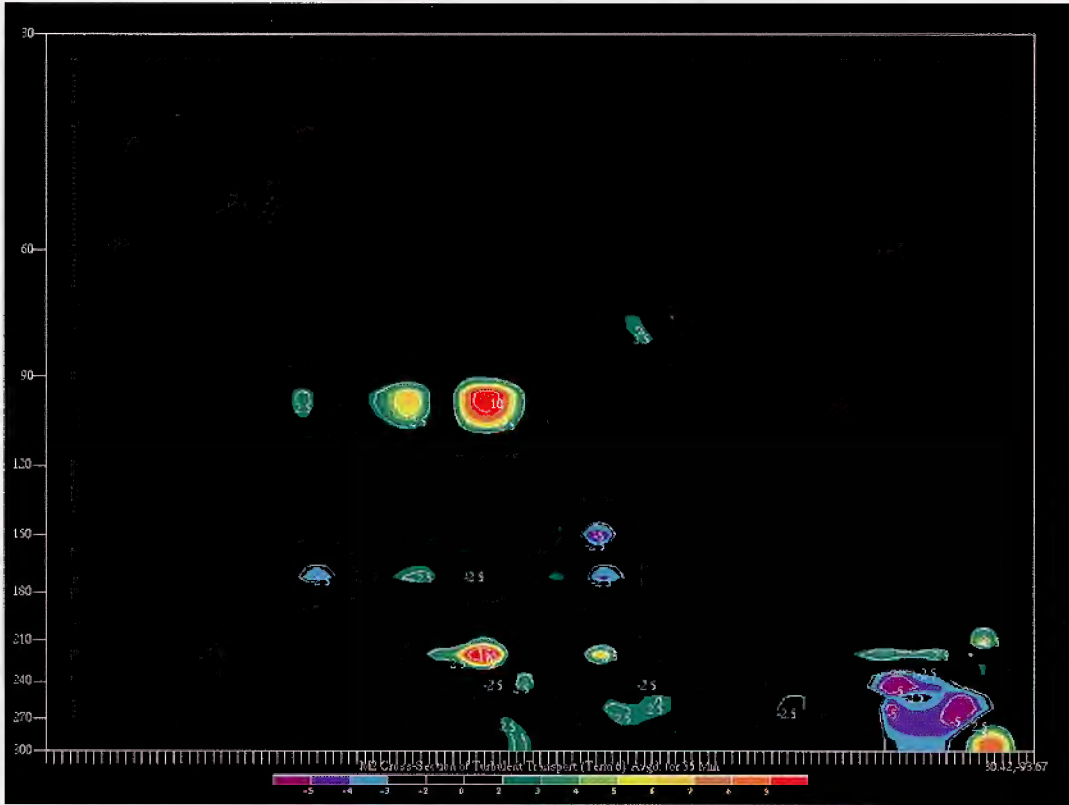


Figure B16. Term 6, Turbulent transport.

3.8. TKE Tendency Due to Term 7: Pressure Perturbations

Using Equation (B8) and the perturbation fields, Term 7 is calculated using the w' and p' fields multiplied together and averaged over the 35-minute model run using (2.2). The pressure perturbation term is outputted directly from the STRATONHMASS simulation. The quantity $w'p'$ represents the creation and destruction of TKE from the pressure perturbations. From Equation (B8), Term 7 is expressed as:

$$\frac{\partial \bar{e}}{\partial t} \approx \dots + g \frac{\partial w' p'}{\partial p} \dots \quad TERM7$$

Figure B17 shows the 35-minute average for Term 7 using the M2 cross-section. The blotchy nature of the cross-section is partly to blame for the appearance of the data. However, there appear to be several couplets in Term 7 located in the same location as other Terms in the TKE equation. As with the other terms, further analysis is needed to explain the pattern.

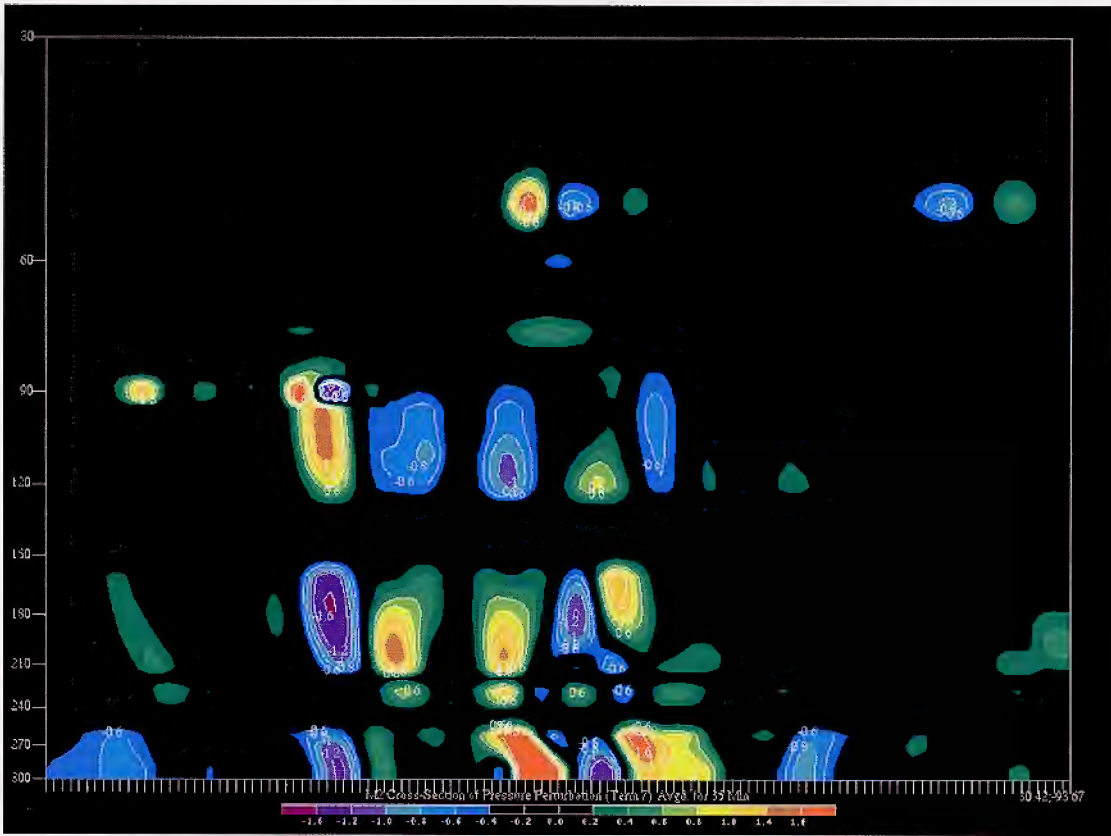


Figure B17. Term 7, Pressure perturbations.

3.9. TKE Tendency Due to Term 8: Dissipation

Using the same Reynolds decomposition algorithm described in sections 2.1-2.3, the average turbulent kinetic energy dissipation was averaged over the 35-minute model period. TKE is a dissipative quantity and, hence, in the absence of Terms 1-7, TKE always acts to be reduced. From S88, TKE dissipation is highest in areas where TKE is large, since overall, TKE is conserved. Figure B18 shows the 35-minute average dissipation from the 12 December case.

Term 8 is surprisingly small in relation to the other terms. This suggests that the explicit calculation of the terms in the TKE budget may be anomalously high on many different levels. The possibility also exists that the model doesn't resolve dissipation as well away from the PBL as is expected by calculating this explicitly.

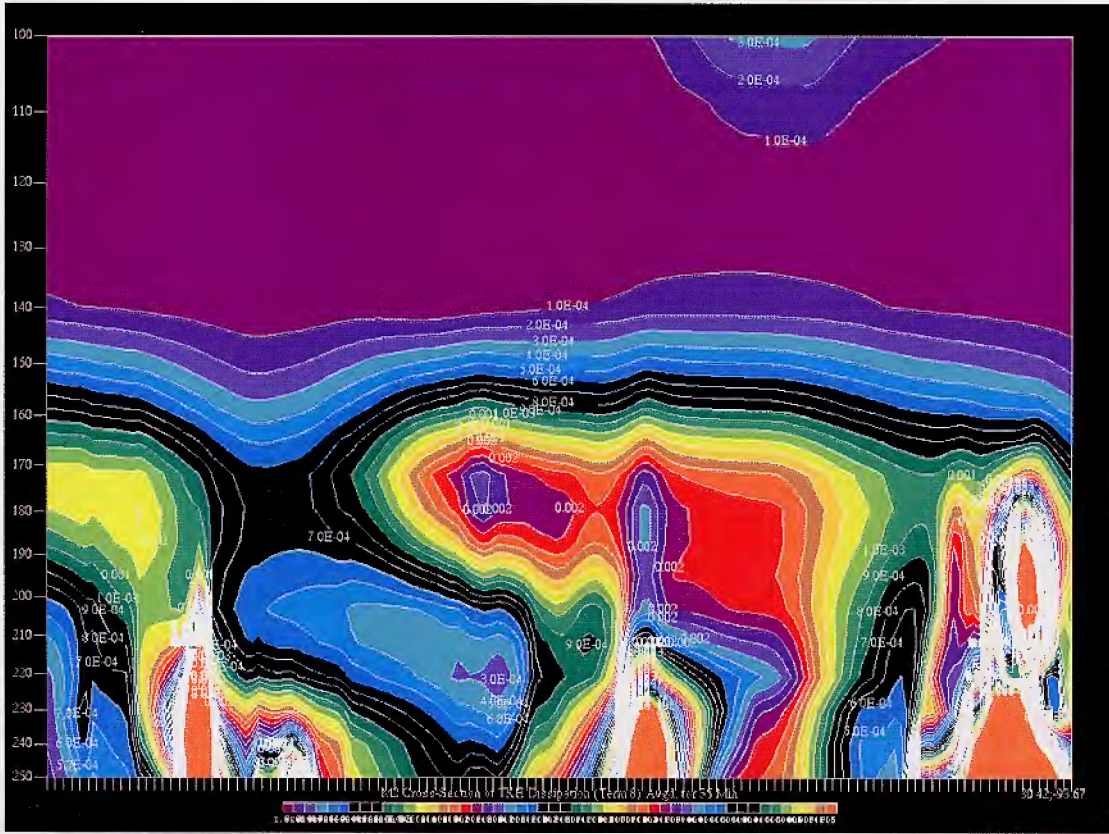


Figure B18. Term 8, TKE dissipation.

4. FUTURE WORK

As highlighted in many sections of this paper, there is much work to be done on the TKE budget algorithm and output for the cases prescribed in the Air Force project. The following research objectives for the Summer 2005 term are proposed:

- Modify current existing model output for height coordinates, and utilize Equation (B5), the TKE tendency equation in height coordinates. This requires that the MASS model's vertical resolution for the stratospheric data are fixed, and set intervals are prescribed in order for the vertical derivatives to be consistent;

OR

- Re-compile the u and v relative wind fields in such a fashion that the GEMPAK program GDOME G can be used to calculate an approximate omega vertical velocity using the continuity equation. The modified TKE tendency in pressure coordinates, given in Equation (B8), can then be used for complete quantitative investigation. A further analysis of the approximations that are invoked will be required. This path may be able to give a quicker mathematical interpretation than the previous suggestion;

- Increase the order of the finite difference scheme employed to calculate the vertical derivatives and compare to the first-order scheme;
- A full quality assurance check of all the data ingested by the TKE budget code to assure that no bad data are responsible for strange budget calculations (see Section 3.9);
- Compare the TKE tendency equation results to that of the model's TKE average over the averaged time period (this will require a direct computational TKE budget). The author and colleagues will then investigate the role of each term in generating TKE tendency physically using wave dynamics and previous literature;
- Complete the TKE budget for all Air Force project cases and regimes as prescribed by Dr. Michael Kaplan;
- Use the TKE budget analysis code and script to develop an EDR budget algorithm that closely resembles that of the TKE budget. The EDR tendency equation (not shown) uses many of the same variables as the TKE budget and should not require a great deal more in the way of calculations and manipulations. The EDR budget would then be calculated for all the Air Force project case studies.

5. CONCLUSIONS

A preliminary TKE budget analysis has been presented for the 12 December 2002 large-amplitude gravity wave case for a model simulation time period of 35 minutes at a 222-m horizontal resolution. Due to various data problems, the TKE tendency equation was written in pressure coordinates and rather than height coordinates. The coordinate transformation necessary to perform many of the calculations leaves the budget to become strictly a qualitative one.

The purpose of this project was to develop the code and perform an initial analysis of the TKE budget for one case study as a stepping-stone to further research. The results presented in Section 3 are purely of a qualitative nature due to the various approximations, data ingestion issues, and coordinate transformations. The development of a skeleton code in which TKE budgets can be calculated is of great significance to the project and future research described in Section 4.

The TKE budget analysis raises many research questions that will require quite a bit of thinking. Are the patterns presented in the terms of physical significance or strictly a byproduct of the calculations within the budget? Many more TKE budgets must be performed on the various case studies in order to begin answering some of these questions. A rigorous physical interpretation of the results is deferred from this conclusion section to further research.

6. SUMMER 2005 RESEARCH UPDATE

As discussed in Section 4, Future Work, several different research goals were described for the Summer 2005 term. The first objective involved utilizing (2.4) to transform the TKE budget into a height coordinate form. After the TKE budget in pressure coordinates was examined closer, it was confirmed that the units were not consistent in the

derivation. The value of the pressure coordinate exercise was to develop the first skeleton code required for the budget and identify the regions of interest.

The TKE budget code was then developed for use in a height coordinate system consistent with the PBL-inspired Equation (B4). Included in this Appendix is the 71-m and 222-m, 12 December 2002, TKE budgets in height coordinates. Cursory examination of the 71- and 222-m TKE budgets indicate a finer-scale resolved turbulence signal within the 71-m run, as well as stronger emphasis on the u and v advection terms. The increase in TKE contribution from the u and v advection terms indicate a stronger horizontal TKE gradient within the 71-m run, consistent with the finer horizontal resolution and the expected resolve turbulence signal. The term calculations for the 71- and 222-m runs are shown in Figures B19-B34. Future analysis and discussion is deferred to future documents due to time constraints.

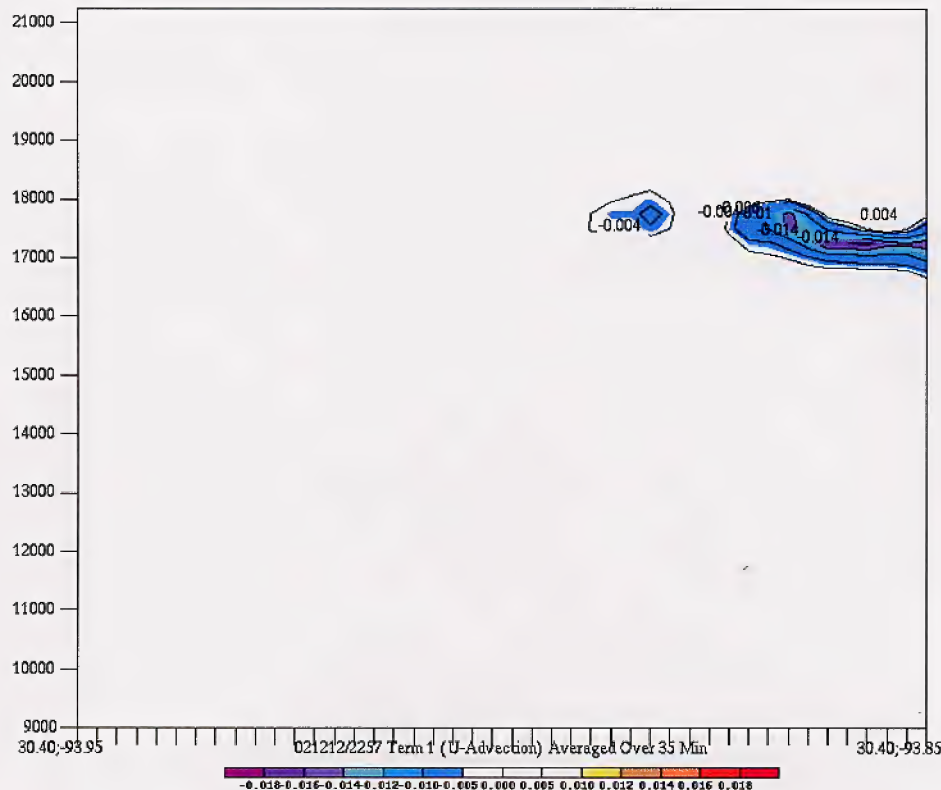


Figure B19.* TKE Budget for 12 December 2002, 222-m case in height coordinates: Term 1, U-Advection.

* Denotes figures inserted as part of Summer 2005 Research Update.

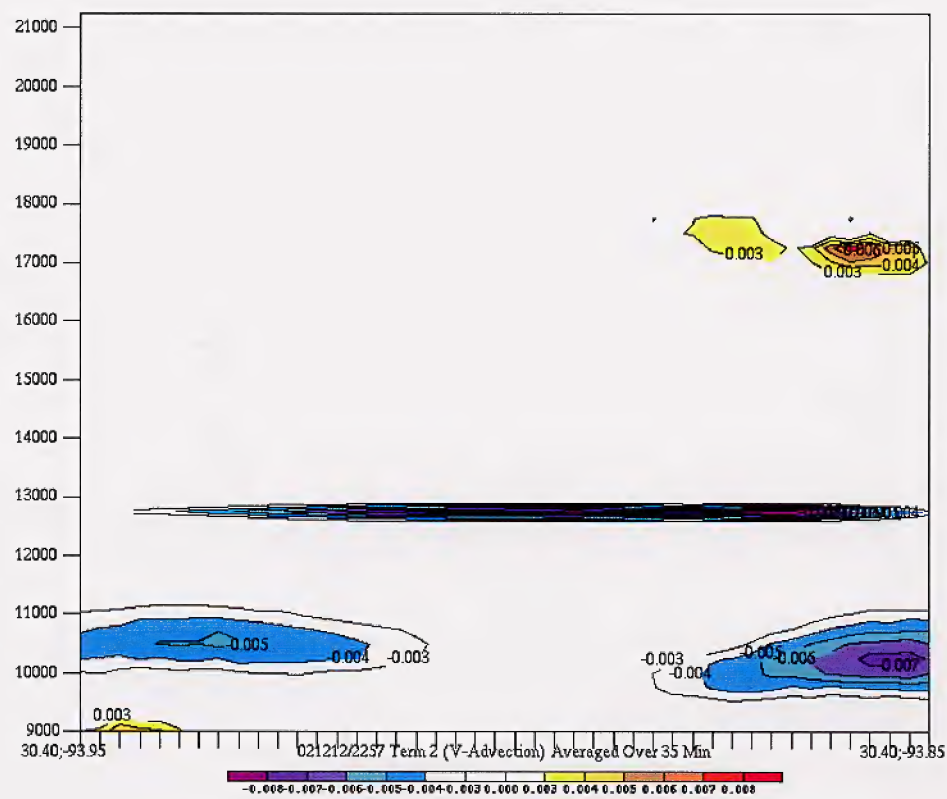


Figure B20.* TKE Budget for 12 December 2002, 222-m case in height coordinates: Term 2, V-Advection.

* Denotes figures inserted as part of Summer 2005 Research Update.

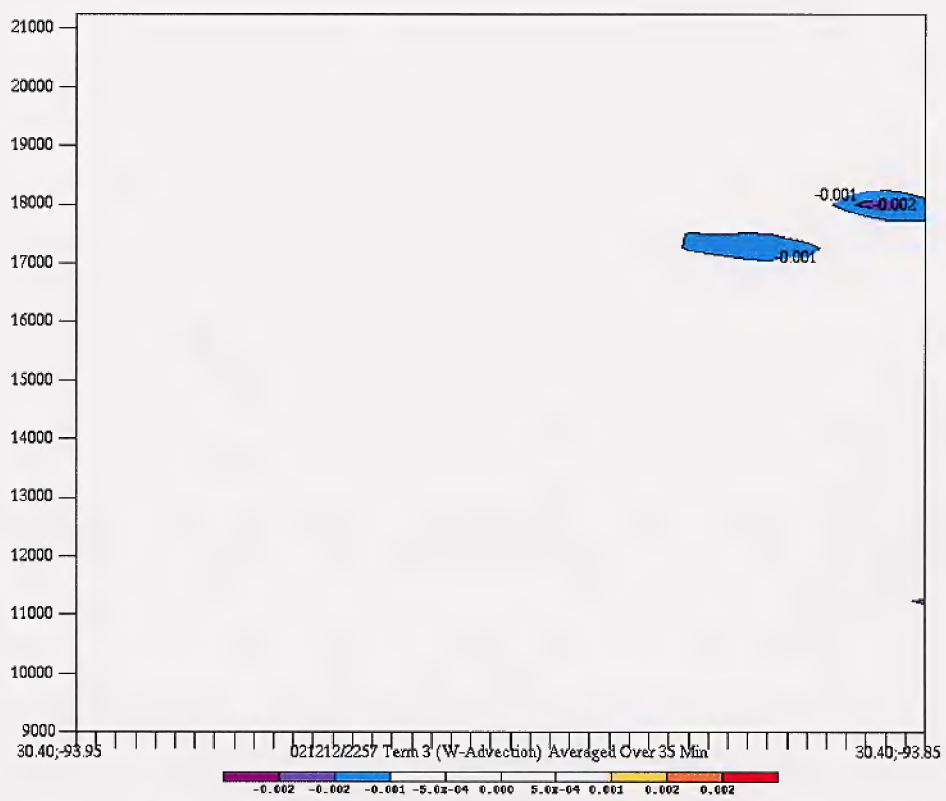
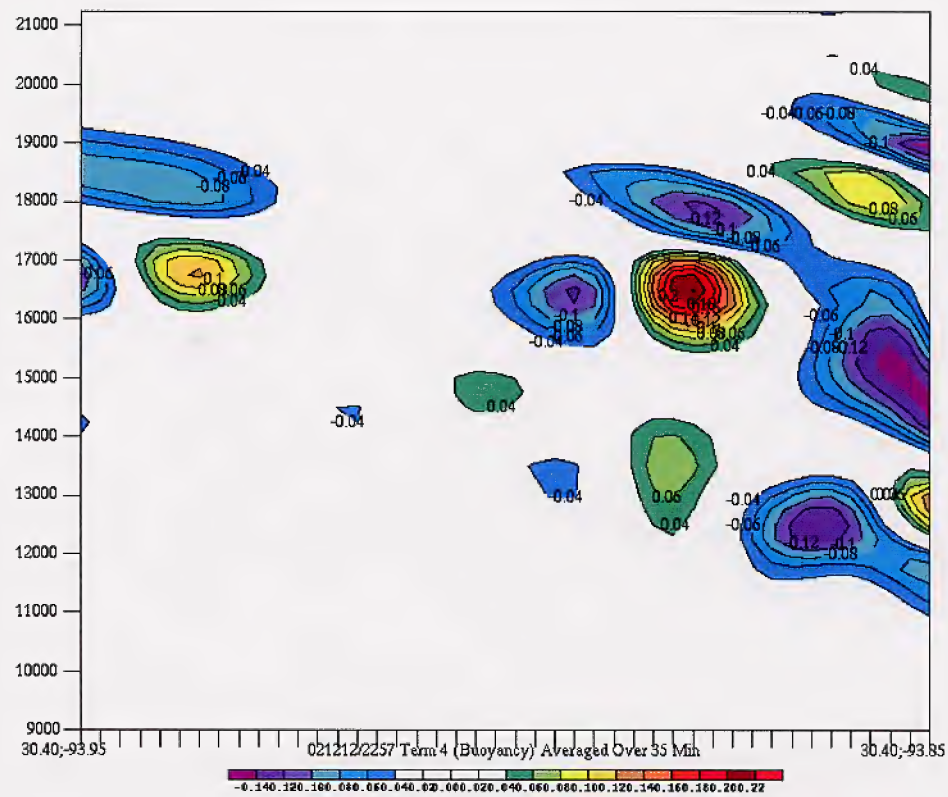


Figure B21.* TKE Budget for 12 December 2002, 222-m case in height coordinates: Term 3, W-Advection.

* Denotes figures inserted as part of Summer 2005 Research Update.



**Figure B22.* TKE Budget for 12 December 2002, 222-m case in height coordinates:
Term 4, Buoyancy Production.**

* Denotes figures inserted as part of Summer 2005 Research Update.

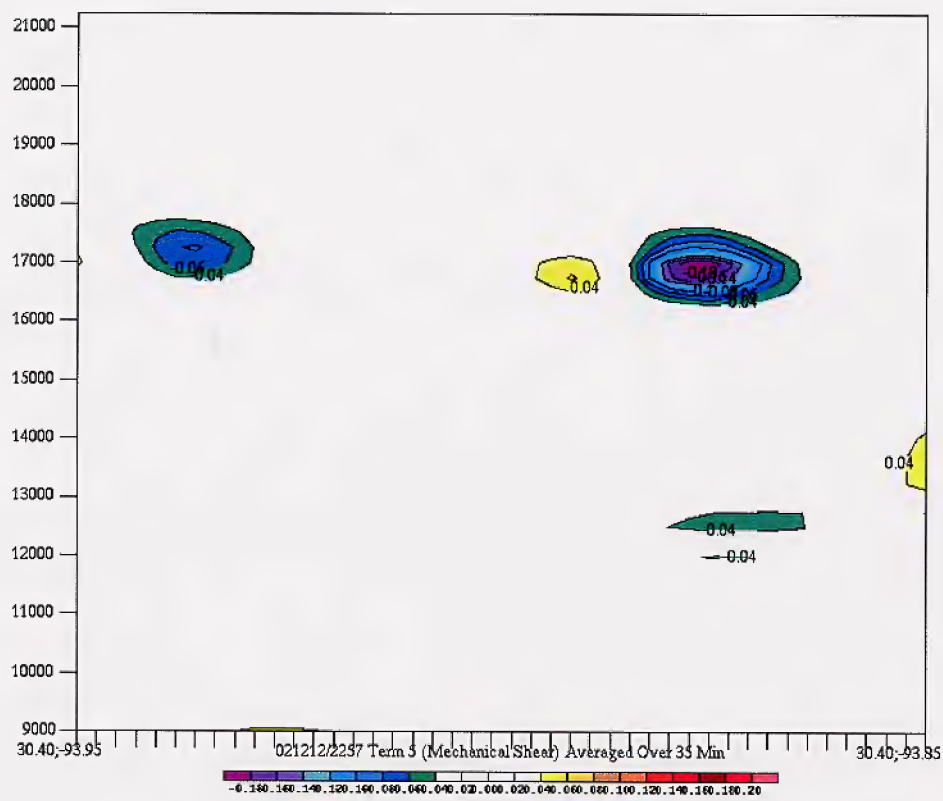
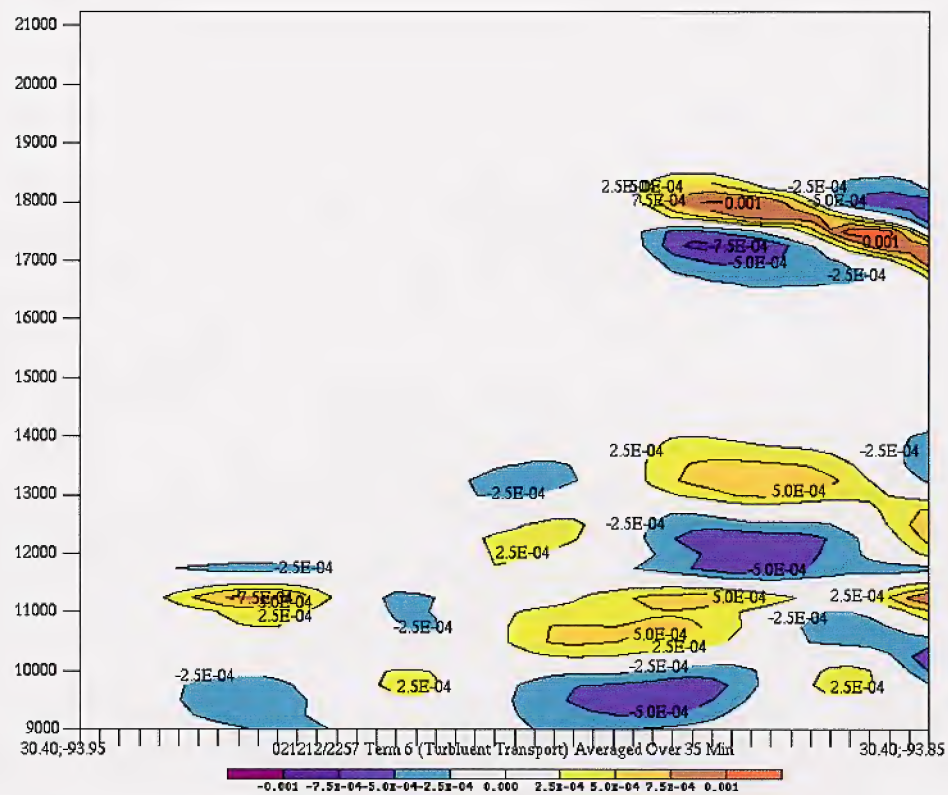


Figure B23.* TKE Budget for 12 December 2002, 222-m case in height coordinates: Term 5, Mechanical Shear.

* Denotes figures inserted as part of Summer 2005 Research Update.



**Figure B24.* TKE Budget for 12 December 2002, 222-m case in height coordinates:
Term 6, Turbulent Transport.**

* Denotes figures inserted as part of Summer 2005 Research Update.

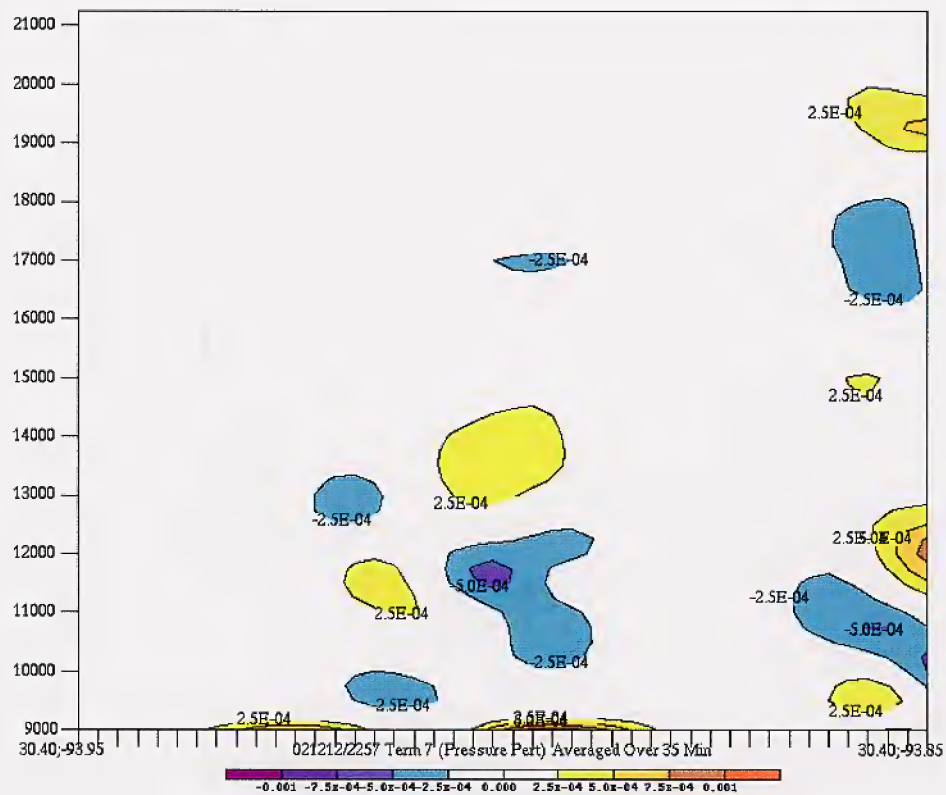
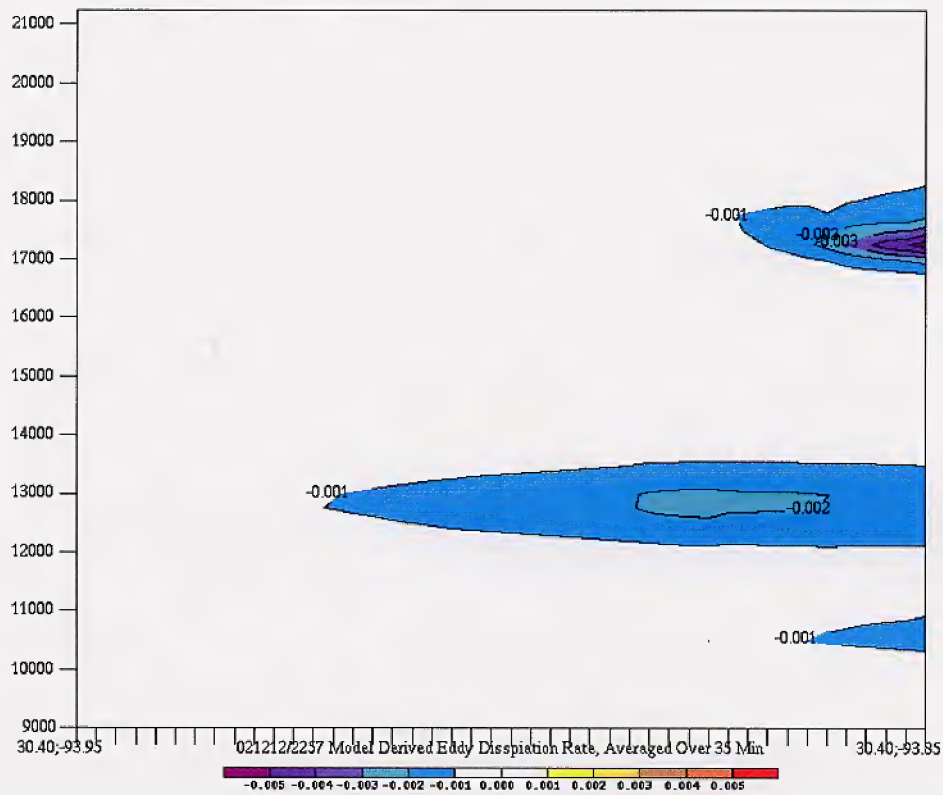


Figure B25.* TKE Budget for 12 December 2002, 222-m case in height coordinates: Term 7, Pressure Perturbations.

* Denotes figures inserted as part of Summer 2005 Research Update.



**Figure B26.* TKE Budget for 12 December 2002, 222-m case in height coordinates:
Term 8, Model Derived EDR.**

* Denotes figures inserted as part of Summer 2005 Research Update.



Figure B27.* TKE Budget for 12 December 2002, 71-m case in height coordinates: Term 1, U-Advection.

* Denotes figures inserted as part of Summer 2005 Research Update.

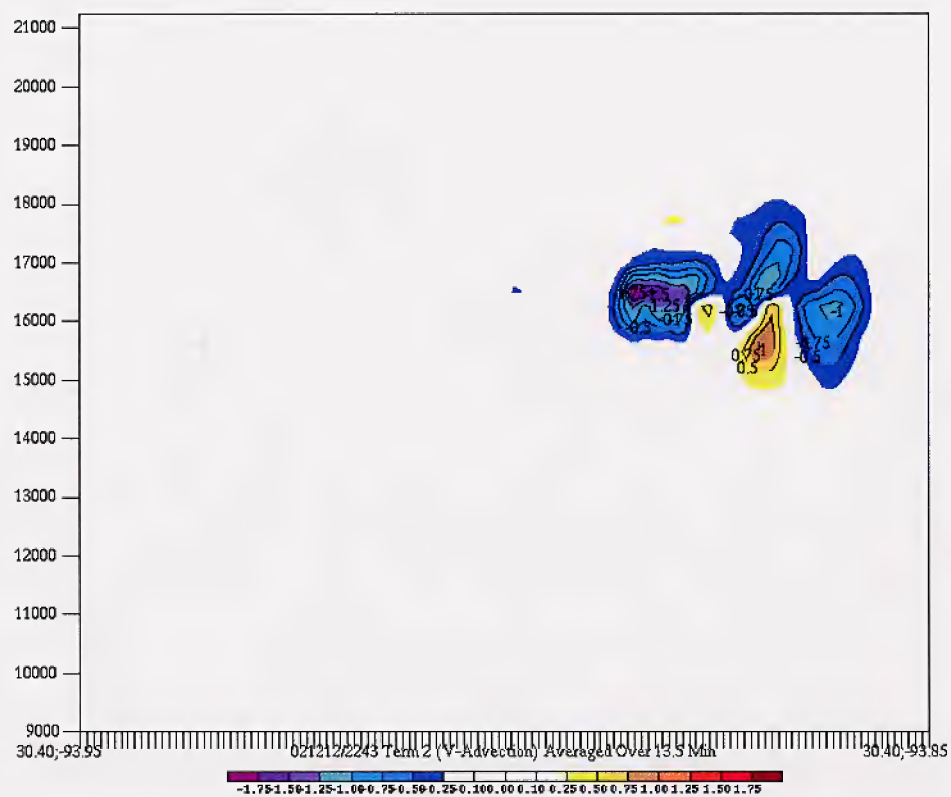


**Figure B28.* TKE Budget for 12 December 2002, 71-m case in height coordinates:
Term 2, V-Advection.**

* Denotes figures inserted as part of Summer 2005 Research Update.

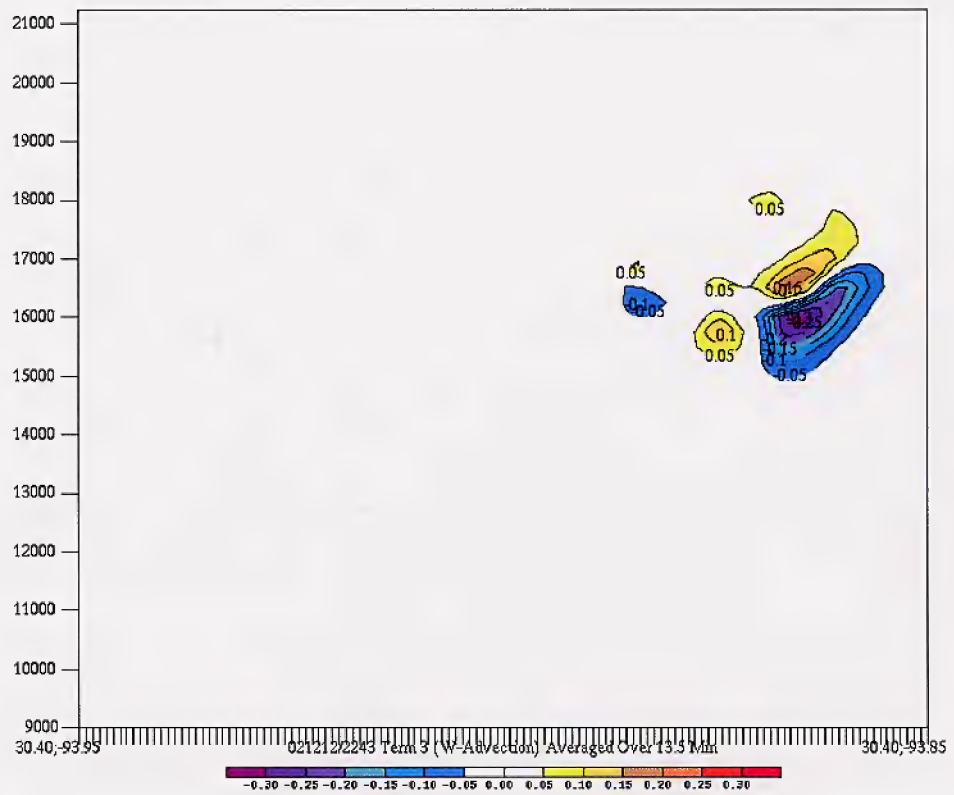


Figure B29.* TKE Budget for 12 December 2002, 71-m case in height coordinates: Term 3, W-Advection.

* Denotes figures inserted as part of Summer 2005 Research Update.

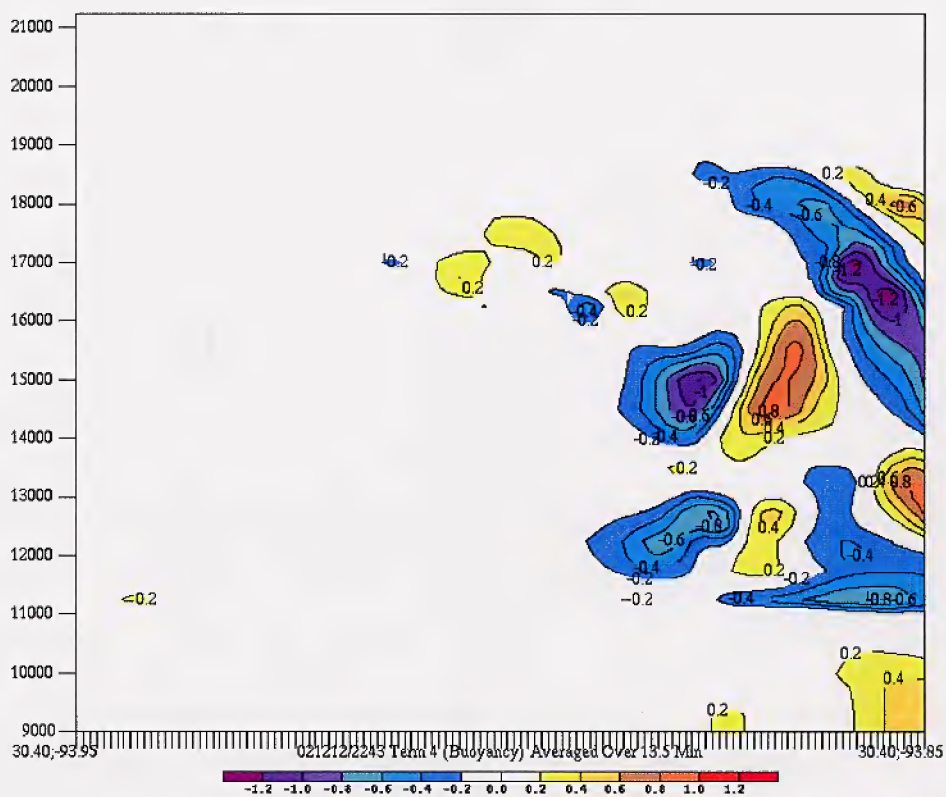


Figure B30.* TKE Budget for 12 December 2002, 71-m case in height coordinates: Term 4, Buoyant Production.

* Denotes figures inserted as part of Summer 2005 Research Update.

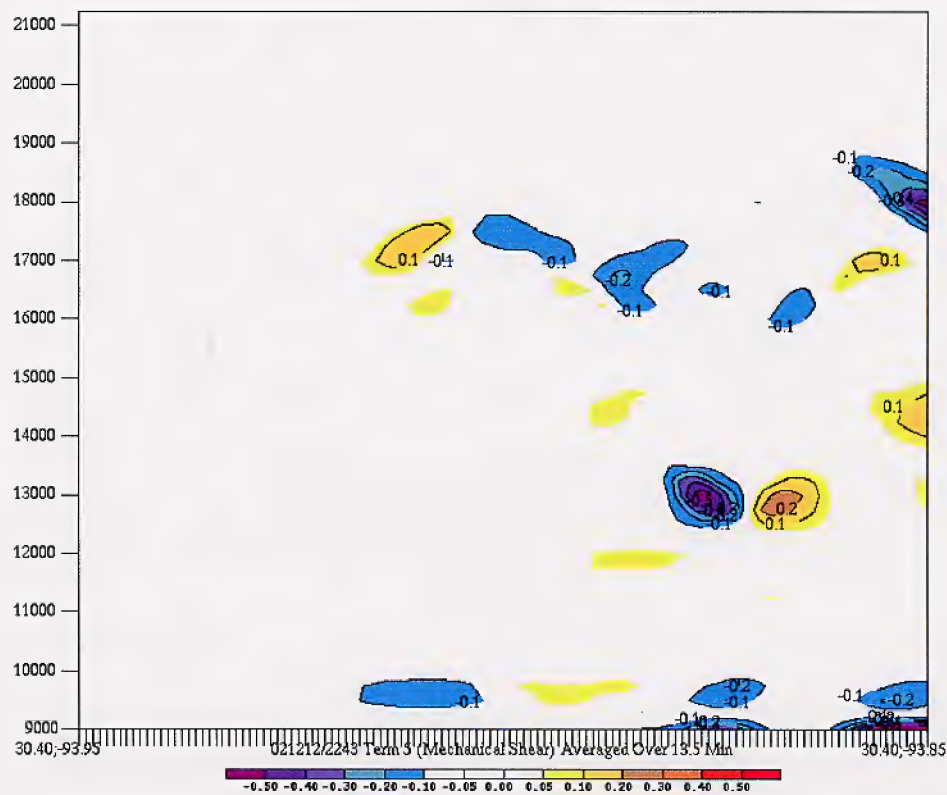


Figure B31.* TKE Budget for 12 December 2002, 71-m case in height coordinates: Term 5, Mechanical Shear.

* Denotes figures inserted as part of Summer 2005 Research Update.

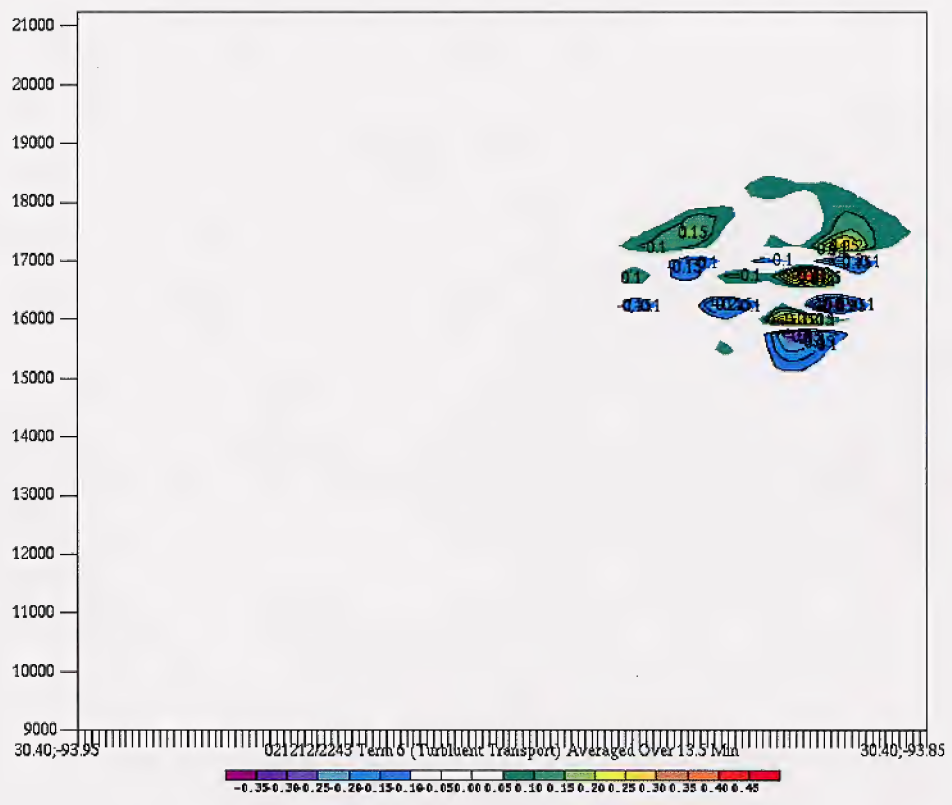


Figure B32.* TKE Budget for 12 December 2002, 71-m case in height coordinates: Term 6, Turbulent Transport.

* Denotes figures inserted as part of Summer 2005 Research Update.

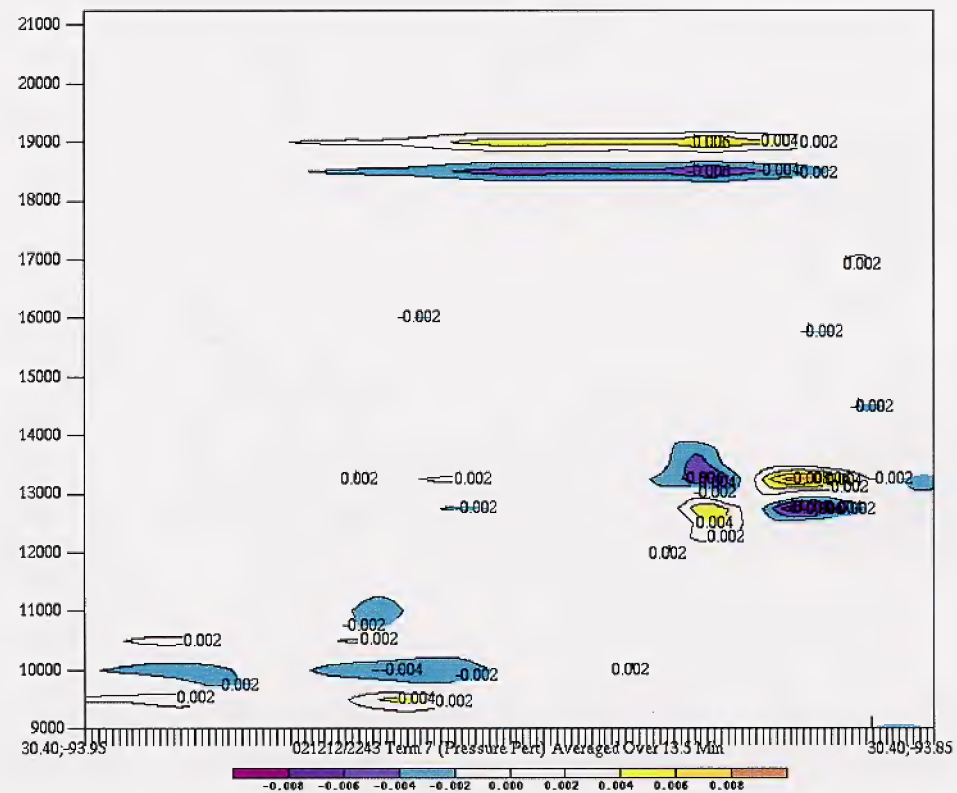
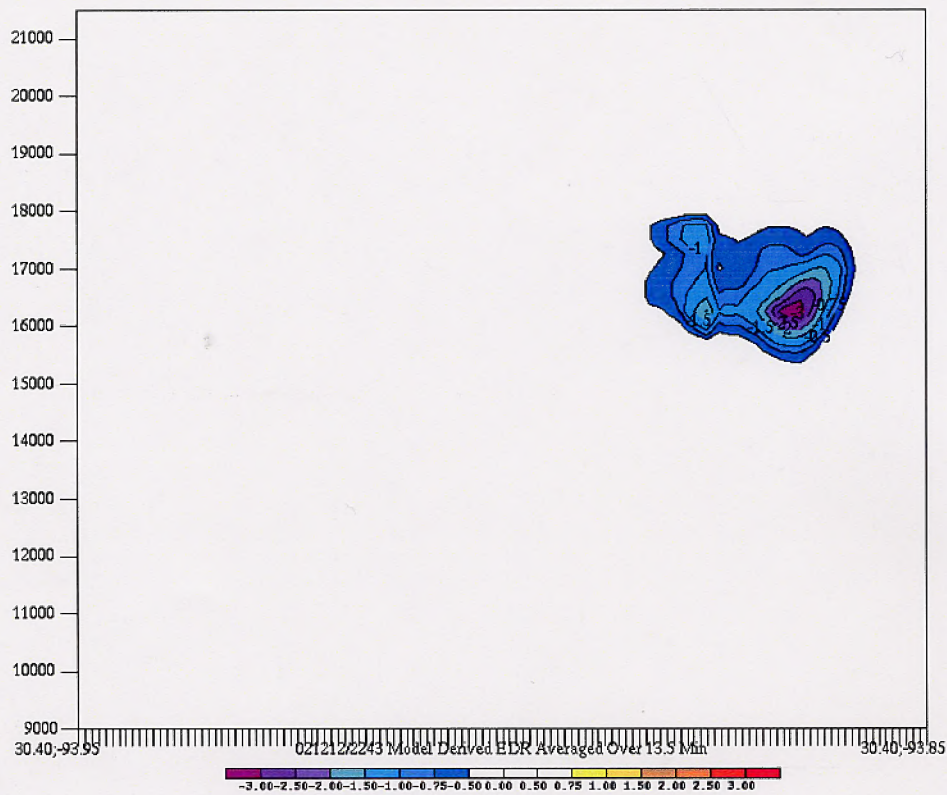


Figure B33.* TKE Budget for 12 December 2002, 71-m case in height coordinates: Term 7, Pressure Perturbations.

* Denotes figures inserted as part of Summer 2005 Research Update.



**Figure B34.* TKE Budget for 12 December 2002, 71-m case in height coordinates:
Term 8, Model-Derived EDR.**

* Denotes figures inserted as part of Summer 2005 Research Update.

REFERENCES

- Bluestein, Howard B., 1993: **Synoptic-Dynamic Meteorology in Midlatitudes, Volume II.** Oxford University Press: Chap. 3.4, pp. 431-520.
- Lin, Y-L. *Mesoscale Meteorology*. To be published. Ch.4: Finite Difference Schemes, Spring 2005.
- Stull, Roland B., 1988. **An Introduction to Boundary Layer Meteorology.** Kluwer Academic Press: 639 pages.

